Non-perturbative calculations of atomic data for applications in laboratory fusion and astrophysical plasmas

by

Di Wu

A dissertation submitted to the Graduate Faculty of
Auburn University
in partial fulfillment of the
requirements for the Degree of
Doctor of Philosophy

Auburn, Alabama
May 4, 2013

Keywords: electron-impact ionization, electron-impact excitation, fusion plasmas, supernova remnant plasmas

Approved by

Stuart Loch, chair, Associate Professor of Physics
Michael Pindzola, Professor of Physics
Connor Ballance, Research Professor of Physics
Michael Fogle Jr., Assistant Professor of Physics

Abstract

Results are presented for non-perturbative quantal calculations of atomic data for application in laboratory fusion and astrophysical plasmas. One of the key issues in laboratory fusion plasmas is the accurate modeling of impurity transport of wall material as it is ablated into the plasma. In support of experiments at Wisconsin-Madison, new ionization cross sections for Al and Al^{2+} were generated. These are supplemented with previous non-perturbative calculations for Al^{+} and new distorted-wave calculations for the remaining ions. This new ionization dataset is compared with previous semi-empirical calculations and literature values, and the likely implications for impurity transport modeling are discussed.

For the application to astrophysical plasmas, a recent development in supernova remnant X-ray emission is considered. The emission from less abundant iron-peak elements (Mn, Cr, Co and Ni) from supernova remnant plasmas has been detected and represents a potentially useful diagnostic opportunity to determining elemental abundances in these plasmas, and to test current supernova models. However, the studies are currently hampered by a lack of K-shell atomic data for many of the Fe-peak elements. Thus, R-matrix calculations for the electron-impact excitation of Ne-like Cr, Mn, Fe, Co and Ni ions are calculated. Collisional-radiative modeling is used to produce emissivities for each of these ions. The results are compared with X-ray spectra from the Tycho supernova remnant plasma, and abundances for Cr and Mn are derived. Evidence is presented that the line commonly identified as Fe Kβ is blended with another line, possibly the Co Kα feature. To assess the possibility that this line originates from a neighboring charge state of Fe, new atomic data for F-like Fe-peak elements are produced. The future direction of this work, and the potential applications of the data are also discussed.

Acknowledgments

I would like to thank those people who have helped me during my doctoral studies. Working towards obtaining a Ph.D. has been the most challenging experience of my life. I have made it this far thanks to the help provided by so many.

I especially want to thank my Ph.D. supervisor, Prof. Stuart Loch, for his guidance throughout my studies at the Auburn University Physics Department. He patiently provided vision, encouragement and advice that helped me excel in my studies, research and thesis writing. I enjoyed his Scottish stories, jokes and accent. I also appreciate the help provided by Prof. Connor Ballance. He guided me through the large calculations from the beginning and inspired me to take a greater interest in coding. I want to thank Prof. Michael Pindzola as well. Because of his atomic physics course, I decided to focus my research on atomic physics. I would also like to thank my other committee members, Prof. Michael Fogle and Prof. Orlando Acevedo. I really appreciate their support, guidance and suggestions. Many thanks to the entire atomic physics group and the physics department. Working with you has been the happiest part of my developing career. And thanks to Naty, who is the best office mate.

As a female, majoring in Physics is challenging. However, it opened my eyes to the wonderful physics world that most girls don't get to see. Mr. Jialong Liang, who was my physics teacher in middle school, opened this world for me and showed me how beautiful physics is. That's where I first began to fall in love with physics. Mr. Yan Sun, who was my math mentor in middle school, encouraged me to join the Mathematics Olympiad Competition and gave me lots of advice. From then on, I became positive, confident and optimistic. I really appreciate their help in changing my life at that point.

I also want to thank my family. Five years ago, a wonderful and caring woman tried to convince me to come to the US and get a higher education. That was my mother and best friend. I really appreciate that she raised me by herself. She always gave me good advice and led me in the right direction. I am eternally grateful to her. I also want to thank my in laws. They gave me a lot of love and support. Because of their help during my qualifying exams, I was well prepared and was able to pass them. My sister in law also gave me suggestions about writing and she's the best movie date! I also appreciate the understanding, help and love from my husband, Trey. He sacrificed two years in order to help me finish my PhD. He also helped me a lot by taking care of our daughter and the housework. I can taste the love from the meals he cooks for me everyday. I love you all. Sorry and thank you to my daughter, Jeni. I am sorry if I didn't spend enough time with you. But every time I worked late, felt tired, got frustrated, just thinking about your peaceful, lovely face, helped me regain the energy and enthusiasm to continue working. Just seeing your smile, helps me see that all this hard work is worth the effort and sacrifice. I am eternally grateful to have you as my daughter.

Finally, I want to thank the National Aeronautics and Space Administration (NASA) for their financial support of my research.

Table of Contents

List of Figures

List of Tables

Chapter 1

Introduction and background theory

1.1 Introduction

This dissertation focuses on the generation of new atomic physics cross sections for application in two main areas. The first area of application is for impurity transport of aluminum in laboratory plasmas and the second is the emission of Fe-peak elements from supernova remnant plasmas. The common theme to both of these applications is that understanding the emission characteristics of less abundant atomic species provides a wide range of useful diagnostics for each of these plasma environments. However, before such diagnostics can be used with confidence, the accuracy of the atomic data must be assessed. In the case of the laboratory plasmas this led to the generation of new non-perturbative calculations for the electron-impact ionization of neutral Al and Al^{2+}. In the case of the supernova remnant plasma this led to the generation of new non-perturbative electron-impact excitation atomic data for Ne-like and F-like Cr, Mn, Fe, Co and Ni.

Before describing these calculations, and the associated modeling work, a brief overview of the two different plasma environments is given. A description of the theoretical methods used to calculate the atomic data and perform the spectral modeling is then given in this chapter. In chapter 2 of the dissertation, the new atomic data for neutral Al is presented. Chapter 3 describes the new R-matrix calculation for Al^{2+}, along with the distorted-wave calculations that have been performed to complete the Al ionization database. Chapter 4 shows some ionization balance results using the new data and discusses the implications for impurity transport modeling. Chapter 5 and 6 describe the new atomic data for supernova remnant plasma diagnostics. Chapter 5 contains the Ne-like Mn, Cr, Fe, Co and Ni electron-impact excitation results along with an analysis of X-ray spectra from the Tycho supernova

remnant plasma. Chapter 6 contains the results for F-like Cr, Mn, Fe, Co and Ni. The conclusions are presented in Chapter 7.

1.1.1 The role of impurity species in laboratory magnetically confined plasma experiments

Magnetically confined plasmas for fusion energy applications have been the subject of active research for more than 50 years, with much progress having been made. The aim is to magnetically confine a plasma of deuterium and tritium at densities such that the confinement time is sufficient for a sustained fusion reaction to occur. A wide range of experiments have been studied, with tokamaks and spheromaks being the two strongest candidates for a magnetically confined approach. The tokamak experiments have increased in size dramatically, with the next experiment being the ITER device currently under construction in Cadarache, France, see fig 1.1.

One of the critical issues for ITER, and all tokamaks, is that the radiative power loss from impurities in the core plasma not reduce the energy confinement to such an extent that the fusion reaction is quenched. These impurities largely originate from the vessel walls. Thus, understanding their influx rates from the walls, and their transport rates into the core plasma, is key to ensuring a sustained fusion reaction. Modeling the transport of such impurities represents a challenging problem, with approaches including the 1D transport code SANCO [18], suites of codes such as SOLPS [19] and TRANSP [20] and the gyrokinetic code XGC [21]. Each of these codes requires atomic physics data through the use of effective ionization and recombination rate coefficients (and metastable cross-coupling coefficients if required). Impurity species that are ablated from the vessel walls cross a wide range of plasma conditions, from T_e=1-10eV and N_e $\sim$1$\times$ 10^{14} cm^{-3} in the edge diverter region, across a very sharp temperature gradient in the scrape off layer at the last closed flux surface, through to temperatures of 10-20 keV in the core region. Thus, for most impurities one would expect them to pass through a wide range of ion stages as they are transported through the plasma.

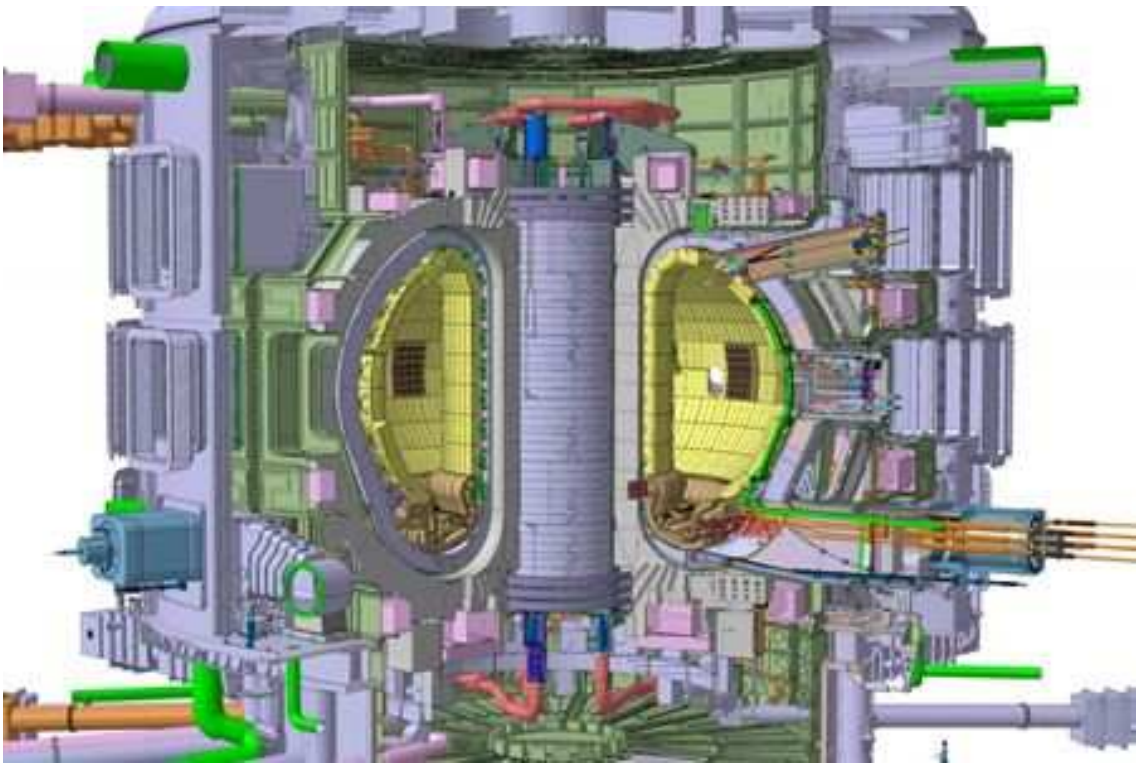

Figure 1.1: Schematic of the ITER tokamak being built in Cadarache, France. Taken from the ITER Organization, http://www.iter.org/

Studies using existing atomic data, along with theoretical values for the radiative power loss have shown that tungsten impurities of 1.9×10^{-4} under ITER conditions would effectively quench the fusion reaction, compared to a plasma without any impurities [22, 23]

In this dissertation new atomic data is generated for all of the ion stages of aluminum, in support of impurity transport studies at the Madison Symmetric Torus, at the University of Wisconsin-Madison (see Fig 1.2). This vessel has Al walls, and recent studies have shown that existing data for Al ionization and recombination is not able to reproduce the spectral signatures observed on the experiment. Figure 1.3 shows an equilibrium ionization balance calculation for aluminum as a function of electron temperature. The current atomic data for Al recombination consists of distorted-wave calculations for all of the ion stages (see the papers of the Dielectronic Recombination (DR) project [24, 25] and the results from the the Flexible Atomic Code [26]). Due to the dominance of DR over radiative and three-body recombination for tokamak conditions, this means that the recombination data is likely to be of sufficient quality for the modeling. The ionization data on the other hand is in significant need of improvement. It currently consists of semi-empirical data generated using the exchange classical impact parameter method [27] or Lotz ionization cross sections. The review of Dere [12] and of Mattioli et al. [28] used a combination of experimental measurements and distorted-wave calculations for the ionization cross section. Thus, in this dissertation new non-perturbative calculations are presented for the electron-impact ionization of Al [29] and Al^{2+}[30]. This is combined with previous non-perturbative calculations for Al^{+}, and new distorted-wave calculations for the remaining ions. This new data is then compared with the data currently available in the ADAS database and in the literature.

Figure 1.2: Photograph of the Madison Symmetric Torus, for which the aluminum data in this dissertation is calculated.

1.1.2 Supernovae and supernova remnant plasmas

A supernova is a thermonuclear stellar explosion that provides some of the brightest X-ray sources in the universe. The burst of radiation often briefly outshines the galaxy that contains the supernova, before fading from view over several weeks or months. During this short interval a supernova can radiate as much energy as the Sun is expected to emit over its entire life span. Emission from the supernova remnant plasma persists for extremely long time.

The first recorded observation of a supernova was in 185 AD in China. Visual observations in modern times originally consisted of supernovae from within the Milky Way. Telescopes allowed observations of supernova from other galaxies, such as observations of S Andromedae in 1885. Supernova were originally classified by their spectral signatures. Events showing no H spectra lines were called Type I, while those with H lines were classified as Type II. Subcategories were later defined, with events with no H or He lines called Type Ia and events with neutral He lines called Type Ib. Type II and Type Ib supernovae are now believed to be due to core-collapse events, while Type Ia supernovae are due to binary star systems. In a Type Ia supernova the progenitor star is thought to be a white dwarf or neutron star, which accretes material from the companion star until it crosses the Chandrasekhar limit [31].

Type Ia supernovae are characterized by their spectra, showing a lack of any hydrogen or helium lines in any phase of their evolution and a strong absorption line due to Si II near 6100 Å. Type Ia spectra usually show forbidden Fe and Co lines in their late-phase. With the range of X-ray telescopes now available (XMM-NEWTON, SWIFT, CHANDRA, SUSAKU), there have been various observations of supernovae remnants, looking at X-ray emission after the reverse-shock has heated the plasma.

The model for Type Ia supernovae as a thermonuclear explosion is described in detail in various papers, see Woosley and Weaver[31]. Type Ia supernovae have found a wide use in a number of astrophysical applications. They are believed to arise from thermonuclear

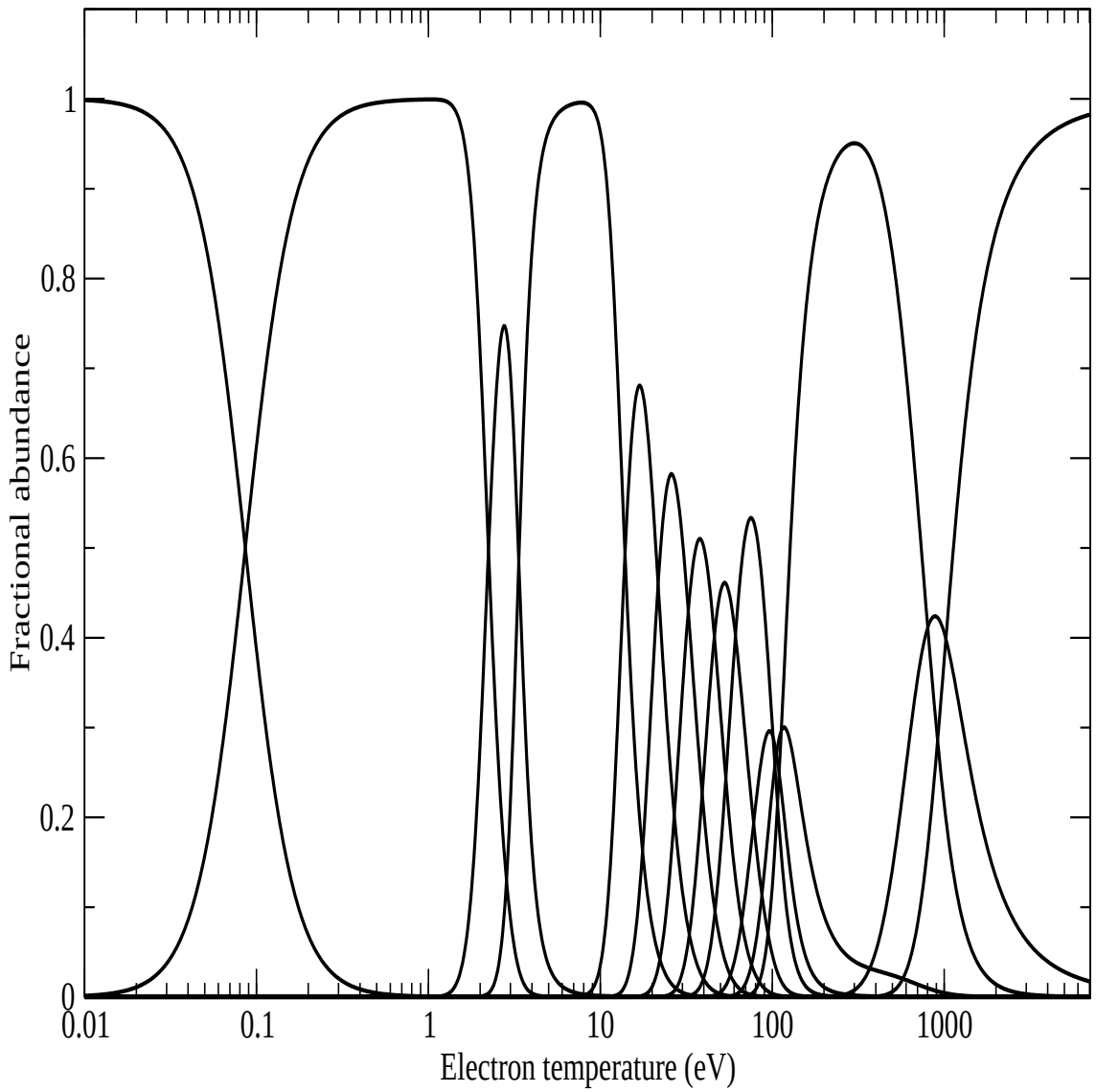

Figure 1.3: Equilibrium ionization balance for Al as a function of electron temperature for N_e=1$\times$ 10^{14} cm^{-3}

explosions of low-mass stars (called the progenitor star) such as a white dwarf which accretes material from a companion star until the progenitor's mass crosses the Chandrasekhar limit [31]. It was originally expected that all Type Ia supernova should have the same characteristic light curve, leading to their use as standard candles. In recent years there have been a range of co-ordinated supernovae searches, such as the Asiago Supernova Catalogue [32], leading to about 200 supernova detections each year. These have lead to a much more complex picture of Type Ia supernovae with the possibility of sub-Chandrasekhar explosions a real possibility [33, 34]. Due to their characteristic light curve, they have been used as standard candles [35], providing a useful distance measurement to red-shifted galaxies [36]. As such, Type Ia supernova spectra have been used to determine the Hubble constant [37] and in more recent years to measure the acceleration of the universe [38]. Modeling Type Ia supernova nucleosynthesis is the key in understanding the elemental abundances in the universe, with Type Ia supernovae expected to be the dominant source for production of elements near Fe. Type Ia supernovae are also believed to play a significant role in the heating of the interstellar medium [39] and may be responsible for a significant fraction of the loss of material from galaxies [40]. This highlights one of the main uncertainties in supernova research, namely that we have a poor understanding of the progenitor stars. Some of the uncertainties in our knowledge of the progenitor stars include: at what mass does the progenitor explode (i.e. Chandrasekhar or sub-Chandrasekhar), how much carbon simmering of the white dwarf occurs before it explodes, and what is the metallicity of the progenitor? One of the aims of this dissertation is to provide currently lacking atomic data that can be used to further such studies, in particular atomic data for Fe-peak elements(Cr, Mn, Fe, Co and Ni).

A range of spectral diagnostics are possible if accurate atomic data for Fe-peak elements is added to existing databases. For example, one can determine the metallicity of supernova progenitors using the Mn-to-Co spectral line ratio, as demonstrated by Badenes et al [41]. Badenes et al. [41] showed that this same ratio is also sensitive to the degree of carbon simmering of the progenitor [41]. Yang et al. [42] showed that the ratio of the equivalent

line widths of Co-to-Fe can contain information about the progenitor and the explosion mechanism. This ratio was used to determine the mass ratio of these Fe and Co ions. This in turn was used as an indicator of whether a supernova was Type Ia or Type II. They also showed that this method has the potential to indicate a detonation model for Type Ia events. Also, line ratios from the He-like or Ne-like ion stages are a useful electron temperature diagnostics [43]. Measurements of the ion stage abundances of non-equilibrium ionization supernova remnant spectra provides a diagnostic of the ionization age of the supernova. Using multiple Fe-peak elements in these diagnostics would provide tight constraints on the diagnosed quantities. The emission that we are interested in consists of X-ray K-shell spectra with potential emission from both Kα and Kβ transitions. For example, Fig.1.4 shows a recent Suzaku observation of the Tycho supernova remnant, which notes that the Fe Kα and Kβ features, along with weaker features from Cr and Mn.

The first X-ray observations of Co and Mn spectral emission from supernova remnant plasma were of the He-like Co and Mn lines from supernova W49B using the ASCA X-ray telescope [44]. This was later confirmed by XMM-Newton observations [45]. No atomic data for the He-like stages of Co or Mn existed, so Hwang et al. [44] obtained data by interpolating from Ca, Fe and Ni atomic data. Yang et al. [42] undertook a survey of Co-K emission of young supernova remnants, finding evidence of Co emission in supernovas W49B, Cas A, Tycho and Kepler. Recently there have been a range of X-ray observations of supernovae, including observations by SWIFT [34], ASCA [44], CHANDRA [46], SUSAKU [1] and XMM-NEWTON [45]. Tamagawa et al. [1] tentatively identified spectral lines from Tycho as belonging to Ne-like Mn and Cr, but had to rely on extrapolated energies to make this identification. Fig.1.4 is taken from Tamagawa et al. [1] and shows their identification of Cr and Mn spectral lines in Tycho. Despite the identifications of Fe-peak element lines, it is clear that diagnostic studies using these lines is currently hampered by a severe lack of accurate atomic data for these ions. For example, Tamagawa et al. [1] stated that

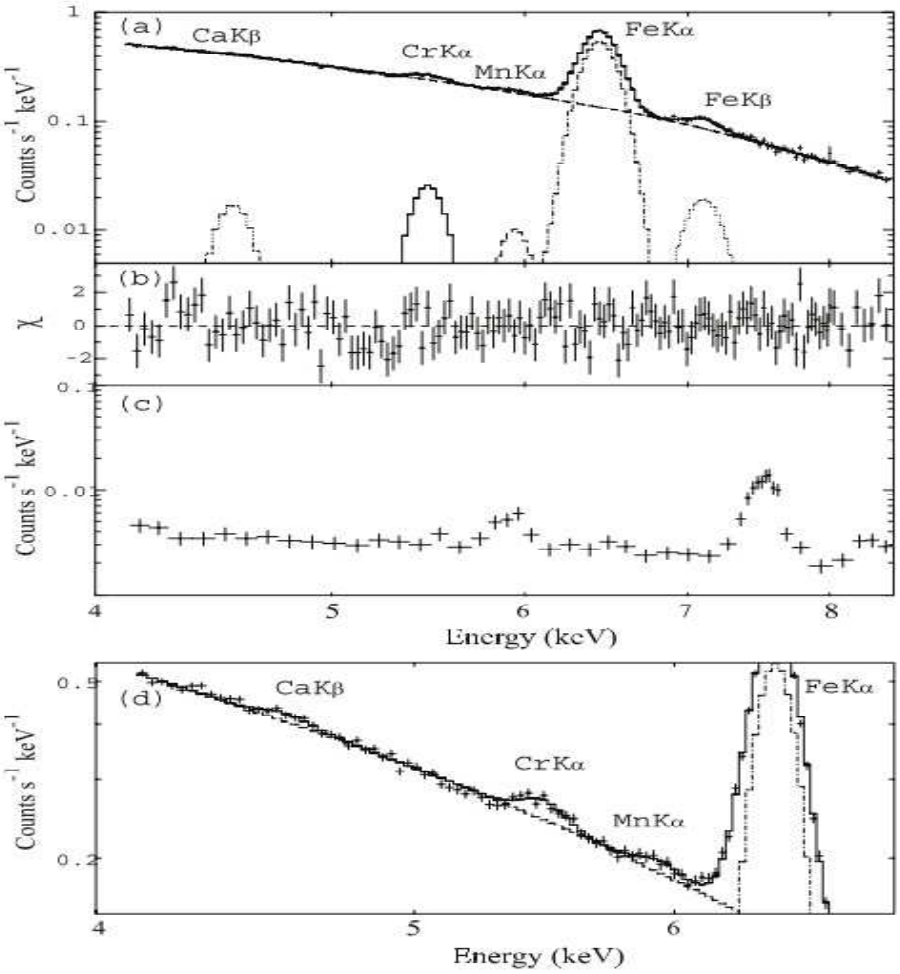

Figure 1.4: Suzaku observation of the Tycho supernova remnant, taken from [1].

"Cr and Mn K_α lines were detected previously only from W49B.....Detailed emissivity calculations for trace species in nonequilibrium hot plasmas are strongly encouraged to open this new method for supernova nucleosynthesis diagnostics".

Badenes et al. [47] showed that the X-ray spectrum can be used to test different supernova explosion models, including whether the explosion was sub-Chandrasekhar. Studies on the Cr emission lines and have found them, in general, to be in similar ion stages to the Fe lines from the same objects [42]. Most of the Fe-peak element lines that have been seen are Kα transition. We note that Tamagawa et al. [1] identified Kβ transitions from Fe and Ca in their work of Tycho, indicating that faint Kβ transitions from Fe-peak elements may be observable.

In this dissertation, we calculate new K-shell electron-impact excitation data for Ne-like and F-like Cr, Mn, Fe, Co and Ni. We also calculate synthetic spectra of the Ne-like ions and compare with observations from Tycho supernova remnant [48], deriving relative abundance for Cr, Mn and Fe.

1.2 Theory

1.2.1 Collisional-radiative theory

Many processes play a role in populating the excited states of atoms and ions, and balancing all of these rates is the key to modeling the emission from both laboratory and fusion plasmas. As will be seen, a number of simplifying assumptions can be made based on the time-scales commonly encountered in the plasmas under consideration.

The atomic processes that can be important for most laboratory and astrophysical plasmas include (but are not limited to) spontaneous decay ($A_{i\to j}$), Auger processes ($A^a_{i\to\sigma}$), Electronic collisional excitation/de-excitation ($q^e_{i\to j}/q^e_{j\to i}$), electron-impact ionization ($S_{i\to\sigma}$), and recombination. Recombination processes include radiative (α^r_i), dielectronic (α^d_i), and three body recombination (α^3_i). Charge exchange can also be important process, such as in the neutral beam experiments on tokamaks [49], or in modeling the X-ray emission from

comets or planetary atmospheres [50]. Note that other processes such as proton collisions can be included in the collisional-radiative formalism. For this work we will ignore proton collisions and charge-exchange as the other collisional processes dominate.

Considering first the time-scale for the different plasma species to reach their equilibrium values, one finds that a number of approximations can be made. The fastest collisional process in plasma is usually the Auger decay processes, thus collisional-redistribution amongst the autoionization levels can often be ignored, though can be included in the collisional-radiative framework as described in Summers et al. [27]. The electron-electron equipartition times are also extremely fast, resulting in Maxwellian distributions for the free electrons in the plasma. While there is some indication that non-Maxwellian distributions may exist in tokamak plasmas they are not considered in this work. However, non-Maxwellian rate coefficients can be easily generated from the cross sections shown later in this dissertation, therefore these effects could be included in future work.

Considering next the time-scale of the energy levels within a given ion stage, the levels can be separated into excited states and the ground/metastable levels. The excited states can decay through dipole radiative decay and so have very fast radiative lifetimes, typically 10^{-8} s for near neutral systems. The ground and metastable levels on the other hand cannot radiatively decay easily and are controlled by collisional processes. They can have equilibrium time-scales comparable with the plasma dynamical time-scales, often of tenths of a second through to seconds for laboratory plasmas. The very low density supernova remnant plasmas can have ionization equilibrium time-scales of hundreds or thousands of years. Thus, one can usually model the excited states as being in instantaneous equilibrium with the ground and metastable levels which in turn must be tracked time-dependently.

Consider an ion consisting of a set of levels with radiative and collisional couplings. The time dependence of the population N_i of an arbitrary level i, in ion stage $+z$ is given by the following set of coupled differential equations

$$\begin{aligned}\frac{dN_i}{dt} &= \sum_\sigma n_e N_\sigma^{z+1}(\alpha_i^r + \alpha_i^d + n_e\alpha_i^3) + \sum_{j<i} N_j n_e q_{j\to i}^e + \sum_{j>i} N_j(n_e q_{j\to i}^e + A_{j\to i}) \\ &= -N_i\Big\{\sum_{j>i} n_e q_{i\to j}^e + \sum_{j<i}(n_e q_{i\to j}^e + A_{i\to j}) + \sum_\sigma (n_e S_{i\to\sigma} + A_{i\to\sigma}^a)\Big\} \end{aligned} \tag{1.1}$$

where n_e is the free electron density. It can be shown [27] that this can be reduced to a more compact form

$$\frac{dN_i}{dt} = \sum_\sigma n_e N_\sigma^{z+1} r_{i\sigma} + \sum_j C_{ij} N_j \tag{1.2}$$

with a populating term for $i \neq j$,

$$C_{ij} = A_{j\to i} + n_e q_{j\to i}^e + n_e q_{j\to i}^p \tag{1.3}$$

a loss term for $i = j$,

$$C_{ii} = -\Big(\sum_{i>j} A_{i\to j} + n_e \sum_{j\neq i} q_{i\to j}^e + \sum_\gamma n_e S_{i\gamma}\Big) \tag{1.4}$$

and a composite recombination coefficient $r_{i\sigma} = \alpha_i^r + \alpha_i^d + N_e\alpha_i^3$. The equation can thus be written as

$$\sum_j C_{ij} N_j = \frac{dN_i}{dt} - \sum_\sigma n_e N_\sigma^{z+1} r_{i\sigma} \tag{1.5}$$

where we define C as the collisional-radiative matrix. Taking into account an m number of metastables (including the ground state), we can set $\frac{dN_\rho}{dt} \neq 0$ for $1 \leq \rho \leq m$, and $\frac{dN_i}{dt} = 0$

for $i > m$, where ρ defines the set of ground and metastable levels and i represents the excited levels. This allows the population of an 'ordinary' level to be determined as a function of the ground and metastable populations of the Z ion stage (N_ρ^Z), and of the $Z+1$ ion stage (N_σ^{Z+1}).

Thus, the population of the j^{th} 'ordinary' level can be solved for the contribution due to each of the 'driving' populations.

$$N_j^z = -\sum_\rho \sum_i C^{-1}_{ji_{(r)}} C_{i\rho} N_\rho^z - \sum_\sigma \sum_i C^{-1}_{ji_{(r)}} r_{i\gamma} N_\sigma^{z+1} n_e \tag{1.6}$$

This has been shown in a number of places, first in the paper by Bates, Kingston and McWhirter [51]. This was later extended to include the role of metastables [27]. Notice, the inverse matrix in equation (1.6) $C^{-1}_{ji_{(r)}}$ is not the inverse of the collisional-radiative, but rather the inverse of the reduced collisional-radiative matrix that has had the ground and mestables rows/columns removed.

As equation (1.6) shows, the solution for the equilibrium population for any 'ordinary' level depends upon the population of the ground and metastable levels. In order to get the ground and metastable population we calculate the ionization balance for the specified ion stage. In the simplest case this can be generated from an equilibrium solution to the ionization balance equations (see the next section) where all of the time derivatives are set to zero. One can also perform a non-equilibrium ionization balance calculation, where the fractional abundances are tracked as a function of time. The most rigorous solution for most plasma applications is found from using the atomic data in a plasma transport code, where plasma dynamics can be modeled simultaneously with the ionization balance of the ions in the plasma. The data will also be provided to collaborators who will use the data in their transport codes.

1.2.2 Ionization balance

In order to solve our collisional-radiative model we need to know the ground and metastable populations of the ions of an element in equilibrium in a thermal plasma. Consider an element **X** of nuclear charge z_o, the populations of the ionization stages are denoted by

$$N_z : z = 0, \ldots, z_o \tag{1.7}$$

When considering the z ion stage we include only the adjacent ion stages, that is we do not include two ion stage jumps in a single atomic process, since sequential single ionization and recombination is the dominant process. The time dependence of the ionization stage populations is given by

$$\frac{dN_z}{dt} = n_e S_{z-1\to z} N_{z-1} - \Big(n_e S_{z\to z+1} + n_e \alpha_{z\to z-1}\Big) N_z + n_e \alpha_{z+1\to z} N_{z+1} \tag{1.8}$$

This is also subject to the normalization condition

$$N_{Tot} = \sum_{z=0}^{z_o} N_z \tag{1.9}$$

where N_{Tot} is the number density of ions of element **X** in any ionization stage. In an equilibrium ionization balance calculation, the time derivatives are set to zero in equation (1.8). Since one often does not know the exact value for N_{Tot}, one solves for the equilibrium fractional abundances N_z/N_{Tot} at a set of temperatures and densities.

Notice that the above equations can be easily extended to include contributions from charge exchange and proton collisions. These will be negligible processes in our plasmas and will not be considered. Furthermore the above equation is for the 'stage-to-stage' ionization balance and do not resolve metastables within an ion stage. The equation can be generalized to include metastables with the introduction of metastable resolved ionization and recombination, rate coefficients, and metastable cross-coupling coefficients, see Summers et al. [27] for more details.

1.3 Theoretical methods for electron-impact ionization and excitation

In the following section, examples of the atomic processes will be given using aluminum, though the methods described are general and can be applied to any system. Consider first non-perturbative methods for the calculation of electron-impact ionization processes. The main contributions to the electron-impact single ionization cross section are from direct ionization, e.g.

$$e^- + Al^{2+} \rightarrow Al^{3+} + e^- + e^-, \tag{1.10}$$

and excitation-autoionization

$$e^- + Al^{2+} \rightarrow (Al^{2+})^* + e^- \rightarrow Al^{3+} + e^- + e^-. \tag{1.11}$$

$(Al^{2+})^*$ represents an excited state of the ion, and for the process of excitation-autoionization, there is also the possibility of radiative stabilization occurring before the excited ion can autoionize. Thus, autoionizing configurations are associated with an Auger yield, giving the fraction of electrons that will autoionize from such a configuration. For many of the ion stages considered here the Auger rates are much larger than the radiative rates, and it is a reasonable approximation to assume that the Auger yield is 100%.

It is also possible for the excitation in the first step of Eqn. 1.11 to proceed via a dielectronic capture (e.g. into $(Al^{+})^*$), which subsequently autoionizes to the excited state

$(Al^{2+})^*$ in Eqn. 1.11. This state can then autoionize as indicated in the rest of Eqn. 1.11. These resonant features on the excitation cross sections are known as resonant-excitation double autoionization (REDA) features. Alternatively the state formed from the dielectronic capture can undergo an auto-double ionization, known as resonant-excitation auto-double ionization (READI).

Thus, the total cross section, considering both direct and indirect processes is

$$\sigma_{total} = \sum_i \sigma_{direct} + \sum_j \sigma_{indirect} \tag{1.12}$$

where the sum i is over the direct ionization channels, and the sum j is over the inner subshell electrons which can be excited (both directly and via a resonance state), leading to an autoionizing configuration.

1.3.1 Configuration-average Distorted-Wave Method

The direct ionization process can be evaluated using the configuration-average distorted-wave method[48], representing the transition

$$(nl)^w k_i l_i \rightarrow (nl)^{w-1} k_e l_e k_f l_f, \tag{1.13}$$

where w is the occupation number of the initial subshell being ionized, $k_i l_i$ are the quantum numbers of the incident electron, while $k_e l_e$ and $k_f l_f$ are the quantum numbers for the ejected and final continuum electrons respectively. The configuration-average direct cross section is given by

$$\sigma = \frac{32\omega}{k_i^3} \int_0^{E/2} \frac{d(k_e^2/2)}{k_e k_f} \sum_{l_i, l_e, l_f} (2l_i+1)(2l_e+1)(2l_f+1) P(l_i, l_e, l_f, k_i, k_e, k_f), \tag{1.14}$$

where $E = \frac{1}{2}(k_e^2 + k_f^2)$ and P is the first order scattering probability which is described in more detail previously [48].

There are commonly two different approximations made for the scattering potential which the incident, scattered and ejected electrons experience. In what will be referred to as the DWIS(N) method, the incident and scattered electrons are evaluated in a V^N potential, with the ejected continuum electron calculated in a V^{N-1} potential, where N is the number of electrons in the initial target. Alternatively, one can calculate the incident, scattered and ejected electrons in a V^{N-1} potential, labeled as DWIS(N-1). We use the DWIS(N-1) method throughout this paper.

The configuration-average distorted-wave method can also be used to calculate the excitation-autoionization contribution [48]. In the configuration-average approach, the excitation process is represented by

$$(n_1 l_1)^{w_1+1}(n_2 l_2)^{w_2-1} k_i l_i \rightarrow (n_1 l_1)^{w_1}(n_2 l_2)^{w_2} k_f l_f, \tag{1.15}$$

where $n_1 l_1$ and $n_2 l_2$ are quantum numbers of the bound electrons, and $k_i l_i$ and $k_f l_f$ are quantum numbers of the initial and final continuum electrons respectively. The configuration-average excitation cross section is given by

$$\sigma_{exc} = \frac{8\pi}{k_i^3 k_f}(w_1+1)(4l_2+3-w_2)\sum_{l_i,l_f}(2l_i+1)(2l_f+1)P(l_i,l_f,k_i,k_f) \tag{1.16}$$

where P is the first order scattering probability [48]. While we calculate distorted-wave cross sections for the direct ionization and excitation-autoionization of Al^{2+}, we do not evaluate any REDA or READI contributions. We note that it has already been shown that DW ionization cross sections after overestimate the total cross section[8] for near neutral systems. Here we include the DW results as a comparison to our new R-matrix results.

1.4 R-matrix theory

R-matrix theory was first introduced in 1946 and 1947 by Wigner and Eisenbud [52, 53] in the context of describing nuclear resonance reactions. In the 1960s there was the realization

that these same techniques could be applied to the resonance processes in electron-atom/ion scattering. As a result, R-matrix theory as an *ab initio* method to describe electron-atom/ion collisions was formally described by Burke and colleagues in a series of papers in in the early 1970s, for example [54]. The fundamental concept of R-matrix theory is the partitioning of configuration space into 2 regions. For electron atom/ion collisions, a sphere of radius $r = a_0$ separates an internal region from an external region, r being the radial distance of the incident or scattered electron from the target nucleus. The radius a_0 of the sphere is usually chosen so that it encompasses the charge distributions of the target eigenstates, or more simply, the radial extent of the most diffuse orbital in the target.

In the internal region, where electron exchange and correlation effects between the scattered electron and the target electrons are important, a configuration interaction basis expansion of the total wave function is adopted.

For all the calculations presented within this thesis, the atomic structure package AUTOSTRUCTURE [55] was used to generate the spectroscopic radial orbitals subsequently employed in the scattering calculation. The wavefunction representing close-coupling expansion in the inner region is given by:

$$\Psi_k^{N+1} = A \sum_{i,j} a_{ijk} \psi_i^{N+1} \frac{u_{ij}(r_{N+1})}{r_{N+1}} + \sum_i b_{ik} \chi_i^{N+1} \ , \tag{1.17}$$

where A is an antisymmetrization operator, ψ_i^{N+1} are channel functions obtained by coupling N-electron target states with the angular and spin functions of the scattered electron, $u_{ij}(r)$ are radial continuum basis functions, and χ_i^{N+1} are bound functions which ensure completeness of the total wavefunction. The radial continuum basis orbitals u_{ij} are now defined only over the range $0 \leq r \leq a_0$. They represent the radial motion of the scattered electron in the internal region and are chosen to vanish at the origin and are in general non-zero on the boundary $r = a_0$ of the internal region, thus providing a link between the solutions in the internal and external regions. The χ_i^{N+1} terms are also referred to a square integrable or correlations terms, and as they are constructed only from target orbitals, and therefore

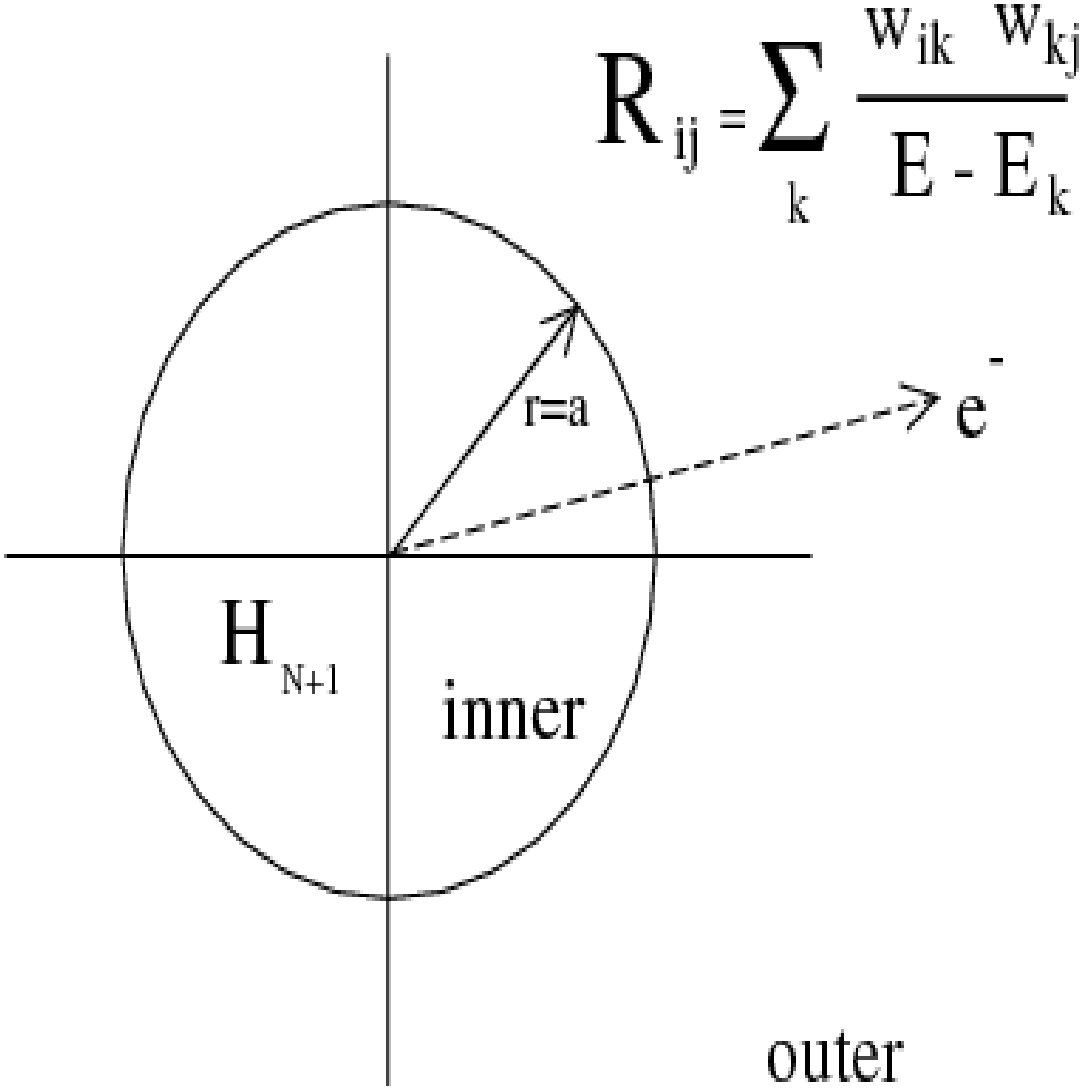

Figure 1.5: Overview of the R-matrix inner and outer region definitions

will also have a negligible value on the the R-matrix boundary. The coefficients a_{ijk} and b_{ik} are determined by diagonalization of the total (N+1)-electron symmetric Hamiltonian. The availability of modern supercomputing architectures and the current codebase permits the concurrent parallel diagonalization of every Hamiltonian utilizing ScaLapack libraries [56]. This has greatly opened up the applicability of the method to diverse set of complex atomic targets. The resulting eigenvalues and eigenvectors are subsequently used in the formation of the R-matrix, which acts as the interface between the inner and outer region is given by:

$$R_{ij}(E) = \frac{1}{2a_0} \sum_k \frac{w_{ik} w_{jk}}{E - E_k} \tag{1.18}$$

where E_k are the aforementioned eigenvalues of the $N+1$ electron Hamiltonian and w_{ik} are referred to as surface amplitudes. The w_{ik} are given by the following expression, where c_{ijk} correspond to the eigenvectors of the aforementioned Hamiltonian.

$$w_{ik} = \sum_j u_{ij} c_{ijk} \quad \text{at} \quad \text{r} = \text{a}_0 \tag{1.19}$$

The R-matrix relates the reduced radial wave function $F_i(r)$, describing the radial motion of the scattered electron in the ith channel, to its derivative on the boundary $r = a_0$.

$$F(r) = \sum_j R_{ij} (a_0 \frac{dF_j}{dr} - bF_j) \quad \text{at} \quad \text{r} = \text{a}_0 \tag{1.20}$$

In the external region, $r > a_0$, the scattered electron wave function satisfies the following radial equations

$$(\frac{d^2}{dr^2} - \frac{l_i(l_i+1)}{r^2} + \frac{2Z}{r} + k_i^2) F_i(r) = 2 \sum_j^n V_{ij}(r) F_j(r) \tag{1.21}$$

where both i and j sum over the n coupled channels of the close-coupling expression, and $k_i^2 = 2(E - E_i^N)$. The direct potential V_{ij} is defined by:

$$V_{ij} =< \psi_i^{N+1} | \sum_k^N \frac{1}{r_{kN}} | \psi_j^{N+1} > \tag{1.22}$$

where the integration is carried out over all co-ordinates except those of the $N+1$ electron. We can use the expansion:

$$\sum_k^N \frac{1}{r_{kN}} = \sum_{\lambda=0}^{\infty} \sum_{k=1}^{N} r_k^{\lambda} P_{\lambda}(cos\theta_{kN+1}) \tag{1.23}$$

where in practice, the summation over λ usually includes only the dipole and quadrapole terms. The only appreciable contribution to the integration for V_{ij} comes from the region $r_k < a_0$, and therefore V_{ij} can be constructed from target N electron dipole matrix elements multiplied by the appropriate angular algebra. The $n \times n$ R-matrix on the boundary can subsequently be related to the asymptotic form $n \times n$ K or S matrix from which cross sections may be derived, taking into account whether the system is a neutral or an ionic target. The final cross section in LS coupling for a transition from one state $\alpha_i L_i S_i$ to another $\alpha_j L_j S_j$ is given by

$$\sigma_{i \to j} = \frac{\pi}{k_i^2} \sum_{l_i, l_j} \frac{(2L+1)(2S+1)}{(2L_i+1)(2S_i+1)} |S_{ij} - \delta_{ij}|^2 \tag{1.24}$$

The strength of the R-matrix method is that it requires a single diagonalization for each partial wave, regardless of the number of the incident electron energies.

1.5 R-matrix with PseudoState calculations

An extension to the standard R-matrix method to include the effects of high Rydberg and continuum states in the representation of the target, and to provide coupling to the continuum was proposed over 40 years ago [57], but implemented for the general case more recently by Hudson and Bartschat [58], Gorczyca and Badnell [59]. In addition to a finite choice of low-lying target states, higher Rydberg states and the target continuum are

now represented using non-orthogonal Laguerre pseudo-orbitals. They are subsequently orthogonalized to the spectroscopic orbitals and to each other. These pseudo-orbitals do not have spectroscopic eigenvalues, and range in terms of energy, from being slightly bound to having values several times the ionization threshold. They only agree with their spectroscopic counterparts in having the same number of radial nodes. As shown in the figure 1.6, these pseudo-states span the energy range above the ionization limit, and are said to provide a discretization of the continuum. The choice of pseudostates required is dependent on the collisional process involved, the energy range and the angular momentum of the initial term/level

In our implementation of the RMPS method, the basis used to represent the $(N+1)$-electron continuum was made orthogonal to the pseudo orbitals using a method developed by Gorczyca and Badnell[59]. The scattering calculation was performed with our set of parallel R-matrix programs[60, 61], which are extensively modified versions of the serial RMATRIX I programs[62]. For the present RMPS ionization work presented in this thesis, the ionization cross sections are simply defined as the summation from the initial terms to those terms above the respective ionization limits. In has been shown that for near-neutral systems that non-perturbative methods such as the RMPS are required to accurately model the ionization cross sections at low energies. Another benefit of the R-matrix approach, is that a single calculation also provides the metastable ionization cross sections from every term, though metastable ionization requires considerably more partial waves that the ground state ionization cross section to achieve a converged result.

1.6 Time-Dependent Close-Coupling method

In our Al and Al^{2+} calculations we also present results from the time-dependent close coupling method. This approach is described in more detail in the review article by Pindzola et al. [63].

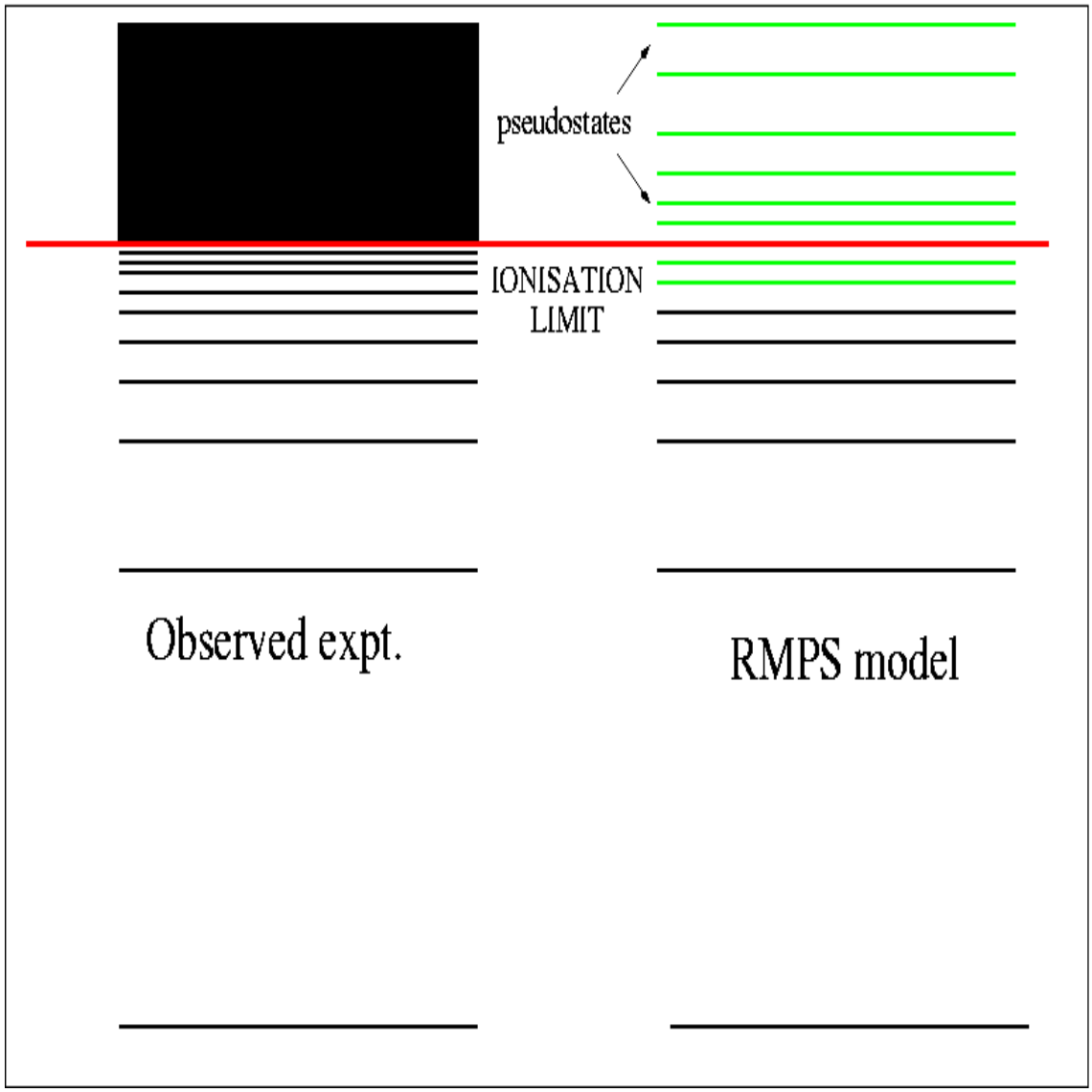

Figure 1.6: R-matrix with pseudostate model

1.6.1 Time-dependent calculations on a 2D numerical lattice

The time-dependent Schrödinger equation for electron scattering from a one-electron atom is

$$\frac{\partial\Psi(\overrightarrow{r_1},\overrightarrow{r_2},t)}{\partial t} = H_{system}\Psi(\overrightarrow{r_1},\overrightarrow{r_2},t) \tag{1.25}$$

where H_{system} is the non-relativistic Hamiltonian for the scattering system, which is given by

$$H_{system} = \sum_{i=1}^{2}(-\frac{1}{2}\nabla_i^2 - \frac{Z}{r_i}) + \frac{1}{|\overrightarrow{r_1} - \overrightarrow{r_2}|} \tag{1.26}$$

where Z is the nuclear charge and $\overrightarrow{r_1}$, $\overrightarrow{r_2}$ are the coordinates for the two electrons. If we expand the electronic wave function in LS coupling, we will have

$$\Psi^{LS}(\overrightarrow{r_1},\overrightarrow{r_2},t) = \sum_{l_1,l_2}\frac{P^{LS}_{l_1l_2}(\overrightarrow{r_1},\overrightarrow{r_2},t)}{r_1r_2}\sum_{m1,m2}C^{l_1l_2L}_{m_1m_20}Y_{l_1m_1}(\hat{r_1})Y_{l_2m_2}(\hat{r_2}) \tag{1.27}$$

where $C^{l_1l_2l_3}_{m_1m_2m_3}$ is a Clebsch-Gordan coefficient and $Y_{lm}(\hat{r})$ is a spherical harmonic. Then we put this wave function into the time-dependent Schrödinger equation, we will get the time-dependent close-coupled partial differential equation,

$$i\frac{\partial P^{LS}_{l_1l_2}(r_1,r_2,t)}{\partial t} = T_{l_1l_2}(r_1,r_2)P^{LS}_{l_1l_2}(r_1,r_2,t) + \sum_{l_1',l_2'}V^{L}_{l_1,l_2,l_1',l_2'}(r_1,r_2)P^{LS}_{l_1'l_2'}(r_1,r_2,t) \tag{1.28}$$

where

$$T_{l_1l_2}(r_1,r_2) = \sum_{i=1}^{2}(-\frac{1}{2}\frac{\partial^2}{\partial r_i^2} + \frac{l_i(l_i+1)}{2r_i^2} - \frac{Z}{r_i}) \tag{1.29}$$

and the coupling operator is given in terms of 3i and 6j symbols by

$$V^{L}_{l_1l_2,l_1'l_2'}(r_1,r_2) = (-1)^{l_1+l_1'+L}\sqrt{(2l_1+1)(2l_1'+1)(2l_2+1)(2l_2'+1)} \tag{1.30}$$

$$\times\sum_{\lambda}\frac{(r_1,r_2)^{\lambda}_{<}}{(r_1,r_2)^{\lambda+1}_{>}}\begin{pmatrix} l_1 & \lambda & l_1' \\ 0 & 0 & 0 \end{pmatrix}\begin{pmatrix} l_2 & \lambda & l_2' \\ 0 & 0 & 0 \end{pmatrix}\begin{Bmatrix} l_1 & l_2 & L \\ l_2' & l_1' & \lambda \end{Bmatrix} \tag{1.31}$$

For electron scattering from a one-electron atom, the initial condition to the solution of the TDCC equations are

$$P^{LS}_{l_1 l_2}(r_1, r_2, t = 0) = P_{nl}(r_1) G_{k_0 l'}(r_2) \delta_{l_1,l} \delta_{l_2,l'} \tag{1.32}$$

where $P_{nl}(r)$ is a bound radial wave function for a one-electron atom and the Gaussian wave packet, $G_{k_0 L}(r)$, has a propagation energy of $\frac{k_0^2}{2}$. Probabilities for all the many collision process possible are obtained by $t \to \infty$ projection onto fully antisymmetric spatial and spin wavefunctions. The partial collision probability for electron single ionization of the hydrogen atom is,

$$\mathcal{P}_{l_1 l_2 L, s_1 s_2 S}(t) = \sum_{k_1} \sum_{k_2} |R(12, t) + (-1)^S R(21, t)|^2 \tag{1.33}$$

where

$$R(ij, t) = \int_0^\infty dr_1 \int_0^\infty dr_2 P_{k_1 l_1}(r_i) P_{k_2 l_2}(r_j) P^{LS}_{l_1 l_2}(r_1, r_2, t) \tag{1.34}$$

Because that the spatial and spin dependence of the time-dependent wavefunction may be separated for two electron systems, the initial condition of the solution for the TDCC equations is given by

$$P^{LS}_{l_1 l_2}(r_1, r_2, t = 0) = \sqrt{\frac{1}{2}} (P_{nl}(r_1) G_{k_0 l'}(r_2) \delta_{l_1,l} \delta_{l_2,l'} + (-1)^S G_{k_0 l'}(r_1) P_{nl}(r_2) \delta_{l_1,l} \delta_{l_2,l'}) \tag{1.35}$$

The same as above, probabilities for all the many collision processes possible are obtained by $t \to \infty$ projection onto spatial product wavefunctions. Now the probability is given by

$$\mathcal{P}_{l_1 l_2 L, s_1 s_2 S}(t) = \sum_{k_1} \sum_{k_2} |R(12, t)|^2 \tag{1.36}$$

Then the total cross section for the electron single ionization of the hydrogen atom is given by

$$\sigma_{sion} = \frac{\pi}{4k_0^2} \sum_{L,S} (2L + 1)(2S + 1) \mathcal{P}^{LS}_{sion} \tag{1.37}$$

We can get $\mathcal{P}_{sion}^{LS}$ by summing over all $l_1 l_2$ partial collision probabilities.

Chapter 2

Electron-impact ionization of neutral Al and Al^+

Electron-impact ionization cross sections for neutral atoms present considerable difficulties for both experimentalists and theorists. On the theoretical side, the use of perturbative methods usually produces cross sections that are spuriously high, while non-perturbative calculations often require massively parallel computers. The results from non-perturbative methods have been shown to give excellent agreement with a range of experimental measurements of neutral systems [64, 65, 66, 67]. The calculations are challenging due to the size of the box required for neutral species and the difficulty in achieving a good target structure for a neutral system. On the experimental side, very few measurements have been performed for neutral species and few facilities remain that can measure neutral ionization cross sections.

In this chapter we focus on the electron-impact ionization of neutral Al and Al^+. As mentioned in the previous chapter, the electron-impact ionization of Al is important for current impurity transport studies on the Madison Symmetric Torus [68], which has Al walls. Al atoms from the walls can be ablated into the plasma and are transported through to the core plasma, where the Al ions can reduce the energy confinement in the plasma through radiative losses. When modeling such impurity transport, one needs accurate ionization and recombination rate coefficients. The only experimental cross section measurements available are part of the comprehensive paper of Freund et al. [2]. The only published theoretical data available for this atom are the generalized oscillator strength calculations of McGuire [11]. When compiling their new ionization datasets, both Mattioli et al. [28] and Dere [12] used the measurements of Freund [2] when making rate coefficients for neutral Al. It is important to have a theoretical check on the cross section measurements using non-perturbative methods. In the following section, and in the next chapter, it may be useful to refer to the data

given in Appendix A, showing the configuration-average direct ionization channels and their configuration-average ionization potentials.

2.1 Neutral Al

2.1.1 Configuration-average distorted-wave calculations

We first calculated CADW cross sections for direct ionization of the $3p$ and $3s$ subshells of Al using Eq. 1.14. All energies and bound radial orbitals for Al were calculated using a Hartree-Fock relativistic (HFR) atomic structure code[69]. For direct ionization of the $3p$ and $3s$ subshells of Al, we included $l_i = 0 - 50$, $l_e = 0 - 8$, and $l_f = 0 - 50$ in the partial wave sums in Eq. 1.14. The incident, ejected, and final scattered electrons are evaluated in a V^{N-1} potential[70], where $N = 13$ for Al. The HFR ionization potential for the $3p$ subshell is 6.15 eV, while for the $3s$ subshell it is 10.85 eV. The CADW direct ionization cross sections for Al are presented in Figure 1. The sum of the CADW $3l$ direct ionization cross sections are within the error bars of experiment[2] from 11 eV to 30 eV. However, as will be seen the agreement is much worse when excitation-autoionization contributions are considered.

CADW cross sections for excitation were calculated of the $3s$ subshell of Al using Eq. 1.16. For excitation of Al, we included $l_i = 0 - 50$ and $l_f = 0 - 50$ in the partial wave sums of Eq. 1.16, and used a V^N potential for the incident and final scattered electrons. The HFR excitation energy for the $3s \rightarrow 3p$ transition is 4.68 eV, for the $3s \rightarrow 3d$ transition it is 9.01 eV, while for the $3s \rightarrow 4l$ transitions it ranges from 7.92 eV to 9.98 eV. Although the configuration-average energy finds $Al^*(1s^2 2s^2 2p^6 3s 3p^2)$ bound relative to $Al^+(1s^2 2s^2 2p^6 3s^2)$, the more accurate NIST data compilation[71] finds the $Al^*(1s^2 2s^2 2p^6 3s 3p^2)$ ^4P and ^2D terms below and the ^2S and ^2P terms above the $Al^+(1s^2 2s^2 2p^6 3s^2)$ ^1S term ionization limit. Therefore, we included the $3s \rightarrow 3p$ transitions by scaling the configuration-average cross section by (2/30) for the ^2S term, where 2 is the statistical weight of the term and 30 is the statistical weight of the configuration, and by (6/30) for the ^2P term, where 6 is the

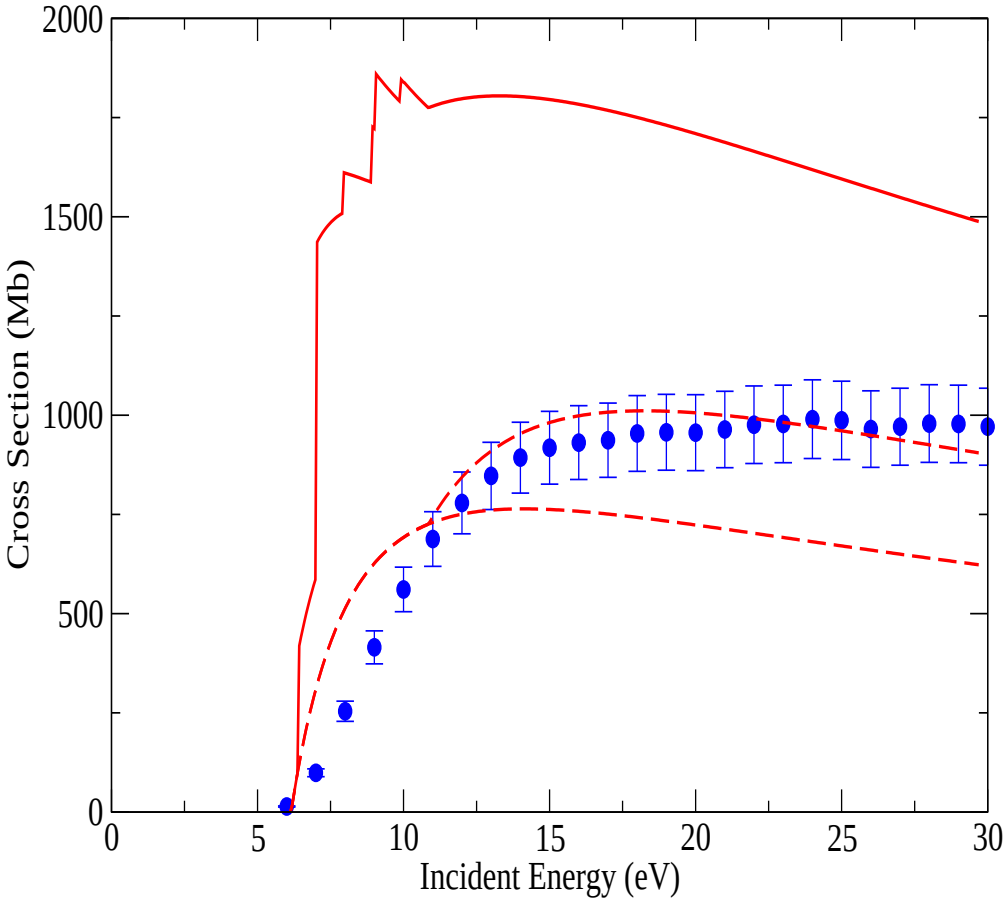

Figure 2.1: Electron-impact single ionization of Al. Lower dashed (red) line: CADW $3p$ direct ionization, upper dashed (red) line: CADW $3s$ and $3p$ direct ionization, solid (red) line: CADW total ionization, (blue) circles: measurements[2] (1.0 Mb = 1.0×10^{-18} cm^2).

statistical weight of the term and 30 is again the statistical weight of the configuration, and by using the NIST excitation energies. The CADW total ionization cross sections for Al, that is the sum of $3l$ direct cross sections and the $3s \rightarrow nl$ indirect excitation-autoionization cross sections, are presented in Figure 1. The CADW total cross sections are almost a factor of 2 higher than experiment[2] over a wide energy range.

2.1.2 RMPS and TDCC calculations

RMPS cross sections were then calculated for the total ionization of the $3p$ and $3s$ subshells of Al using Eqs.1.24. All energies and bound radial orbitals for Al were generated using the atomic structure package AUTOSTRUCTURE [55], using a Thomas-Fermi-Dirac-Amaldi statistical potential and orbital scaling parameters to optimize the atomic structure of the target. In the RMPS calculation we included the $1s^2 2s^2 2p^6 3s^2 nl$ and $1s^2 2s^2 2p^6 3s 3pnl$ configurations, where $3p \leq nl \leq 12g$ $(0 \leq l \leq g)$. We use spectroscopic orbitals up to $4p$ and pseudo-orbitals for the higher subshells. We also included the $1s^2 2s^2 2p^6 3p^3$ configuration to improve the target structure. We used orbital scaling parameters for the $2p$, $3s$ and $3p$ orbitals (λ_{2p}=0.92, λ_{3s}=1.0672 and λ_{3s}=0.96) to further improve the atomic structure. There are 404 LS terms in our target structure and for our scattering calculation we included partial waves for $L = 0 - 25$. The contribution from higher partial waves were estimated for dipole transitions using the Burgess method[72] and for non-dipole transitions assuming a geometric series in L, using energy ratios, with special procedures for addressing transitions between near degenerate LS terms. We used a basis set of $u_{ij}(r)$ in Eq. 1.17 that gives a maximum node energy of 50 eV, thus we estimate that the calculation should be valid up to about 35 eV incident energy. The RMPS total ionization cross sections for Al are presented in Figure 2.2. The RMPS total cross sections are found to be in good agreement with experiment[2] over the entire energy range.

To better understand direct and indirect contributions to the total ionization of Al, we calculated TDCC cross sections for direct ionization of the $3p$ and $3s$ subshells of Al.

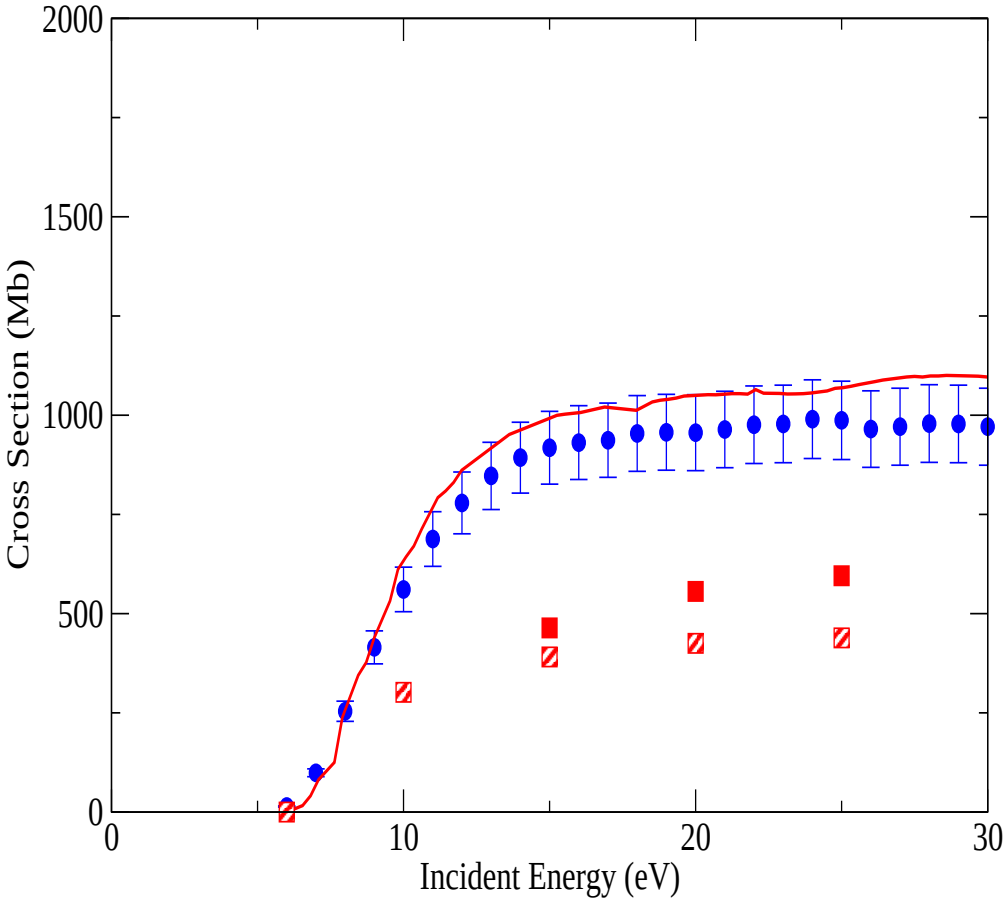

Figure 2.2: Electron-impact single ionization of Al. Lower dashed (red) squares: TDCC $3p$ direct ionization, upper solid (red) squares: TDCC $3s$ and $3p$ direct ionization, solid (red) line: RMPS total ionization, (blue) circles: measurements[2] (1.0 Mb = 1.0×10^{-18} cm^2).

The $V_{ij}(r)$ potential of Eq.1.23 was constructed using Hartree-Fock bound orbitals for the $1s^2 2s^2 2p^6 3s^2$ and $1s^2 2s^2 2p^6 3s3p$ configurations of Al^+[73]. For both cases, the active target orbital and the rest of the excited state spectrum is obtained by diagonalization of the one electron Hamiltonian optimized on experimental removal energies[71], with the introduction of $l = 0$ and $l = 1$ pseudo-potentials to remove the problem of de-excitation to filled subshells[63]. For direct ionization of the $3p$ subshell, the number of LS symmetries is $(3pks)\ ^{1,3}P$ and $(3pkl)\ ^{1,3}L$ with $L = l-1, l, l+1$ for $l = 1-5$. For direct ionization of the $3s$ subshell, the number of LS symmetries is $(3skl)\ ^{1,3}L$ with $L = l$ for $l = 1-5$. As many as 19 coupled channels were propagated on a 500×500 point radial lattice with a uniform mesh spacing of $\Delta r = 0.20$. CADW calculations were used to "topup" the TDCC calculations for $l \geq 6$. The TDCC direct ionization cross sections for Al are presented in Figure 2.2. The sum of the TDCC $3l$ direct ionization cross sections are almost a factor of 2 lower than experiment[2] over a wide energy range. We note that RMPS excitation cross sections may be approximately calculated by summing the full 404 LS term results only over the $1s^2 2s^2 2p^6 3s3pnl$ configurations involving the $3p$, $3d$, $4s$, and $4p$ spectroscopic orbitals whose LS terms are above the ionization limit. Subtracting the RMPS excitation cross sections from the RMPS total ionization cross sections yields direct ionization cross sections that are in good agreement with the TDCC ($3s$ and $3p$) direct ionization results over the whole energy range.

In summary, we have carried out perturbative distorted-wave and non-perturbative close-coupling calculations for direct and total electron-impact ionization cross sections of the ground state of the neutral Al atom. Comparison of the CADW and TDCC results for the direct ionization of the $3l$ subshells indicates a strong correlation effect for the ejection of a target electron into the continuum. In fact, the factor of 2 decrease is one of the largest seen in all the atoms studied to date. Comparison of the CADW and RMPS results for the total ionization of the $3l$ subshells indicates a strong correlation effect for the excitation of a target

electron into autoionizing states. Comparison of the TDCC direct and RMPS total ionization cross sections indicate that the direct ionization and indirect excitation-autoionization contributions are almost the same strength for Al. Finally, the good agreement found between the RMPS total ionization cross sections and experiment[2] confirms the validity of the ionization rate coefficients found in recent datasets[28, 12] for the ground state of neutral Al.

2.2 Al^+

The theoretical and experimental results for Al^+ are shown in Fig 2.3 . Al^+ has a ground configuration of $1s^2 2s^2 2p^6 3s^2$. Table I show the direct ionization potential for the ground configuration of Al^+. The dominant ionization is from 3s subshell. Al^+ cross sections were measured by Montague et al.[4] and Belic et al.[3]. Excitation-autoionization contributions were calculated using the R-matrix method by Tayal and Henry [74] and the total direct ionization and excitation-autoionization contribution was recently calculated using the R-matrix with pseudostates (RMPS) method and the Time-Dependent Close-Coupling (TDCC) method by Ludlow et al. [75]. While DW calculations for Al^+ are in reasonable agreement with the experimental measurements, the non-perturbative calculations are in agreement with each other but are lower than the experimental measurements. Given that DW calculations usually overestimate the ionization cross sections for singly ionized systems, this suggests that the experimental measurements may be too high for Al^+.

In the Figure 2.3, we can see that experimental results match the distorted-wave calculation very well while the RMPS and TDCC results of Ludlow et al. [75] are both higher than the experimental measurements. However, considering the poor performance of distorted-wave calculations for other near-neutral system[76, 77], a more careful consideration is required. Nonperturbative methods such as TDCC and RMPS are needed. In Fig. we can see that the TDCC and RMPS results are in good agreement with each other, which is about

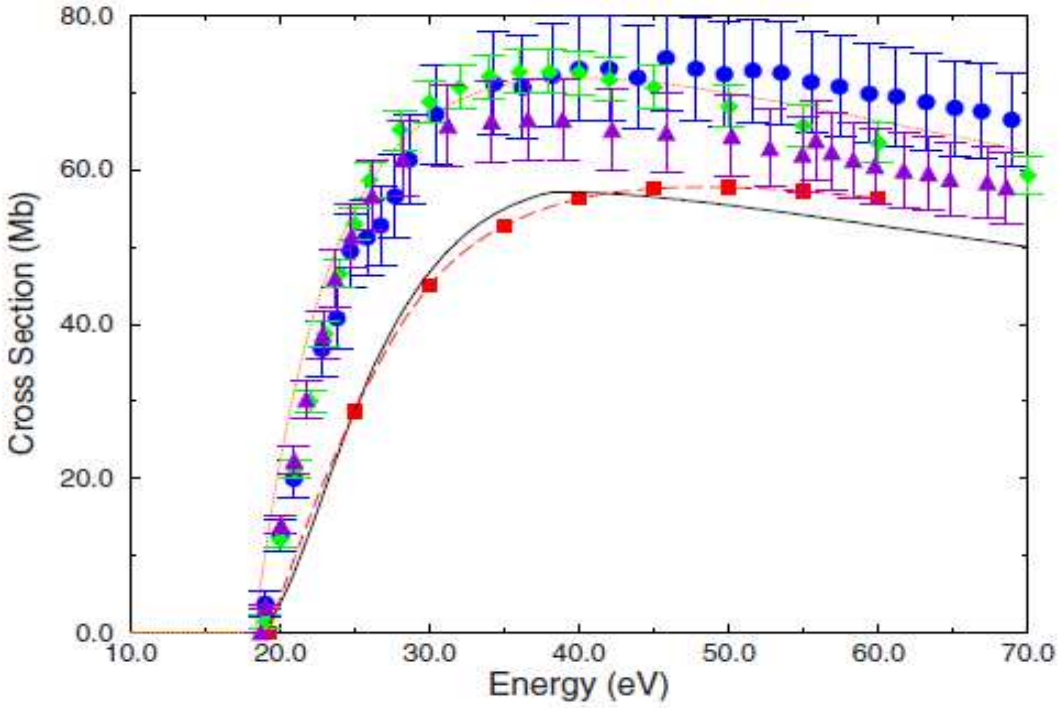

Figure 2.3: Electron-impact ionization cross section for Al+. Dotted curve: distorted-wave, solid squares: TDCC, solid curve: RMPS, solid circles: experiment [3], solid diamonds: experiment [4], and solid triangles: experiment [5].

20% below distorted-wave at the peak. The TDCC result is higher than RMPS data at larger energies.

Chapter 3

Electron-impact ionization of Al^{2+} through to Al^{12+}

In this chapter we complete the ionization cross section calculations required for the remaining Al ionization stages.

3.1 Al^{2+}

In this section we focus on resolving discrepancies between the currently available theoretical cross section data and experimental measurements of the electron-impact single ionization of Al^{2+}. Ionization of Al^{2+} has been previously studied both experimentally and theoretically. Al^{2+} cross sections were first measured by Crandall et al. [6]. The direct ionization for this ion was calculated using the distorted-wave (DW) method by Younger [78] and distorted-wave data for the excitation-autoionization of the 2p subshell were calculated by Griffin et al.[79]. The total DW cross sections were significantly higher than the experimental measurements, as one might expect for a doubly ionized system. Badnell et al. [8] then presented results from three non-perturbative calculations of the 3s ionization, using the RMPS, Time-Dependent Close-Coupling (TDCC), and Convergent Close-Coupling (CCC) methods. These were found to be in reasonable agreement with each other, about 30% higher than the measurements of Crandall et al. [6], and significantly lower than the distorted-wave cross sections. Thomason and Peart [7] then measured the ionization cross section with results that were in excellent agreement with the non-perturbative results of Badnell et al. [8] at energies where the 3s direct ionization dominates, and higher than the previous measurements of Crandall et al. [6]. Thomason and Peart also measured the cross section at a fine-energy resolution to map out the indirect ionization contributions due to excitation of the 2p subshell. They found that configuration-average distorted-wave

(CADW) calculations of the indirect contribution were much larger than their measured values. The two-state close-coupling calculations of Henry and Msezane [80] were closer to their measurements, but were still higher than the experimental values. Teng [9] then performed RMPS calculations for the direct ionization of the 3s subshell and for the indirect ionization of the 2p subshell. Teng [9] used scaled DW cross sections for the 2p direct ionization. One of the unique aspects of the high resolution scan performed by Thomason and Peart [7] was that such resonant features were observed in the total cross sections. Teng [9] showed theoretically that REDA did contribute a significant fraction to the indirect ionization and also showed that READI made a small contribution for this ion. These theoretical results matched the shape of the indirect contributions, including features that corresponded to resonant excitation double autoionization, but were still higher than the measured values. Explaining the experimental cross sections for Al^{2+} above 80 eV is still an open question and is the subject of this section.

3.1.1 RMPS and TDCC calculations for Al^{2+}

Al^{2+} has been extensively studied previously, and while non-perturbative calculations have shown good agreement with the lower energy measurements of Thomason and Peart [7], there is still significant disagreement in the region where indirect ionization due to the 2p subshell contributes to the total cross section. We used the multi-configuration Breit-Pauli structure code AUTOSTRUCTURE[55] to generate our radial orbitals in a Thomas-Fermi Amaldi-Dirac potential. To investigate this, we set up three RMPS calculations. The first one calculated just the 3s direct ionization using a set of $2p^6$ nl configurations, where 3s$<$ nl $<$ 14h ($0 \leq l \leq$ h). We used spectroscopic orbitals up to the 5g subshell and pseudostates for the higher subshells. In our AUTOSTRUCTURE calculation, we used the orbital scaling parameters for the pseudo-orbitals to achieve an even spread of the pseudostates across the ionization potential. We used the following scaling parameters for our radial pseudostates : $\bar{n}s$=0.99, $\bar{n}p$=0.92, $\bar{n}d$=0.82, $\bar{n}f$=0.84, $\bar{n}g$=0.9, $\bar{n}h$=1.12. We refer to this calculation as

$RMPS_{3s}$. Thus, this is a similar calculation to the RMPS calculation of Badnell et al. [8], though much larger in size.

Our second RMPS calculation for this ion used the $2p^5 3s nl$ configurations, where $3s < nl < 13g$ ($0 \leq l \leq g$). We used spectroscopic orbitals up to the 3d subshell, pseudostates for the higher subshells and used orbital scaling parameters for the s and p pseudo-orbitals to evenly distribute their terms over the ionization potential. We note that we chose hydrogenic scaling parameters for the remaining d, f and g pseudo-orbitals, otherwise the size of the R-matrix box would be too large. We used $\bar{n}s$=1.08, $\bar{n}p$=1.02. We refer to this calculation as $RMPS_{2p}$. While this calculation has both direct ionization of the 2p and excitation-autoionization of the 2p subshell, many Auger channels for the resonances attached to the excited configurations are missing, meaning that the heights of these resonant features may be artificially large. These channels were also missing from the calculation of Teng [9], and it was postulated in that paper that this was the reason that the RMPS results were higher than the experiment of Thomason and Peart [7].

Thus, our third RMPS calculation included the $2p^6$ nl and $2p^5 3s nl$ configurations, where $3s < nl < 14g$. We used spectroscopic orbitals up to 3d and pseudostates for the higher subshells and used orbital scaling parameters to evenly distribute the s and p pseudo-orbitals over the ionization potential ($\bar{n}s$=1.03, $\bar{n}s$=1.04). Thus, this calculation includes both the direct ionization of the 3s and 2p subshells, and the indirect processes associated with the 2p subshell. Due to the inclusion of the $2p^6$ nl pseudostates in the calculation, we allow for Auger decay of the REDA and READI resonant features in the 2p indirect ionization cross section. We also shift the following term energies in the prediagonalization of the (N+1) Hamiltonian of the RMPS calculation, to match NIST values: $2p^5 3s^2$ (^{2}P), $2p^5 3s3p$(^{4}D, ^{4}P, ^{2}D, ^{2}P), $2p^5 3p^2$($^2P^o$, $^4D^o$), and $2p^5 3s3d$($^4P^o$, $^4F^o$, $^4D^o$, $^2D^o$, $^2P^o$). We refer to this calculation as $RMPS_{3s2p}$.

Table 3.1 shows the energies of the terms that are expected to provide the dominant contribution to excitation-autoionization and their corresponding NIST energies. Figure

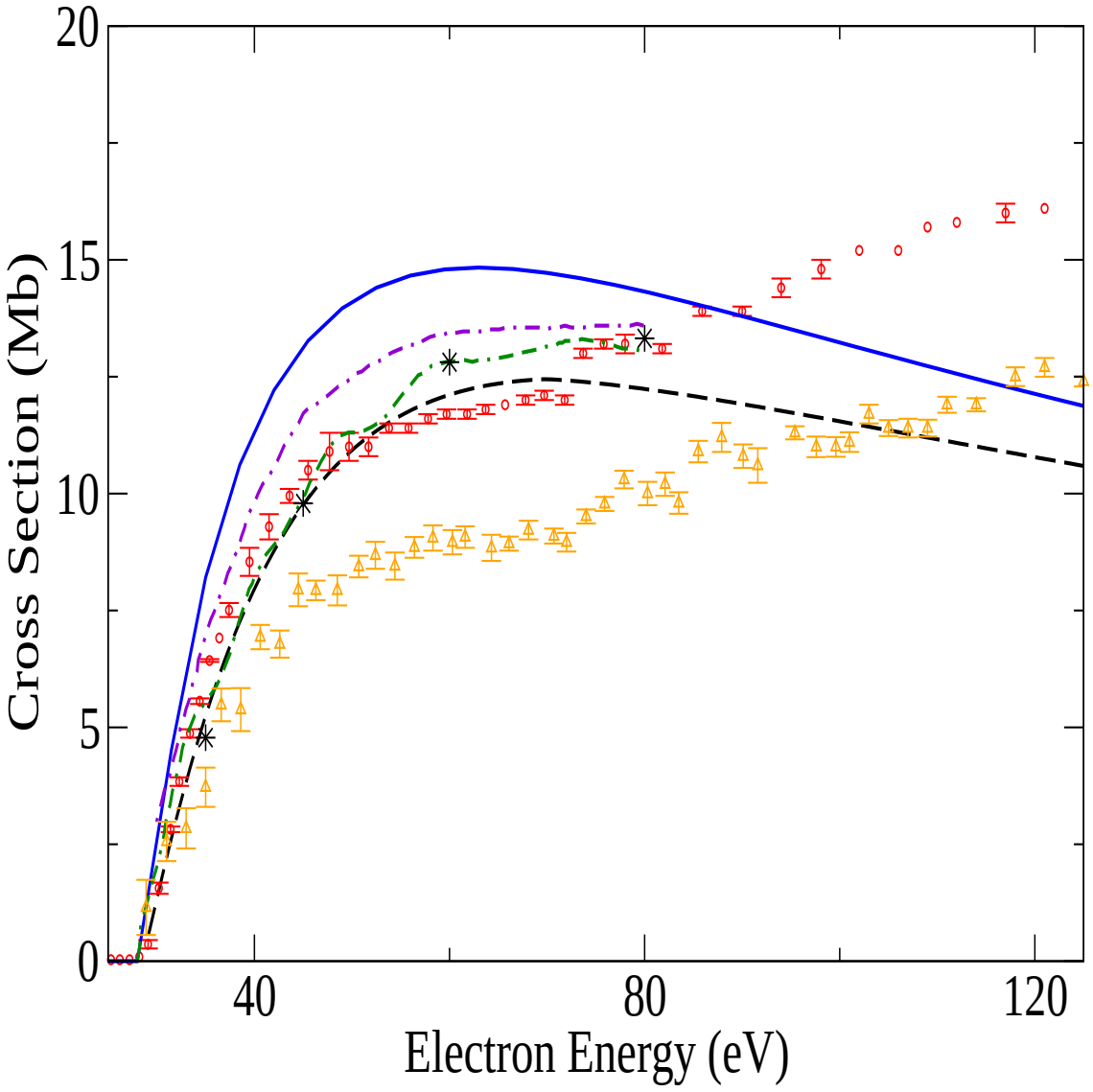

Figure 3.1: Electron-impact ionization cross section for Al^{2+}. The dashed curve(black) shows the $RMPS_{3s}$ calculations. The solid curve(blue) shows the DW results for the 3s ionization only. The up triangles(yellow) show the experimental measurements of Crandall et al. [6], and the circles(red) show the experimental measurements of Thomason and Peart [7]. Also shown are the RMPS (double-dash dot line(green)), TDCC (stars(black)) and CCC (dash-dot line(purple)) results from Badnell et al. [8]

configuration	AUTOSTRUCTURE result (Ry)	NIST value(Ry)	Difference(%)
$2p^5 3s^2(^2P^o)$	5.456794	5.3734	1.55
$2p^5 3s3p(^4S)$	5.719620	5.6978	0.38
$2p^5 3s3p(^4D)$	5.793384	5.77433575	0.33
$2p^5 3s3p(^4P)$	5.840355	5.81294	0.47
$2p^5 3s3p(^2D)$	5.860121	5.839	0.36
$2p^5 3s3p(^2P)$	5.876833	5.854	0.39
$2p^5 3s3d(^4P^o)$	6.566398	6.52413	0.65
$2p^5 3s3d(^4F^o)$	6.583279	6.52743	0.86
$2p^5 3s3d(^4D^o)$	6.611779	6.564	0.73
$2p^5 3s3d(^2D^o)$	6.645	6.60235	0.65
$2p^5 3s3d(^2P^o)$	6.654120	6.620485	0.51

Table 3.1: Term Energies from AUTOSTRUCTURE model RMPS_{3s2p} and corresponding NIST energies

3.1 shows the results for the two experimental measurements, along with previous theoretical results for the direct ionization of the 3s subshell. We also show the results from our RMPS_{3s} calculation. We note that our RMPS_{3s} are in good agreement with the previous non-perturbative calculations (RMPS and TDCC) of Badnell et al. [8], and are in good agreement with the experimental measurements of Thomason and Peart [7] at energies below which the 2p subshell starts to contribute, about 75 eV. This again supports the previous conclusion that the measurements of Crandall et al. [6] are spuriously low. Distorted-wave results have already been shown to be higher than both the experimental measurements and the non-perturbative theoretical results[8].

Figure 3.2 shows our RMPS_{2p} results. For clarity in the plot we show only the experimental results of Thomason and Peart [7]. The distorted-wave results for the 2p ionization (which includes no REDA or READI contributions) are about 30% higher than the RMPS_{2p} cross section. Our total RMPS cross section is a sum of the RMPS_{3s} and RMPS_{2p} cross sections and is clearly higher by about 15-20% than the experimental measurements, showing very large REDA features above about 75 eV. This is similar to the findings of Teng [9] who pointed out that without the Auger decay channels for the REDA features in a calculation of the 2p contribution, the resonances would be spuriously high.

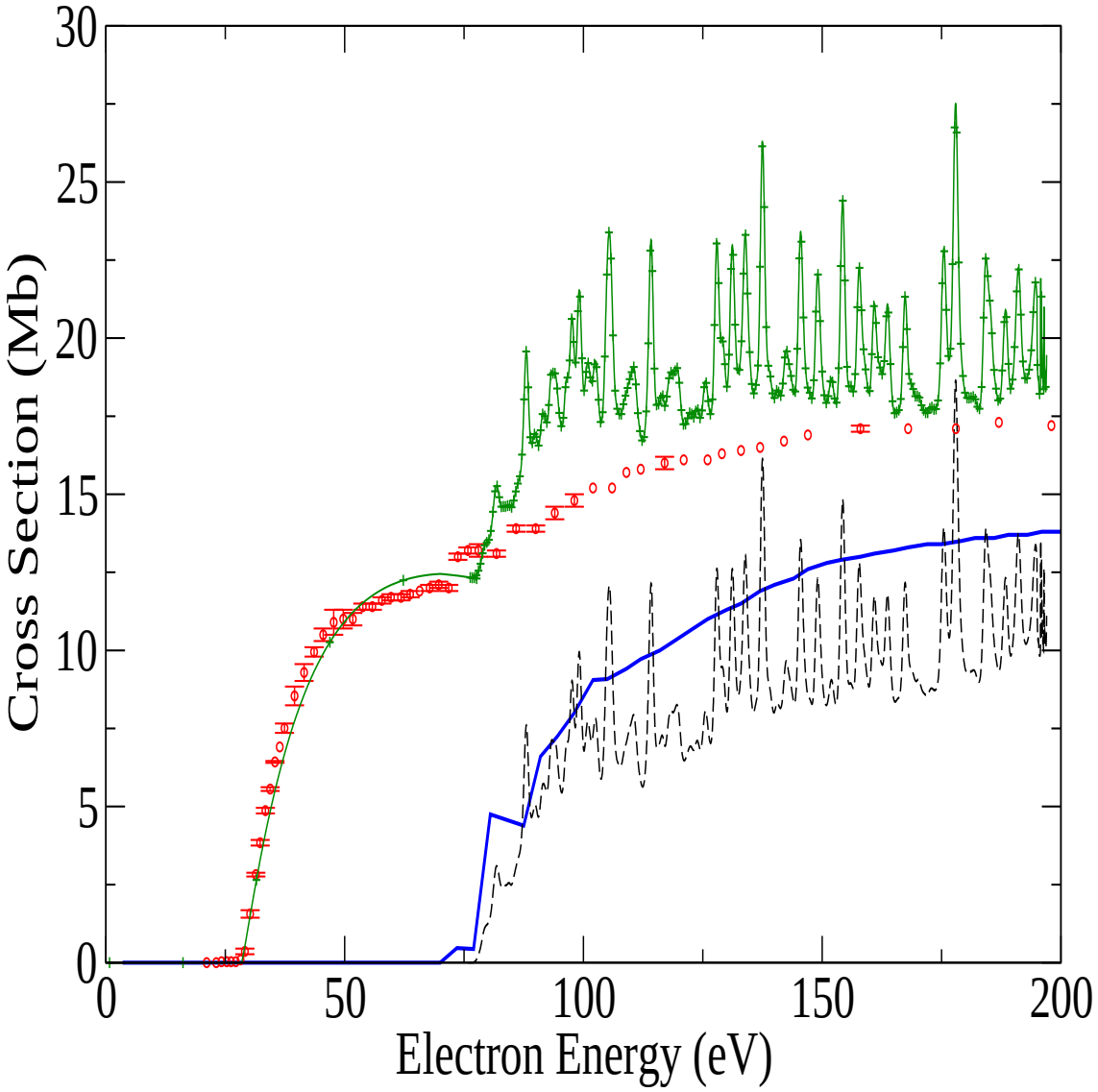

Figure 3.2: Electron impact ionization cross section for Al^{2+}. The dashed curve(black) shows the $RMPS_{2p}$ results. The solid curve(blue) shows the DW results for the 2p ionization only (direct ionization + excitation-autoionization). The circles(red) show the experimental measurements of Thomason and Peart [7]. The stars(green) connected with the solid line shows the $RMPS_{3s}$ + $RMPS_{2p}$ results.

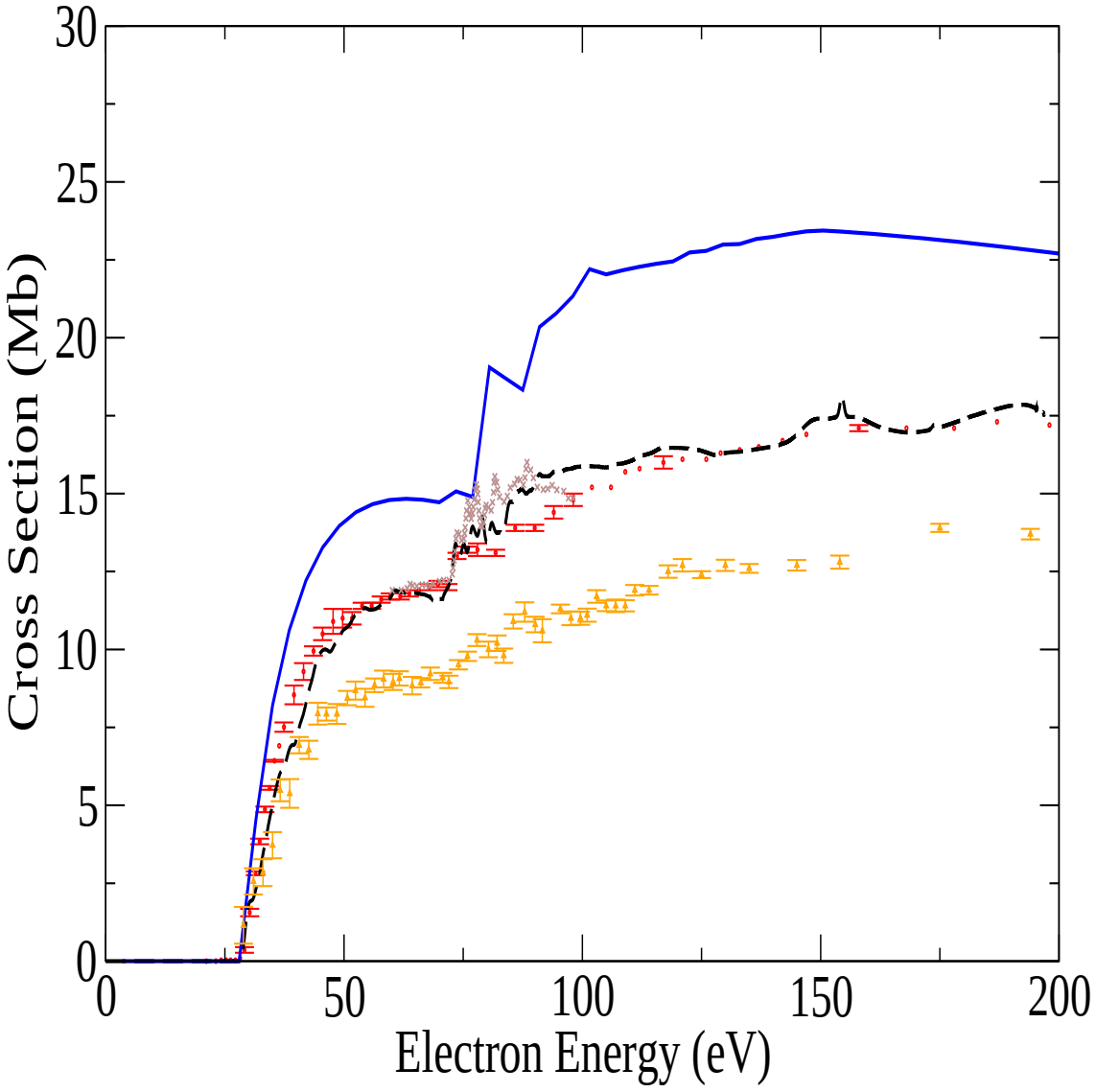

Figure 3.3: Electron impact ionization cross section for Al^{2+}. The dashed curve(black) shows the $RMPS_{3s2p}$. The raw RMPS cross section has been convolved with a 1 eV Gaussian. The solid curve(blue) shows the DW results for the 3s and 2p ionization. The up triangles(yellow) show the experimental measurements of Crandall et al [6], and the circles(red) show the experimental measurements of Thomason and Peart [7]. The R-matrix calculation of Teng [9] is denoted by crosses(tan) and can be seen in more detail in Figure3.4.

Figure 3.3 shows the results from our $RMPS_{3s2p}$ calculation. The heights of the resonance features are much reduced, compared with the $RMPS_{2p}$ results and the background cross section is also reduced in height. The total cross section is now in much better agreement with the experimental measurements of Thomason and Peart [7], and is lower than the RMPS results of Teng [9]. We also note that the contribution due to the 3s near 60 eV is also reduced slightly, and is in better agreement with the experiment. We show our RMPS results convolved with a 1eV Gaussian as previously determined by Teng et al. [9] to best match the experimental resolution. The distorted-wave results are up to 35% higher than the experimental measurements. We note that we have excellent agreement across almost the whole energy range of the experiment, with some small discrepancies remaining from 80-100 eV.

In Figure 3.4 we show results for the region 70 -110 eV, comparing our $RMPS_{3s2p}$ cross section with the experiment of Thomason and Peart [7] and the RMPS results of Teng[9]. In the 70-90 eV region we have much better agreement with the resonance position and heights than the previous results of Teng [9]. Above about 75 eV we are still about 15% higher than the experimental measurements, with the discrepancy being perhaps due to sensitivity in the cross section to the resonance positions of these features. We note that the level of discrepancy that remains is not sufficient to significantly affect the ionization balance results that would be produced using the new data.

3.2 Al^{3+} - Al^{11+}

For the remaining ion stages of Al, non-pertubative methods should provide accurate ionization cross section. For Al^{3+} through to Al^{7+} Aichele et al.[10] have presented cross beam measurements and compared with CADW calculations. Aichele et al. [10] have already calculated CADW cross section for Al^{3+} to Al^{7+}. We perform our calculations here to generate date for the higher charged stages, and rate coefficient for the complete dataset. Aichele et al. [10] found, and we confirmed, that good agreement was found for all of the

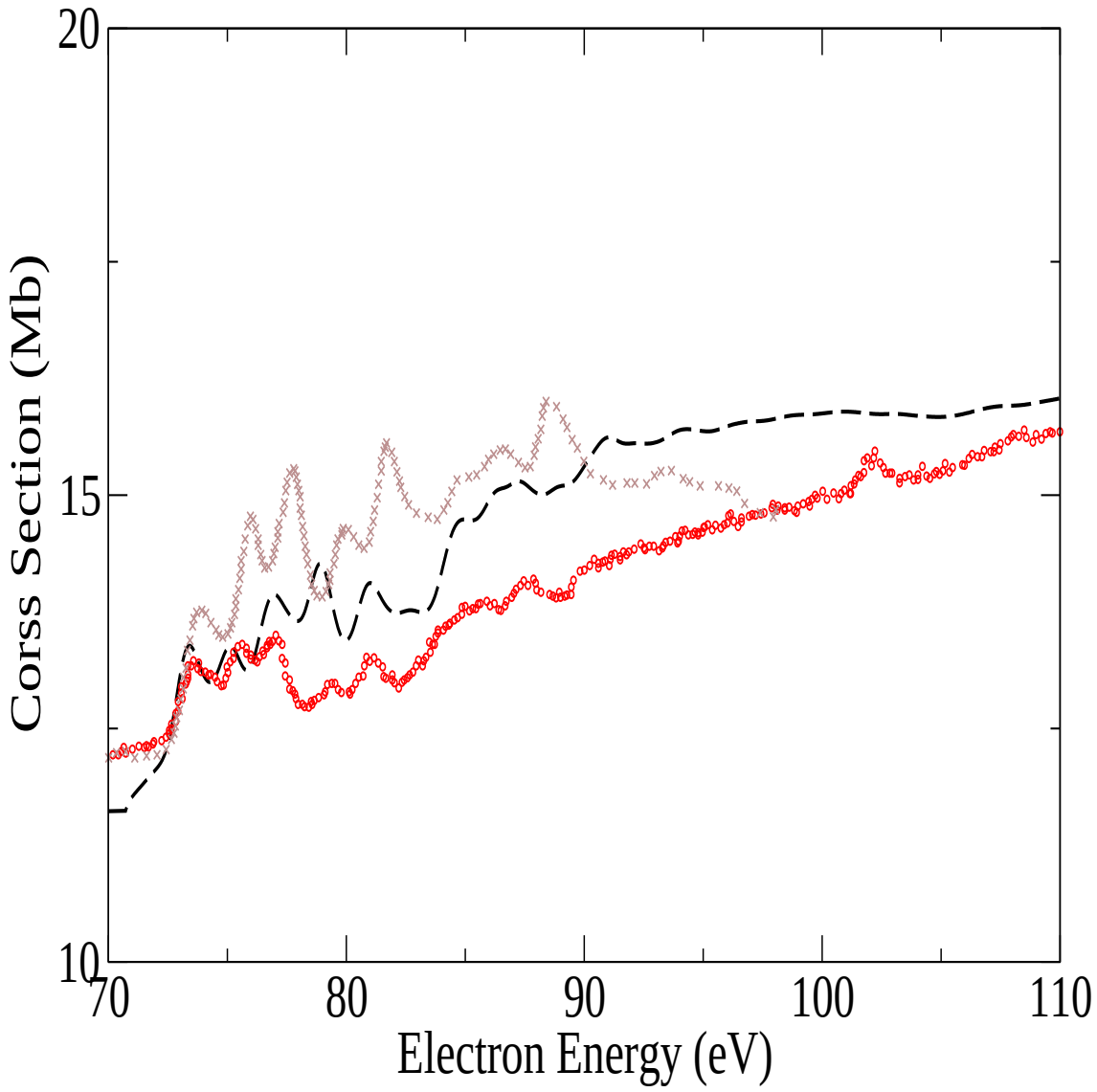

Figure 3.4: Electron impact ionization cross section for Al^{2+}. The dashed curve(black) shows the $RMPS_{3s2p}$ results. The raw RMPS cross section has been convolved with a 1 eV Gaussian. The circles(red) show the fine energy scan experimental measurements of Thomason and Peart [7]. The crosses(tan) show the R-matrix calculation of Teng [9].

ion stages which have no metastable contribution in the ion beam. For the ion stages which were found to have metastable fraction, the experimental results were higher than the ground state CADW ionization cross sections and were consistent with one would expect due to a metastable contribution to the total cross section. To complete our atomic dataset for Al, we have performed our own CADW ionization calculations including both direct ionization and excitation-autoionization. Our results are shown in Figs. 3.5 through to 3.10, with the configuration-average single and double ionization potentials being shown in Appendix A. Our CADW calculations include all process that lie below the double ionization potential for each ion stage.

The theoretical and experimental results for Al^{3+} are shown in Fig 3.5 . Al^{3+} has a ground configuration of $1s^2 2s^2 2p^6$. In the theoretical calculation for the ground configuration, we include direct ionization of the 2p and 2s subshells, and excitation-autoionization from the 2s subshell into the $2s2p^6nl$ configurations, where $3 \leq n \leq 7$ and $0 \leq l \leq 3$. The direct ionization from the 2p and 2s subshells dominates the cross section. In Fig. 3.5, the ionization from 2p and 2s subshells total is about 10% below the experimental result. When we add the excitation autoionization to the total cross section, for energy up to 400 eV, the theoretical result matches the experimental result well. Above 400 eV, total cross section is slightly below experiment. The plane wave Born calculations match the CADW results only at the highest energies.

The theoretical and experimental results for Al^{4+} are shown in Fig 2. Al^{4+} has a ground configuration of $1s^2 2s^2 2p^5$. In the theoretical results for the ground configuration, we include direct ionization of the 2p and 2s subshells, and excitation-autoionization from the 2s subshell into the $2s2p^5nl$ configurations, where $3 \leq n \leq 7$ and $0 \leq l \leq 3$. The dominant ionization of Al^{4+} is from direct ionization of the 2p and 2s subshells. For energy below 400 eV, direct ionization cross section is about 10% below the experimental result. The total cross section which includes excitation autoionization matches the experiment in the low energy part. For

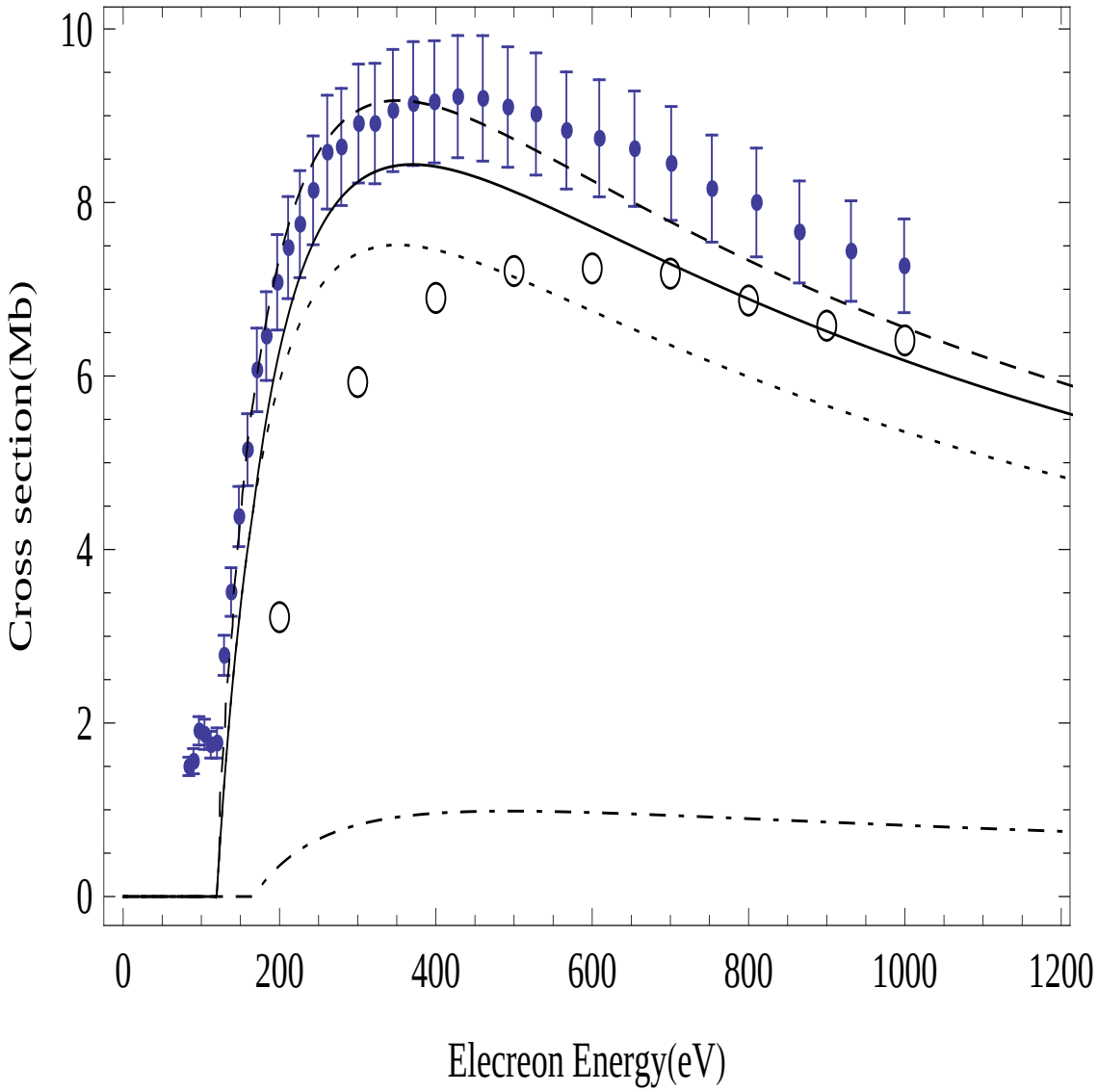

Figure 3.5: Electron impact ionization cross section for Al^{3+}. Error bar represent the total experimental uncertainty [10]. Solid line, CADW calculation, direct ionization;dashed line, CADW calculation, total cross section (direct ionization and excitation);dotted, CADW calculation, 2p subshell only; dot dashed, CADW calculation, 2s subshell only; larger circle, Born-approximation calculation [11]

energy above 400 eV, the total cross section is a little below the experimental result. The plane wave Born calculations match the CADW results only at the highest energies.

The theoretical and experimental results are shown in Fig.3.7 for Al^{5+}. Al^{5+} has a ground configuration of $1s^22s^22p^4$, with terms ^3P, ^1D, ^1S. We calculate the direct ionization from the 2p and 2s subshells, and excitation-autoionization from the 2s subshell into the $2s2p^4nl$ configurations, where $3 \leq n \leq 7$ and $0 \leq l \leq 3$. Direct ionization of the 2p and 2s subshells again dominates the cross section. From Figure 3.7, there is a 10-15% of difference between the experimental results and the total theoretical calculation which includes direct ionization and excitation-autoionization. This may be due to ionization from the excited terms within the $2s^22p^4$ configuration. The experiment does not extend low enough in energy to detect any ionization cross section below the ground state ionization potential.

To check for possible metastable presence in the first excited configuration, we calculated the ionization cross section from the $1s^22s^22p^33s$ configuration. It has terms of ^3S, ^5S, ^1P, ^3P, ^1D, ^3D, of which the ^5S could be metastable. We include the direct ionization from 3s, 2p and 2s sub-shells and excitation-autoionization from the 2p and 2s sub shells to the $1s^22s^22p^2nl$ and $1s^22s2p^3nl$ configurations respectively, where $3 \leq n \leq 7$ and $0 \leq l \leq 3$ for the total cross section for the first excited state of Al^{5+}. This total cross section is about 25% above the experimental result for energy above 1000 eV. Thus, it seems likely that the disagreement between DW theory and experiment is due to metastable terms in the ground and possibly first excited configurations.

Fig.3.8 shows the results for Al^{6+}. The total CADW cross section is about 10% lower than the measurements of Aichele [10] and significantly lower than the the other set of data measured by Aichele [10]. With a ground configuration of $1s^22s^22p^3$ containing ^4S, ^2D and ^2P terms, metastable presence seems likely, explaining with the experimental measurements are higher than the results.

The theoretical and experimental results are shown in Fig. 3.9 for Al^{7+} ground state. Al^{7+} has a ground configuration of $1s^22s^22p^2$, with terms ^3P, ^1S and ^1D. We calculate the

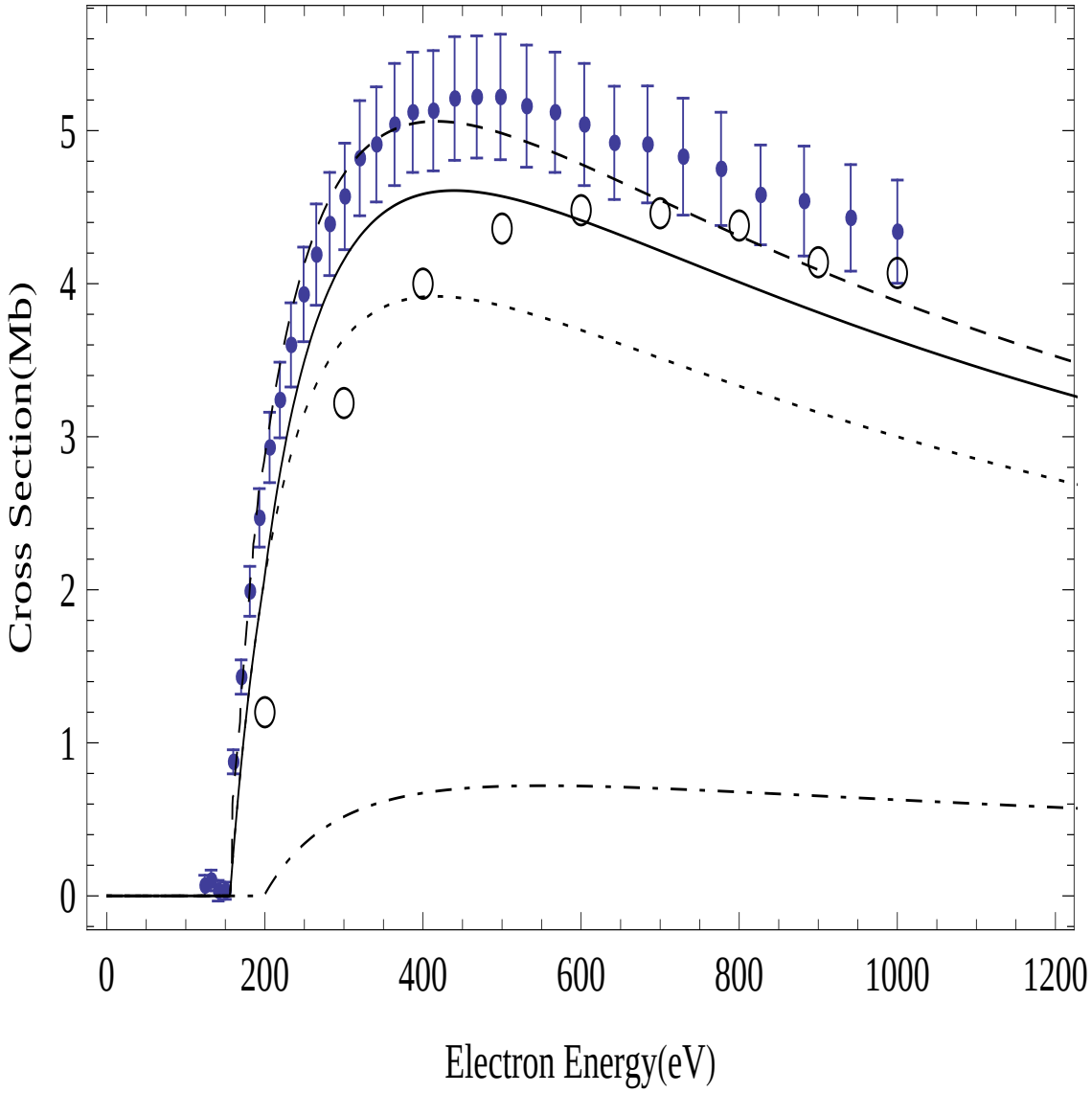

Figure 3.6: Electron impact ionization cross section for Al^{4+}. Error bar represent the total experimental uncertainty [10]. Solid line, CADW calculation, direct ionization;dashed line, CADW calculation, total cros section (direct ionization and excitation);dotted, CADW calculation, 2p subshell only; dot dashed, CADW calculation, 2s subshell only; larger circle, Born-approximation calculation [11]

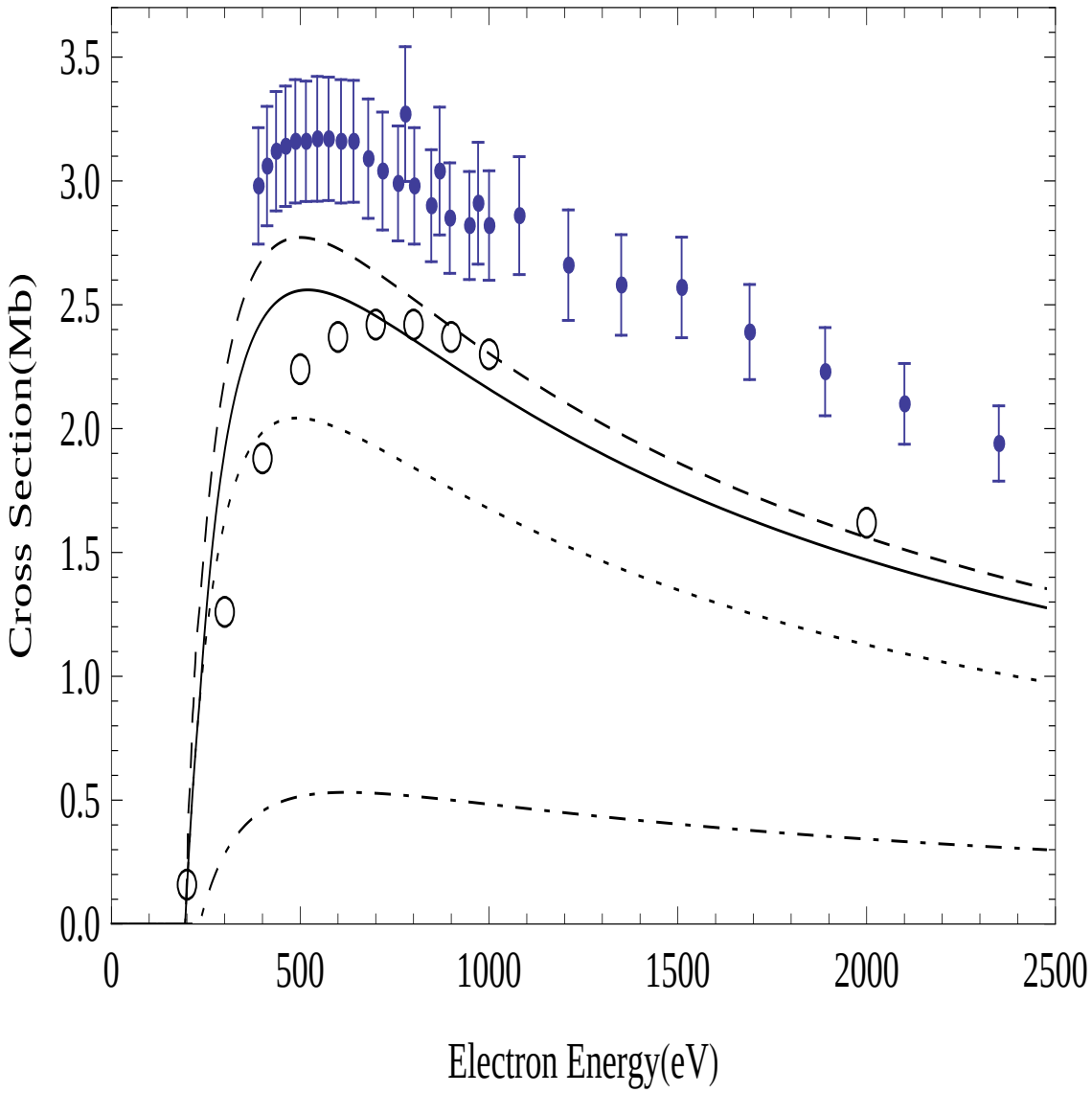

Figure 3.7: Electron impact ionization cross section for Al^{5+}. Error bar represent the total experimental uncertainty [10]. Solid line, CADW calculation, direct ionization;dashed line, CADW calculation, total cross section (direct ionization and excitation);dotted, CADW calculation, 2p subshell only; dot dashed, CADW calculation, 2s subshell only; larger circle, Born-approximation calculation [11]

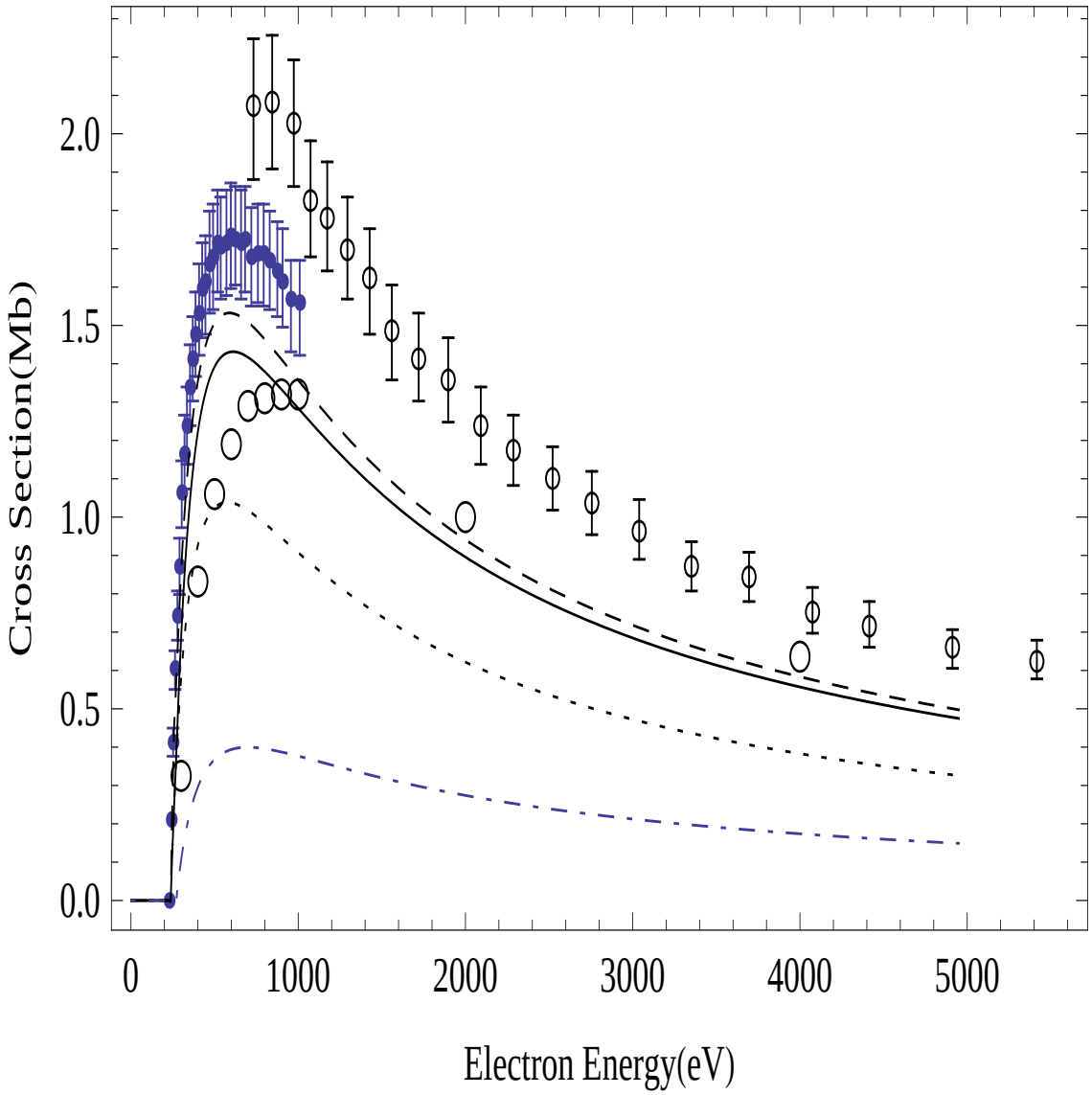

Figure 3.8: Electron impact ionization cross section for Al^{6+}. Error bar represent the total experimental uncertainty [10]. Solid line, CADW calculation, direct ionization;dashed line, CADW calculation, total cross section (direct ionization and excitation);dotted, CADW calculation, 2p subshell only; dot dashed, CADW calculation, 2s subshell only; larger circle, Born-approximation calculation [11]

direct ionization from the 2p and 2s sub-shells. In Fig. 3.9 we can see that experimental result is 25% larger than the theoretical calculation. This again seems most likely to be due to metastable presence in the ground configuration.

For the ion stages above Al^{7+} no experimental measurements exist. There have been two recent compilations of ionization data, in Dere [12] he used experimental data for ion stages up to Al^{7+} and DW calculations using the Flexible Atomic Code (FAC) for the higher ion stages. Mattioli et al .[28] also used experimental measurements for the ion stages up to Al^{7+} and then used the DW data of Bell et al.[81] for the higher ion stages.

Fig 3.10 shows our CADW total ionization cross sections for Al^{8+} to Al^{11+}. For each of these ions direct ionization dominates the total cross section. For Al^{8+} the 2s and 2p ionization dominates, for Al^{9+} and Al^{10+} the 2s ionization dominates, and the 1s is the only ionization channel available for the Al^{11+} ions. Our CADW cross section are in good agreement with the DW data of Dere [12].

In this chapter we have reported on new RMPS results for the single ionization of Al^{2+}. When both the 3s and 2p ionization channels are included in a single calculation, much better agreement is found with the experimental measurements of Thomason and Peart [7]. Distorted-wave calculations for the higher ions were calculated and have been compared with the available experimental measurements. Thus, we expect our new ionization dataset for Al to be a significant improvement over the previously available data. In the next chapter, we investigate the likely implications of the new data using ionization balance modeling results.

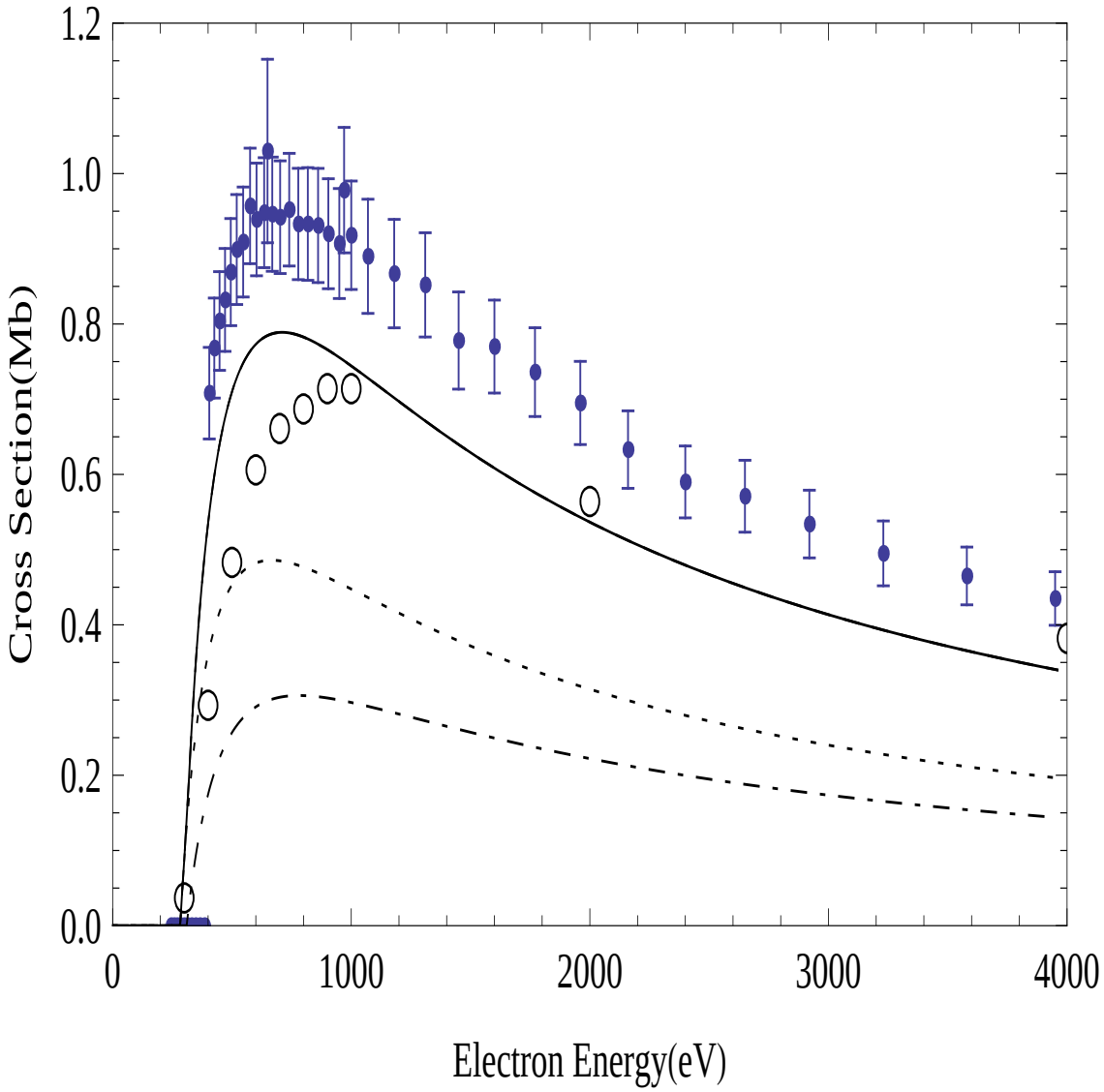

Figure 3.9: Electron impact single ionization cross section for Al^{7+}. Error bar represent the total experimental uncertainty [10]. Solid line, CADW calculation, direct ionization;dotted, CADW calculation, 2p subshell only; dot dashed, CADW calculation, 2s subshell only; larger circle, Born-approximation calculation [11]

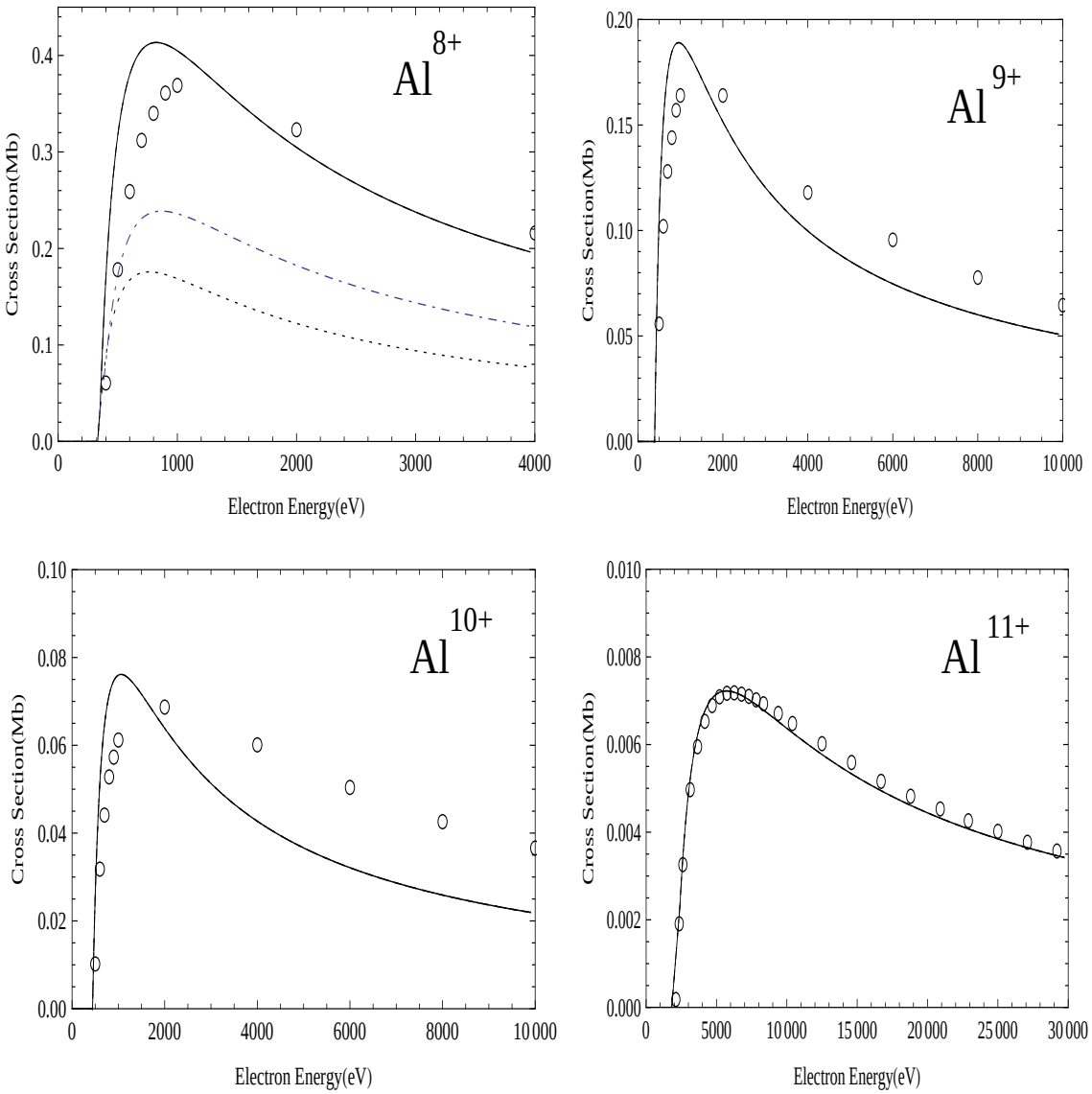

Figure 3.10: Electron impact single ionization cross section for Al^{8+} through to Al^{11+}. Solid line, CADW calculation, direct ionization;dotted, CADW calculation, 2p subshell only; dot dashed, CADW calculation, 2s subshell only; larger circle, Born-approximation calculation [11]

Chapter 4

Data comparison with existing aluminum data and consequences of the new data

While the impact of the new atomic data will be found in future transport modeling studies for the MST device, it is still possible to assess the probable implications of the new data for Al modeling. We will do this through the use of an equilibrium ionization balance study.

The new data can be compared against the existing data in the literature. The data in the ADAS database is based upon their baseline quality calculations and consists of Lotz [82] direct ionization cross sections, this will be referred to as **ADAS89** data. There have been two recent revisions to the available online ionization rate coefficients, namely the compilation of Dere [12] and that of Mattioli et al. [28]. In the compilations of Dere [12] and Mattioli et al. [28], experimentally measured ionization cross sections were used where possible, and largely DW data when no experimental data existed.

4.1 Rate coefficient calculations

For the most meaningful comparison with literature data, Maxwellian rate coefficients should be used as these are the quantities used in the modeling codes. To generate Maxwellian rate coefficients from the non-perturbative R-matrix cross sections shown in the previous two chapters, the cross sections were first fitted with an expression given by Rost and Pattard [83]. These gave good fits for the low energy part of the cross section. Fits using the expression of Younger [78] were then used to fit the higher energy part of the cross sections. These higher energy fits include the Bethe limit point, generated from a distorted-wave photon-ionization calculation, and ensures that the cross sections can be safely extended to the higher energies required for the generation of some of the higher temperature rate coefficients. Figure 4.1

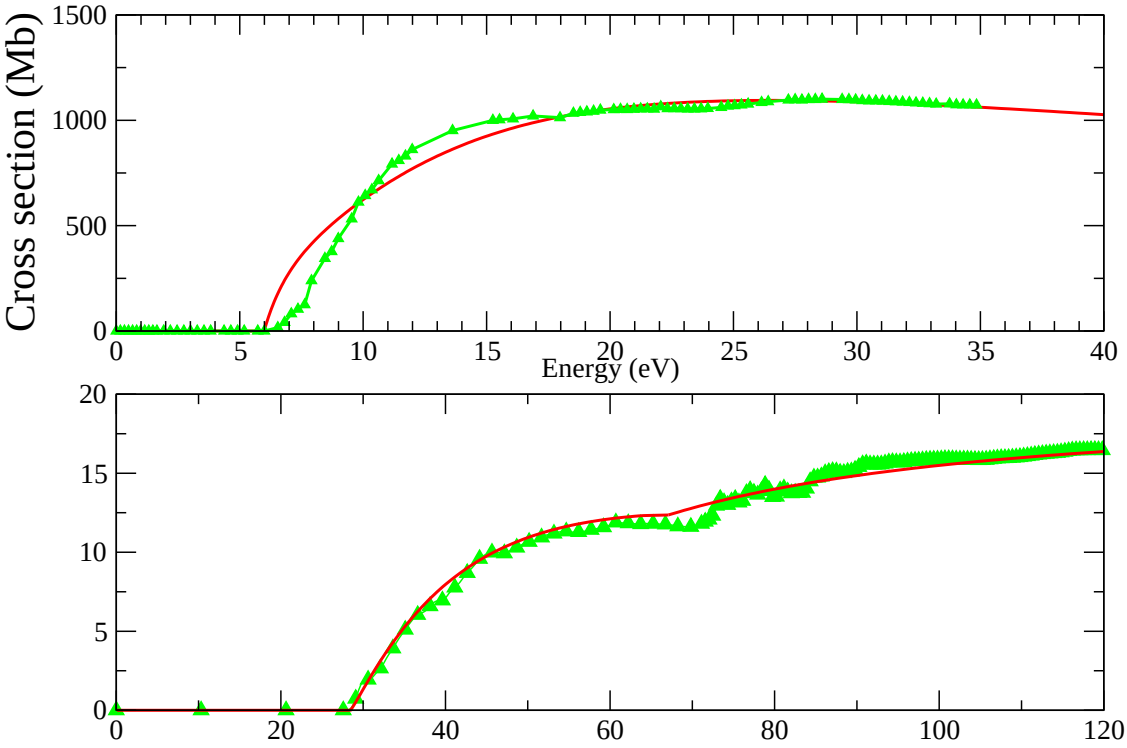

Figure 4.1: Fits to the RMPS cross sections for neutral Al and Al^{2+}. The up triangles (green) show the raw RMPS results and the solid red line shows the fit to the RMPS data.

shows the fits generated for the neutral Al and the Al^{2+} cross sections. A similar method was used by Ludlow et al. [75] to fit their RMPS cross section data for Al^{+}. Note that one of the purposes of the fits to such RMPS cross sections is to smooth out the pseudo-resonance structure seen in the theoretical cross sections.

For the ion stages above Al^{2+} in our new dataset, rate coefficients were made from the distorted-wave cross section shown in Chapter 3. Fits were performed using a Chebychev fit to the near threshold part of the cross section (up to twice the ionization potential), and the Younger expression was used to fit the higher energy part of the cross section. Figures 4.2 through to 4.6 show the comparison for each of the Al ion stages.

Considering the neutral rate coefficient first figure 4.2, the new RMPS data is in good agreement with the data of Dere [12], and lies below the DW data. Since the Dere data is based on a fit to the experimental cross section, which agrees with our RMPS data, one would expect the rate coefficients to be close to each other. The difference between the DW

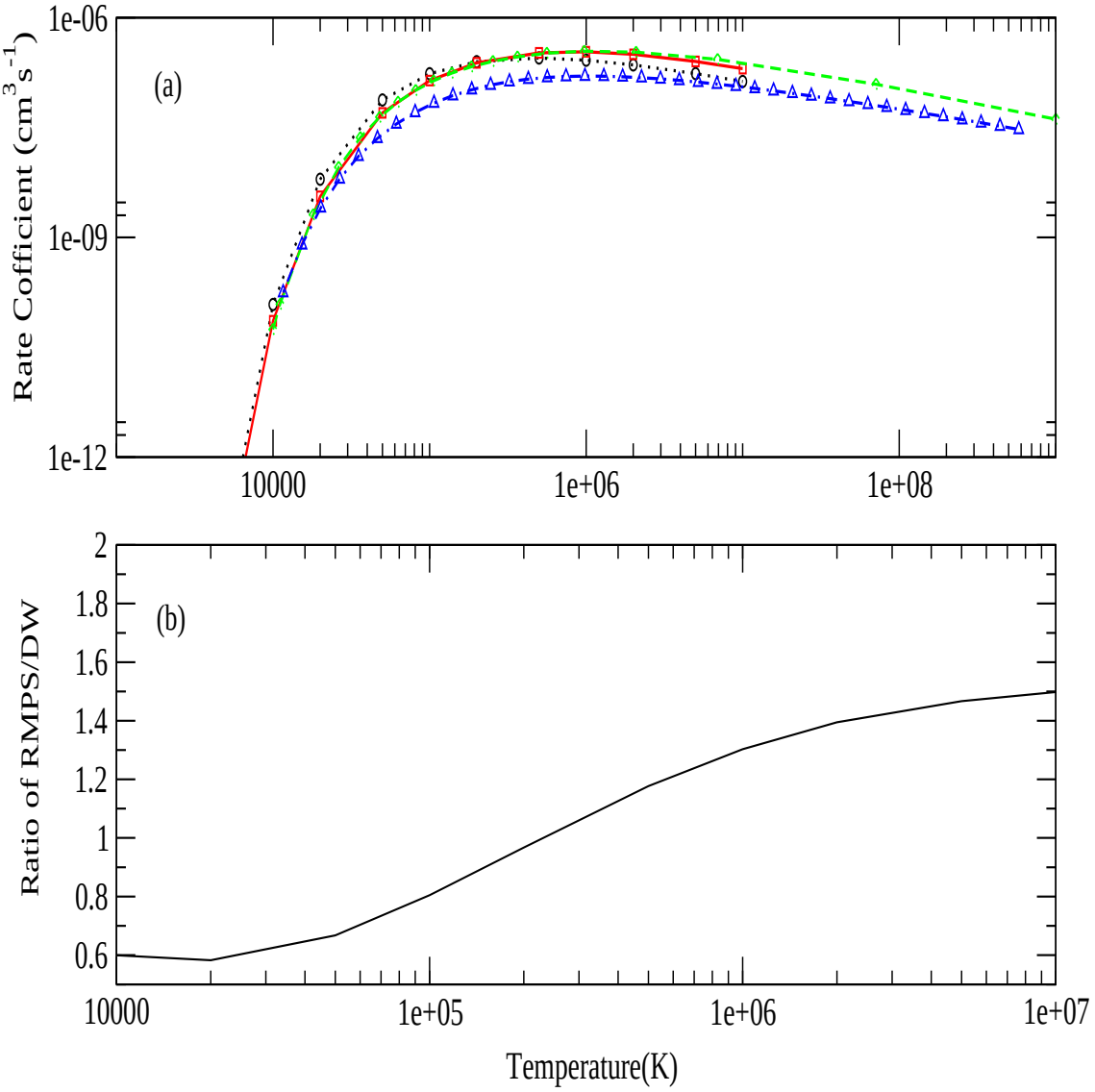

Figure 4.2: Electron-impact ionization rate coefficients for neutral Al. Fig (a) The solid line(red) shows the R-matrix data, the dotted line(black) shows the distorted-wave data, the dashed line(green) shows Dere [12] data and the dashed-dot line shows the ADAS data. Fig (b) shows the ratio of the RMPS rate coefficient to the DW results.

and the RMPS data is due to the DW cross section being spuriously high for the neutral as can be seen in the cross section.

The Al^+ 3s ionization has already been discussed by Ludlow et al. [75] and presents a particularly interesting case. Both the TDCC and RMPS cross section results were below the experimental measurements, while the DW calculations were in good agreement with the measurements. Thus, Ludlow et al. [75] concluded that the measurements were likely to be incorrect and the TDCC/RMPS data should be preferred. One would expect the DW cross sections for a singly ionized system to be too high, so the agreement with experiment is perhaps fortuitous, particularly given the DW results for Al^{2+} are higher than the experiment. Thus, in our recommended dataset, the rate coefficients were generated from the RMPS data discussed in chapter 2. The Dere et al. data on the other hand is based upon the experimental measurements and so agrees with the DW data. Our RMPS rate coefficients are lower than the DW rate coefficients for most of the temperature range, see Fig. 4.3. For Al^+ the RMPS 3s ionization rate coefficients were then supplemented with DW data for the 2p direct ionization and for excitation-autoionization from the 2p subshell. The DW method should improve for the inner shell processes, and these do not significantly affect the total rate coefficient at the temperatures relevant for Al^+.

For Al^{2+} (Fig. 4.4), the RMPS cross section is in good agreement with the Dere et al. data, as one would expect since the Dere et al. data is based upon the experimental measurements. The DW data is slightly above both the RMPS and Dere et al. data, reflecting the fact that the DW cross sections are higher than the RMPS values. For the remainder of the ionization rate coefficients, Al^{3+} through to Al^{12+}, our DW rate coefficients sections are in good agreement with the Dere et al. data, see Figs 4.5 and 4.6. This is consistent with the fact that Dere [12] uses experimental values for ion stages which should consist of pure ground state atoms (and our DW data agrees with these ion stages), and DW data for the ion stages where there are no experimental measurements.

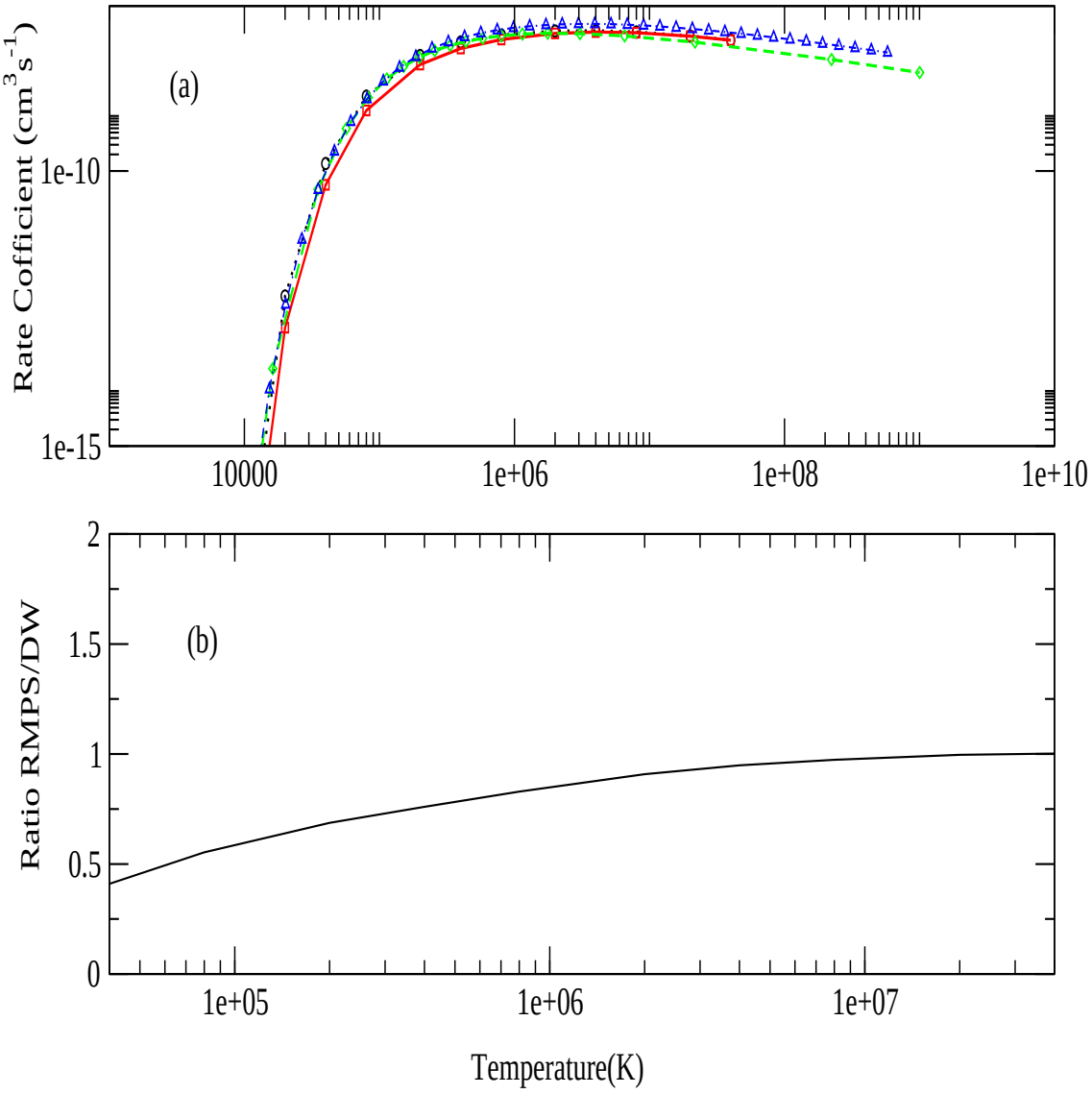

Figure 4.3: Electron-impact ionization rate coefficients for Al^+. Fig (a) The solid line(red) shows the R-matrix data, the dotted line(black) shows the distorted-wave data, the dashed line(green) shows Dere [12] data and the dashed-dot line shows the ADAS data. Fig (b) shows the ratio of the RMPS rate coefficient to the DW results.

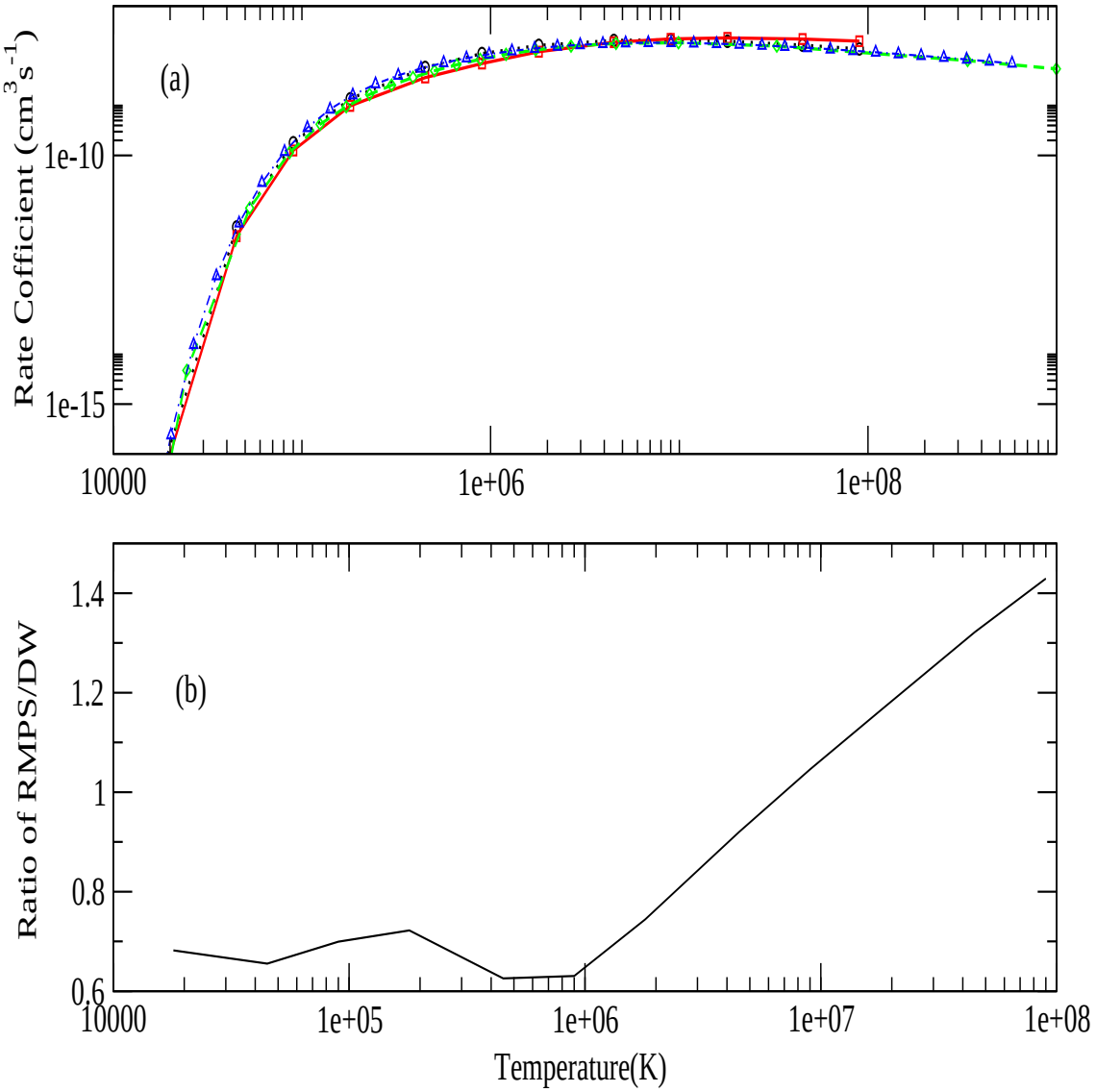

Figure 4.4: Electron-impact ionization rate coefficients for Al^{2+}. Fig (a) The solid line(red) shows the R-matrix data, the dotted line(black) shows the distorted-wave data, the dashed line(green) shows Dere [12] data and the dashed-dot line shows the ADAS data. Fig (b) shows the ratio of the RMPS rate coefficient to the DW results.

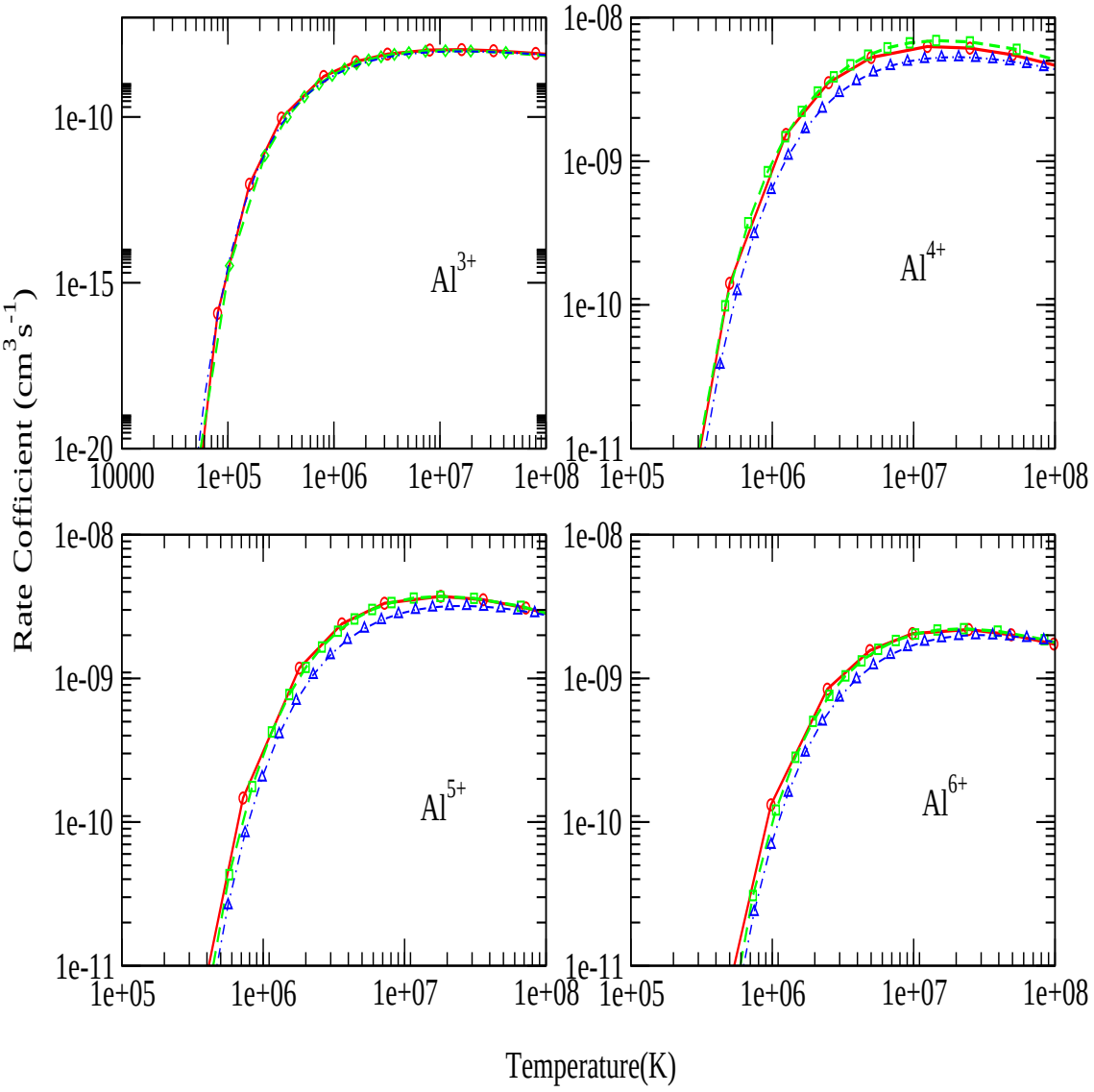

Figure 4.5: Electron-impact ionization rate coefficients for Al^{3+} through to Al^{6+}. Fig (a) The solid line(red) shows the distorted-wave data, the dashed line(green) shows Dere [12] data and the dashed-dot line shows the ADAS data.

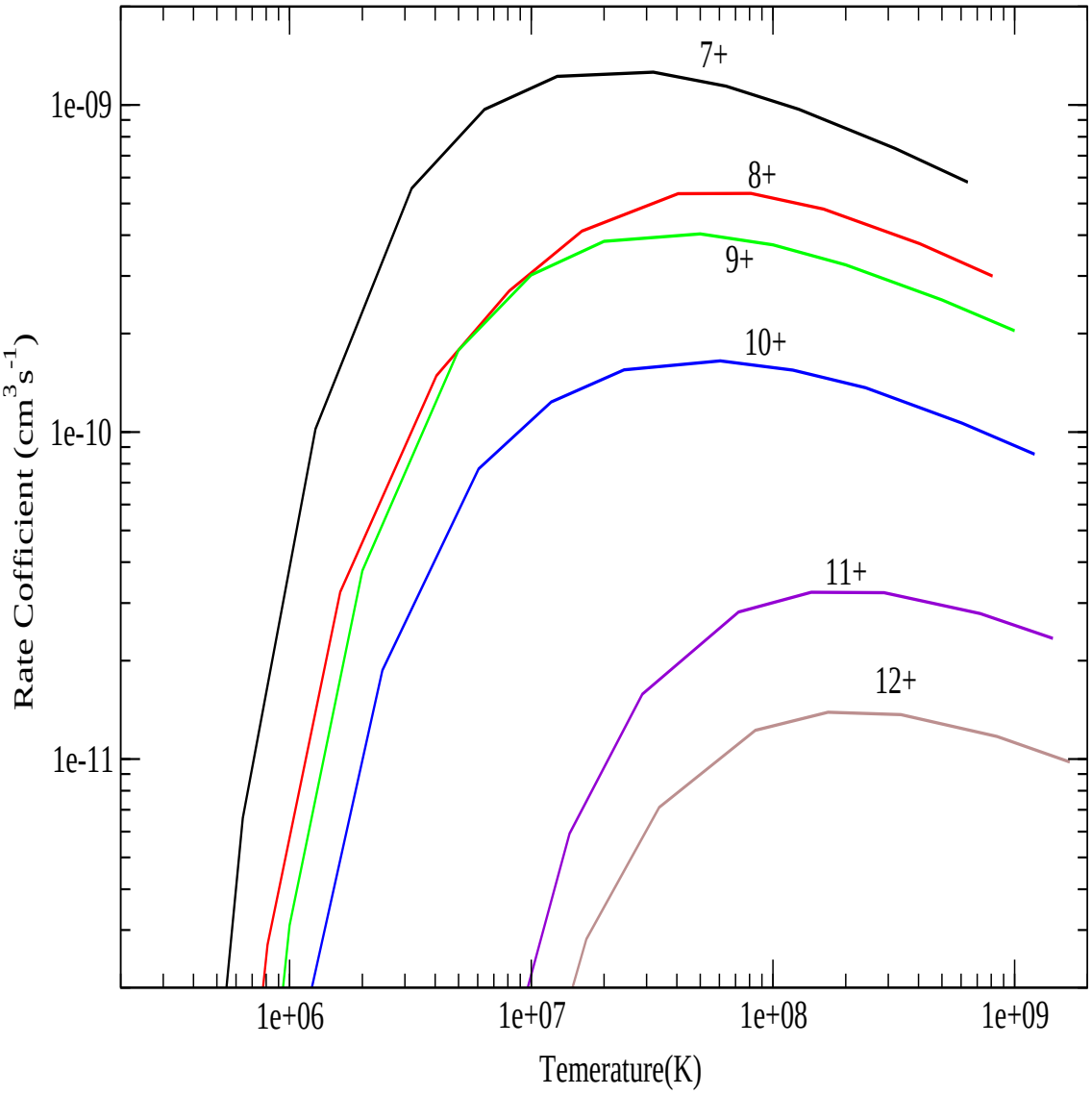

Figure 4.6: Electron-impact ionization rate coefficients for Al^{7+} through to Al^{12+} using DW data.

The Maxwellian rate coefficients will be made available on the CFADC (http://www-cfadc.phy.ornl.gov/data_and_codes/home.html) and the OPEN-ADAS (http://open.adas.ac.uk/) web pages.

4.2 Ionization balance calculations

These rate coefficients were then used to generate an equilibrium ionization balance calculation for all of the ion stages of Al. We compare three datasets, namely the ADAS89, a dataset consisting purely of DW data (called ADASDW), and our new dataset (called ADASRM). In all of the calculations the same recombination rate coefficients were used, namely the DW data in the ADAS database, allowing us to isolate the difference due to just the new ionization rate coefficients. Fig. 4.7 shows the comparison over a temperature range that covers all of the ion stages. As one would expect, the calculations show very little difference for ion stages Al^{4+} and higher, due to the similarity in the underlying rate coefficients. The most interesting differences occur for the first three ion stages, thus Fig.4.8 shows just the low temperature results. The DW results are closer to the R-matrix results than the ADAS89 data. Since all of our ionization rate coefficients for the low charge states are lower than the existing ADAS data, one can see from the figures that the low charge states of Al are predicted to exist up to higher temperatures than previously thought. Also, since the rate coefficients are smaller than those previously used, one would also expect that it would take the Al ions longer to reach ionization equilibrium than previously thought.

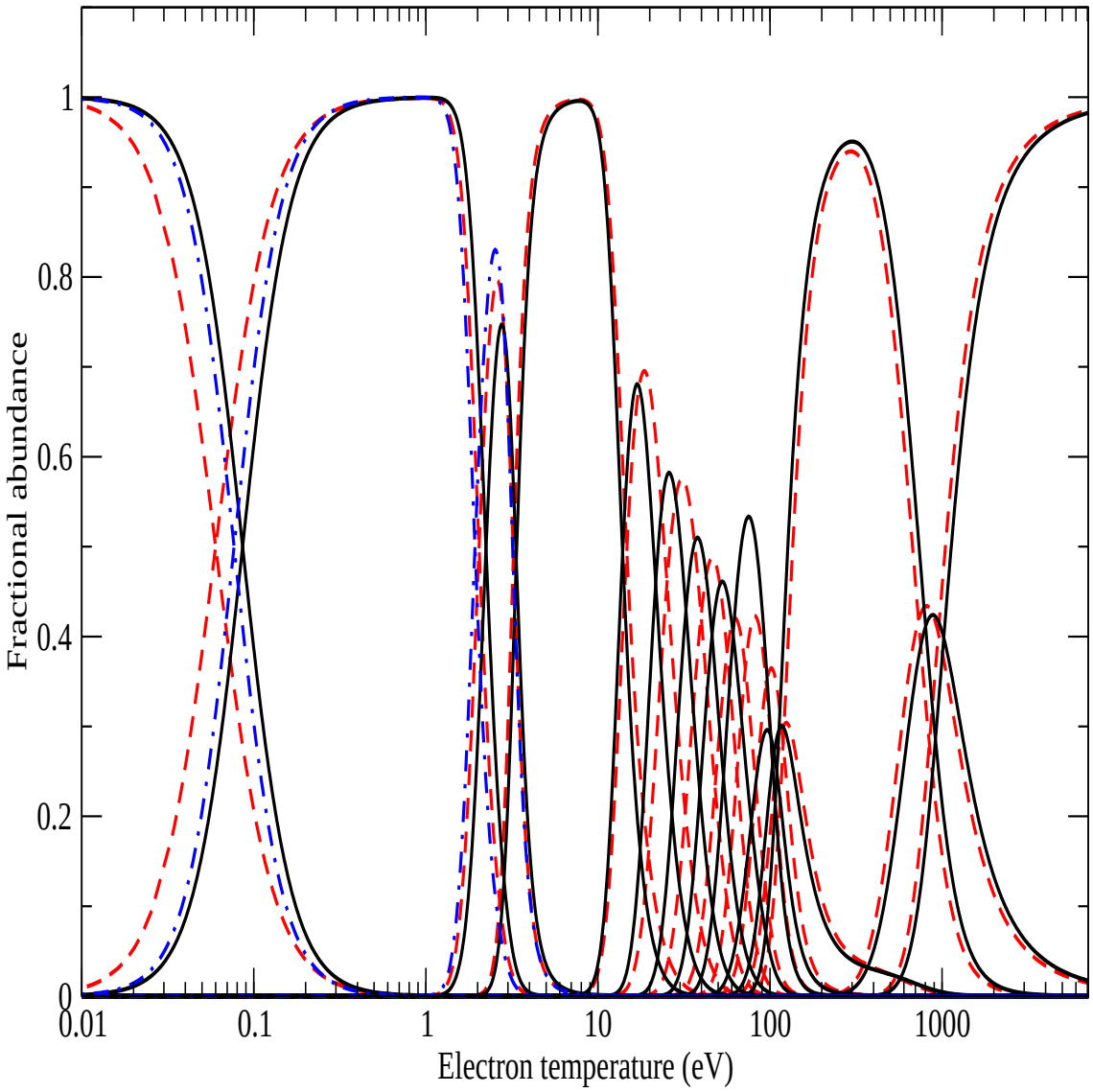

Figure 4.7: Electron-impact equilibrium ionization balance results showing the results using the R-matrix dataset (solid line), the DW dataset(dot-dashed line) and the ADAS dataset(dashed line).

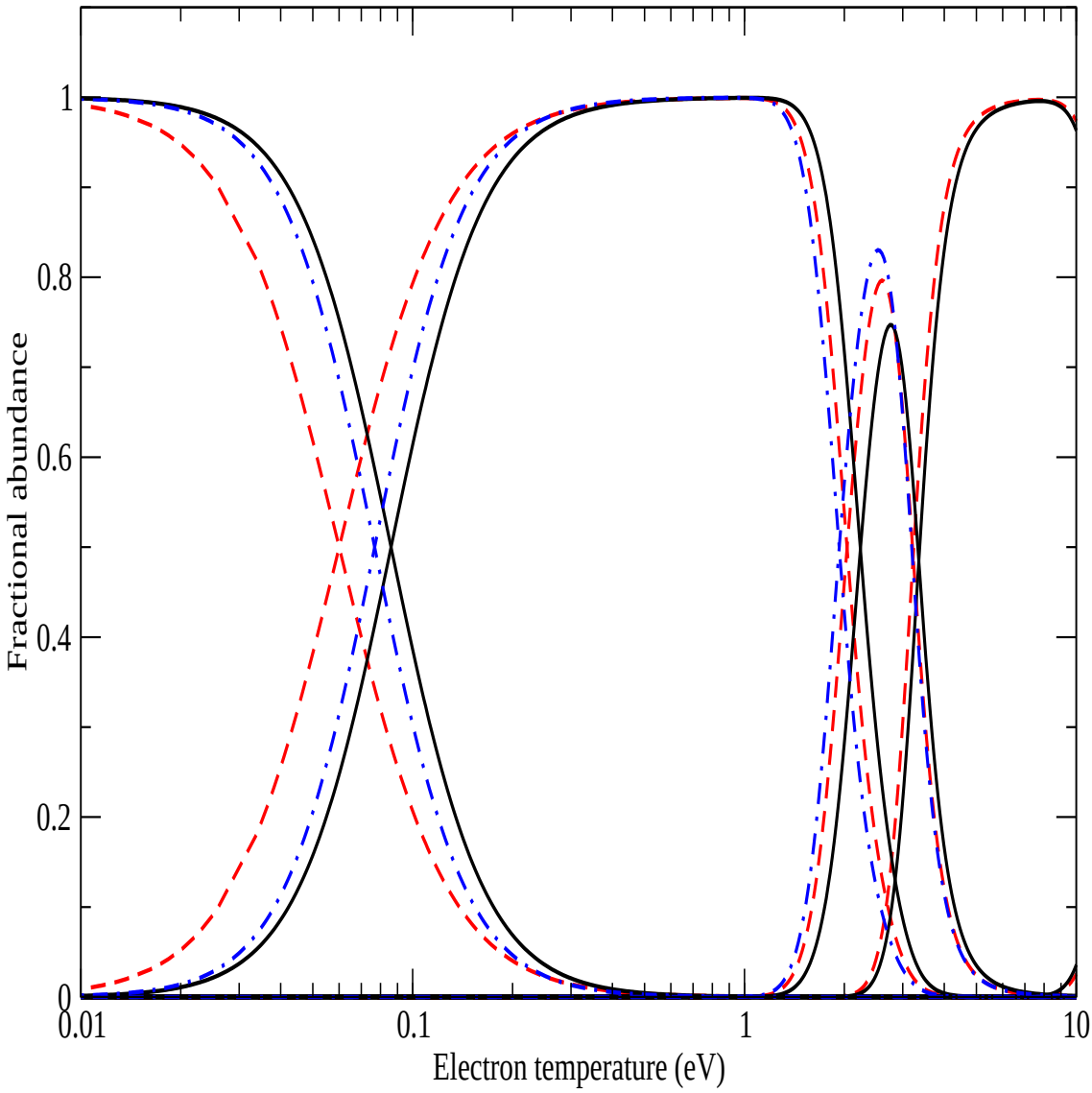

Figure 4.8: Electron-impact equilibrium ionization balance results showing the results using the R-matrix dataset (solid line), the DW dataset(dot-dashed line) and the ADAS dataset(dashed line). Results are shown for just the first 4 ion stages.

Chapter 5

Ne-like iron-peak elements

5.1 Introduction

The improved sensitivity and spectral resolution of X-ray observations have led to the recent detection of the less abundant Fe peak elements, starting with the identification of Kα emission from He-like Mn and Cr in ASCA spectra of the W49B supernova remnant [44], later confirmed with XMM by Miceli [45]. A number of more recent observations have also revealed emission from the Ne-like stages of these ions. In the Suzaku spectra of Tycho's SNR, Tamagawa et al. [1] identified not only the Fe Kα blend, but also presented the first tentative identifications of Kα emission from Ne-like Cr and Mn (energies 5.48 and 5.95 keV, respectively). They also report Ca and Fe Kβ features at 4.56 and 7.11 keV, respectively. Yamaguchi et al. [84] used Suzaku observations to identify K shell emission from Mn and Cr in Tycho, Kepler, and N103B. Chandra detections of Cr have been reported by Yang [42]. Cr and Mn have also been identified in the Galactic Center [85] and the Perseus Cluster [86] using Suzaku.

The Fe peak elements, which are very sensitive to the details of the supernova event, are important diagnostics of the explosion and even of the progenitor. Badenes [41] demonstrated that the relative Mn/Cr abundances depends upon the progenitor metallicity. The usefulness of the growing sample of existing observations, however, is sharply limited by the lack of K-shell electron-impact excitation data for Mn, Cr, Co, and Ni. Without photon emissivities derived from such calculations, element abundances cannot be estimated accurately, and that problem is complicated further by the inability to address issues such as line blending. The current generation of X-ray spectrometers have adequate sensitivity to detect these weak lines, though only have moderate spectral resolution (ΔE $\sim$100 eV).

The Ne-like ions of the Fe group are likely to be particularly abundant in supernova remnants and yet there are no relevant K-shell data in the atomic database. Previous collision calculations for Fe-peak elements have focused largely on iron, and for the Ne-like ions most work has concentrated on the L-shell transitions. Very few calculations for the K shell are in existence.

Previous L shell calculations for Fe have used a variety of methods. Chen [87] reported theoretical results from semi-relativistic R-matrix calculations for Ne-like Fe. Chen [15] calculated Dirac R-matrix effective collision strengths, and compared modeled line ratios with EBIT and astrophysical measurements. Loch et al. [13] reported on fully relativistic R-matrix calculations for Fe^{16+}. A number of comparisons of the available theoretical data with EBIT measurements at the Lawrence Livermore National Laboratory (LLNL) electron beam ion trap (EBIT) [88] and the NIST EBIT [89] have been performed. They find broad agreement at the lower energies, but discrepancies remain with some of the theoretical results for the 3C/3D ratio at the highest energies measured. The measurements are in good agreement with the calculations of Chen [15], with the results of Loch [13] being higher than the measured ratio.

For elements other that Fe, there have been recent iso-electronic sequence calculations for L-shell excitation of Na^+ through to Kr^{26+} using the intermediate coupling frame transformation (ICFT) R-matrix approach [14]. It is also noted that Ne-like Ni [90, 91] and Ne-like Kr [92] have also been calculated previously. However, there are not at present any non-perturbative calculations of K-shell excitation for Ne-like Cr, Mn, Fe, Co, or Ni. Thus, there is a lack of such atomic data in current astrophysical databases. Due to the likely abundance of the Ne-like ion stages in young supernova remnant plasmas, there is a pressing need for such data. In this chapter we perform R-matrix calculations for each of these ions, generating electron-impact excitation rates as well as radiative transition rates.

5.2 Spectral modeling theory

As part of this work, a set of photon emissivity coefficients (PECs) are generated from a collisional-radiative model. We use collisional-radiative theory [51] as implemented in the ADAS suite of codes ([27],http://www.adas.ac.uk) to produce photon emissivity coefficients for each element in our study. The photon emissivity coefficients for a given transition $j \rightarrow k$, which include collisional and radiative redistribution between the excited states (i and j) are given by

$$PEC^{exc}_{j\rightarrow k} = A_{j\rightarrow k} \sum_i C^{-1}_{ji} C_{i1} \quad (5.1)$$

$$PEC^{rec}_{j\rightarrow k} = A_{j\rightarrow k} \sum_i C^{-1}_{ji} R_{i+} \quad (5.2)$$

where $A_{j\rightarrow k}$ is the spontaneous emission coefficient for the transition $j \rightarrow k$ and the C-matrix elements contain the collisional and radiative rates connecting the excited levels of the atom. C_{i1} is the excitation rate coefficient from the ground of the Ne-like ion to level i and R_{i+} is the recombination rate coefficient from the ground of the recombining ion into level i of the Ne-like stage.

Thus, the absolute line intensity in a given spectral line would be the PEC^{exc} coefficient multiplied by the ground population and the electron density, plus the PEC^{rec} times the ground population of the recombining ion and the electron density. For most plasma applications the PEC^{exc} dominates the line emission so the line intensities in Section 3.2 will be analyzed using PEC^{exc} values. We archive PEC coefficients for the strongest transitions for each ion on a temperature-density grid. These can then be used for direct comparison with spectral observations. If the line intensities of two different Ne-like ions are measured one can calculate the abundance ratio if the PEC ratio is known. Consider the ratio of the observed $K\alpha$ fluxes in Ne-like Fe and Mn from a homogeneous plasma.

$$\frac{I_{K\alpha}^{Mn}}{I_{K\alpha}^{Fe}} = \frac{N_{tot}^{Mn}(\frac{N^{Mn^{15+}}}{N_{tot}^{Mn}})(\frac{N_{excited}^{Mn^{15+}}}{N^{Mn^{15+}}})A_{K\alpha}^{Mn^{15+}}}{N_{tot}^{Fe}(\frac{N^{Fe^{16+}}}{N_{tot}^{Fe}})(\frac{N_{excited}^{Fe^{16+}}}{N^{Fe^{16+}}})A_{K\alpha}^{Fe^{16+}}} \tag{5.3}$$

where N_{tot}^{Fe} and N_{tot}^{Mn} are the absolute densities of Fe and Mn in the plasma, and the subsequent terms in brackets are the fractional abundance of the Ne-like ion stage and the relative population of the excited state within the Ne-like stage. If we assume that both ions have the same fraction in the Ne-like stage, then we have

$$\frac{I_{K\alpha}^{Mn}}{I_{K\alpha}^{Fe}} = \frac{N_{tot}^{Mn}}{N_{tot}^{Fe}} \frac{\frac{N_{excited}^{Mn^{15+}}}{N^{Mn^{15+}}} A_{K\alpha}^{Mn^{15+}}}{\frac{N_{excited}^{Fe^{16+}}}{N^{Fe^{16+}}} A_{K\alpha}^{Fe^{16+}}} \tag{5.4}$$

where the fraction on the right hand side is simply the ratio of the PEC^{exc} values for the transitions. For the case of the Kα emission features, these would be the sum over all of the level-resolved Kα transitions. Thus, we can determine an abundance ratio from a measured line ratio.

Later in this chapter we illustrate the use of these PECs by analyzing Mn, Cr, Fe and Ni fluxes reported by Tamagawa [1] to determine abundance ratios of Mn, Cr and Ni to Fe. The PECs are archived in the OPEN-ADAS (http://open-adas.ac.uk), the CFADC (http://www-cfadc.phy.ornl.gov) and the xspec(http://heasarc.gsfc.nasa.gov/xanadu/xspec)web pages, so that they can be used by the modeling community.

5.3 Collisional Results

We have used AUTOSTRUCTURE [93] to generate the radial orbitals for each of the ion stages. Our atomic structure calculations employed the same orbital scaling parameters as used by Liang [14], showed in table 5.3. All 27 terms (47 JΠ levels) arising from the following configurations $2p^6$, $2p^5nl$, $2s2p^6nl$ and $1s2s^22p^6nl$ ($n = 3$ and $l = s, p, d$) were also used in the close-coupling expansion of the subsequent scattering calculation. AUTOSTRUCTURE was

Table 5.1: scaling parameters for Ne-like iron-peak elements

orbital	scaling parameter
1s	1.0
2s	1.27826
2p	1.06471
3s	1.23503
3p	1.08299
3d	1.05443

also used to calculate the infinite-energy Bethe/Born limit points to allow us to interpolate our collision strengths to higher energies.

Significantly modified versions of the serial RMATRX I programs ([62], [61] and [60]), have been used to perform the electron-impact excitation R-matrix calculation for each of the five ion stages. In the ICFT approach, the majority of the scattering calculation is carried out within an LS coupling framework, including the one electron mass-velocity and Darwin terms. This greatly reduces the amount of angular algebra to be calculated, the size of Hamiltonian matrices to be diagonalised, and the overall number of close-coupled scattering channels. It is only at the final stage of the calculation that term-resolved K-matrices are transformed into level-to-level K-matrices from which level-resolved cross sections can be extracted. A fine energy mesh is simply achieved by the distribution of the energy mesh over a large number of processors, and this degree of energy resolution facilitates the faster convergence of Maxwell averaged collision strengths.

In order to span the electron-impact energy range that involves X-ray transitions, we calculated the electron-continuum basis from 0 to 2200 Ryds (approximately 4 times the K shell edge) for each of the ion stages. Fifty-six partial waves ranging in angular momentum from L=0-13 were calculated that allowed for exchange between the incident and target electrons. Another 152 higher partial waves, from L=14-48, were also explicitly calculated but now ignoring exchange. All results were 'topped-up' to include higher L contributions to the cross section using the method described by Burgess [72] for dipole transitions and a geometric series for non-dipole transitions.

We investigated the effects of radiation damping [94] on the resonant contributions to our cross sections, and although there exists forbidden transitions for which the effect is noticeable, for the strong dipole allowed excitations the effects were minimal. However, we shall illustrate this in greater detail within the results sections. Preliminary investigations into the effects of Auger damping revealed negligible effects on the cross section for this neon-like sequence.

In Table 5.2, we compare our AUTOSTRUCTURE target energies with available NIST energies, though we note that there are no level-resolved target energies for the K-shell hole states of Fe^{16+}. In general, there is good agreement with NIST energies. Comparisons with the energy levels of NIST, for the 29 levels available reveal an average difference of only 0.16%. Figure 5.3 shows a energy level diagram for Fe^{16+} and Fe^{15+}.

In the asymptotic region, we performed several calculations on one ion stage, to verify the energy mesh required to converge the effective collision strengths. Using Fe^{16+} as our benchmark, we progressively doubled the energy mesh until there were minimal differences in the Maxwellian averaged collisions strengths between models. Between 200,000 and 400,000 points in the resonance region, only 79% of the transitions from the ground state had converged to 5%, however by 800,000 points this had converged to better than 5%. This energy mesh was used for each of the Fe-peak elements we calculated.

We also compared our R-matrix results with previous work [13, 15] on Ne-like Fe^{16+} excitation. Loch [13] used Dirac-Fock atomic structure program GRASP with 139 levels which have the configurations $2p^6$, $2p^5nl$ with n=3-5 and $2s2p^6nl$ with n=3-4. Chen [15] used $2s2p^63l$ with l=s,p,d and $2s^22p^54l$ with l=s,p,d,f. The calculations of Liang [14] included 113 LS terms originating from configurations $2s^22p^6$, $2s^22p^5nl$, $2s2p^6nl$ (n=3-5 and l= s,p,d,f and g), and $2s^22p^56l', 7l'$ (l' = s,p and d). We cannot compare our K-shell results with previous calculations, however we can compare with the L-shell transitions from the papers mentioned above. Figure 5.3 shows the results for the $1s^22s^22p^6$ ($^1S_0$) $\rightarrow 1s^22s^22p^53d$ ($^3D_1$) and $1s^22s^22p^6$ ($^1S_0$) $\rightarrow$ $1s^22s^22p^53d$ ($^1P_1$) transitions. Also shown on Figure 5.3 are the effective collision

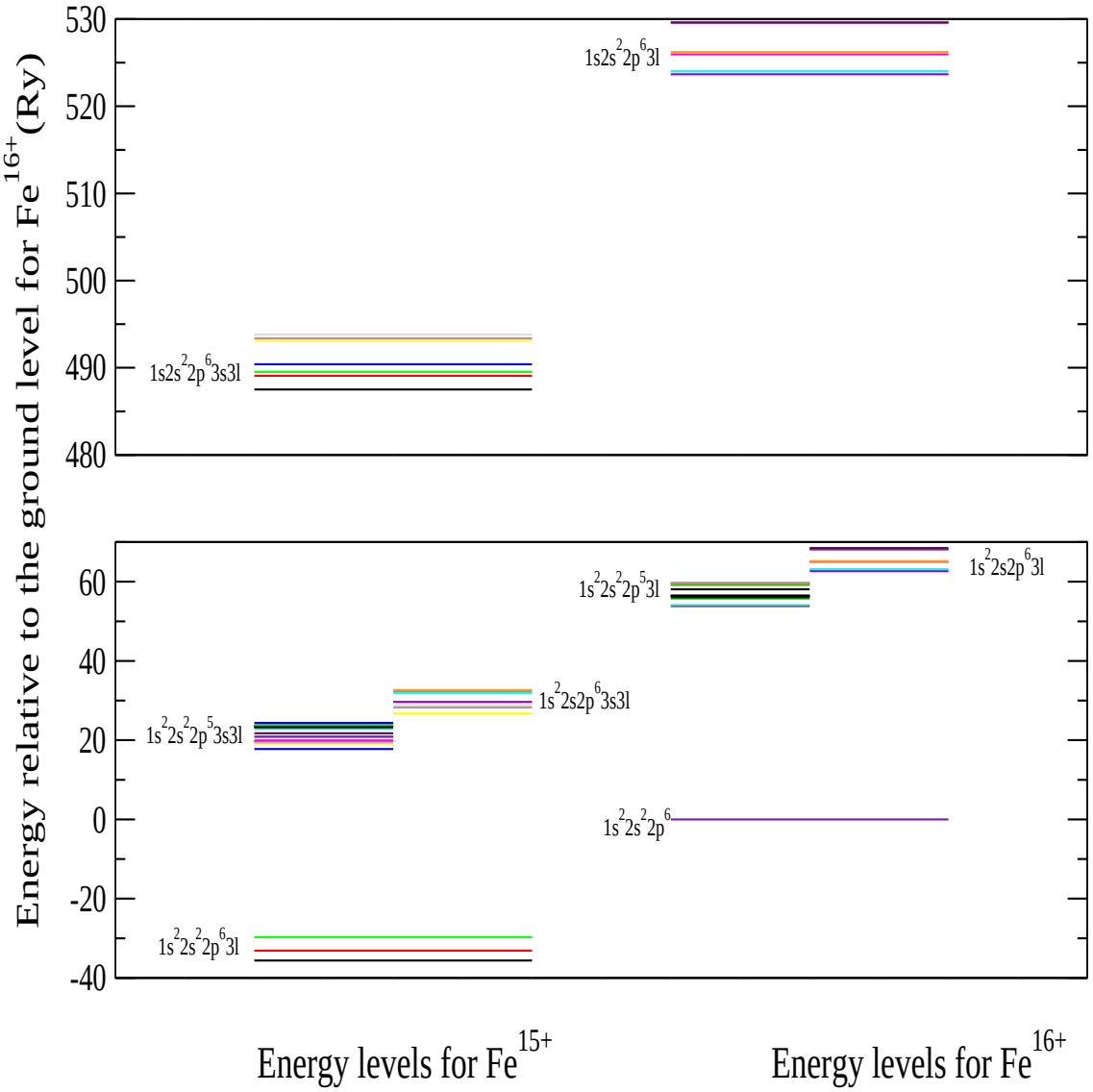

Figure 5.1: Energy levels for Fe^{15+} and Fe^{16+} relative to the ground state of Fe^{16+}.

Table 5.2: Sample of the level energies from AUTOSTRUCTURE and corresponding NIST energies.

Configuration	Term	Level	NIST result (Ry)	AUTOSTRUCTURE value (Ry)	Difference (%)
$1s^2 2s^2 2p^6$	^1S	0	0.00000	0.0000	0.00
$1s^2 2s^2 2p^5 3s$	^3P	2	53.30447	53.315455	0.0206
	^1P	1	53.44371	53.460198	0.0309
	^3P	0	54.23142	54.330453	0.1826
	^3P	1	54.31944	54.422717	0.1901
$1s^2 2s^2 2p^5 3p$	^3S	1	55.52760	55.535145	0.0136
$1s^2 2s^2 2p^5 3p$	^3D	2	55.78494	55.796155	0.0201
	^3D	3	55.90377	55.932013	0.0505
	^3D	1	56.67197	56.773272	0.1788
$1s^2 2s^2 2p^5 3p$	^1P	1	55.98688	56.012094	0.0450
$1s^2 2s^2 2p^5 3p$	^3P	2	56.12011	56.150614	0.0544
	^3P	0	56.51906	56.604307	0.1508
	^3P	1	56.91054	57.024039	0.1994
$1s^2 2s^2 2p^5 3p$	^1D	2	56.93833	57.060799	0.2151
$1s^2 2s^2 2p^5 3p$	^1S	0	57.89653	58.193330	0.5126
$1s^2 2s^2 2p^5 3d$	^3P	0	58.90412	58.932336	0.0479
	^3P	2	58.90412	59.013155	0.1851
	^3P	3	58.90412	59.163010	0.4395
	^3F	4	59.11234	59.177600	0.1104
	^3F	3	59.16884	59.216109	0.0799
	^3F	2	60.09223	60.222887	0.2174
$1s^2 2s^2 2p^5 3d$	^3D	3	59.37224	59.440231	0.1145
	^3D	1	59.7080	59.801105	0.1559
	^3D	2	60.15228	60.296689	0.2401
$1s^2 2s^2 2p^5 3d$	^1F	3	60.19056	60.346535	0.2591
$1s^2 2s^2 2p^5 3d$	^1P	1	60.69	60.905269	0.3547
$1s^2 2s 2p^6 3s$	^1S	0	63.88	63.854206	0.0404
$1s^2 2s 2p^6 3p$	^3P	1	65.6012	65.744405	0.2183
$1s^2 2s 2p^6 3p$	^1P	1	65.9238	66.114857	0.2898

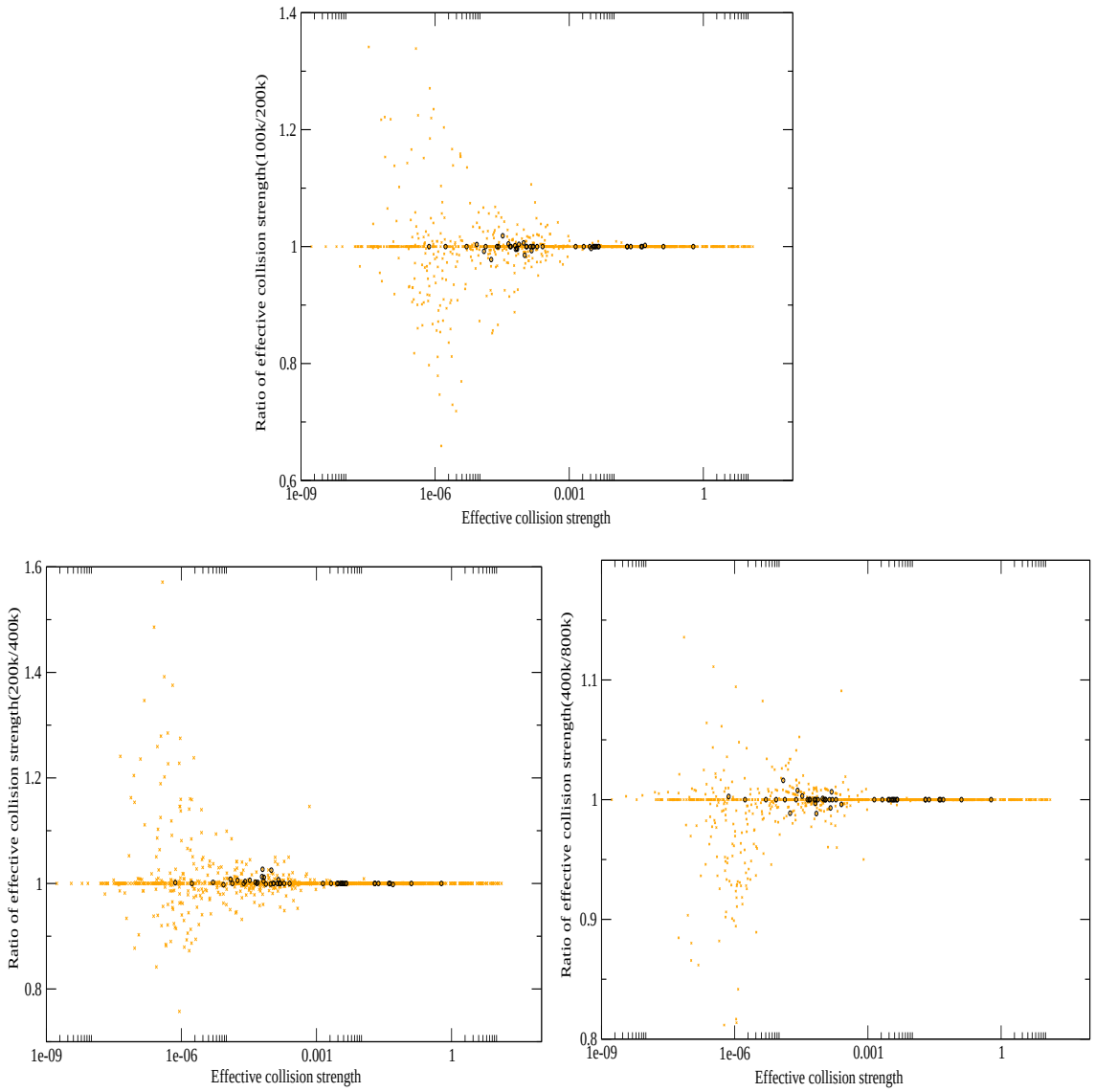

Figure 5.2: Ratio of effective collision strength for different energy mesh vs. effective collision strength. The yellow circles show the results for all of the transitions in the file. The hollow black circles show the results for just the transitions from the ground level.

strength results for Fe^{16+} from [13], [14], and [15]. As one can see, previous work is about 10-20% different than our results for these L-shell transition. Similar differences are found for many of the L-shell transitions. The discrepancies are due to small differences in the target structure, and to the higher-n resonances that are included in these previous calculations. Contributions from resonances attached to core excitations to the n=4 and 5 shells are not included in the current calculations, due to the size of the calculations required to include the K-shell processes. Thus, we do not recommend using the L-shell data from the current calculations, instead the previous data should be used. The purpose of this chapter is to provide data for the K-shell excitations. Our final recommended dataset is a combination of previous L-shell iso-electronic sequence data [14] with our current K-shell data, though our current L-shell data are also available upon request.

We investigated the importance of both radiation and Auger damping on our results, focusing on the K-shell transitions. For the L-shell excitations, neither radiation damping or Auger damping has a significant effect on the effective collision strengths. Figure 5.4 shows the results for a K-shell dipole and a non-dipole excitation. For the non-dipole transition $1s^22s^22p^6(^1S_0) \rightarrow 1s2s^22p^63s(^3S_1)$ in the low temperature range, the effects of radiation damping on the resonances results in about a 20% decrease in the effective collision strengths, with the effect decreasing at higher temperatures. In the case of the dipole excitation, radiation damping does not significantly change the effective collision strengths, such as the $1s^22s^22p^6(^1S_0) \rightarrow 1s2s^22p^63p(^1P_1)$ transition shown in Figure 5.4. This is due to the dominance of the background over the resonance contributions. In no cases were Auger damping found to be important. The differences described here were typical for all of the K-shell excitations that we calculated.

Thus our final calculations for each of the Ne-like ions (Cr, Mn, Fe, Co, and Ni) consist of 800,000 mesh points in the outer region, and include radiation damping. Figure 5.5 shows the effective collision strengths for the non-dipole transition $1s^22s^22p^6(^1S_0) \rightarrow 1s2s^22p^63s(^3S_1)$ and for the dipole transition $1s^22s^22p^6(^1S_0) \rightarrow 1s2s^22p^63p(^1P_1)$ for each of the ions. As

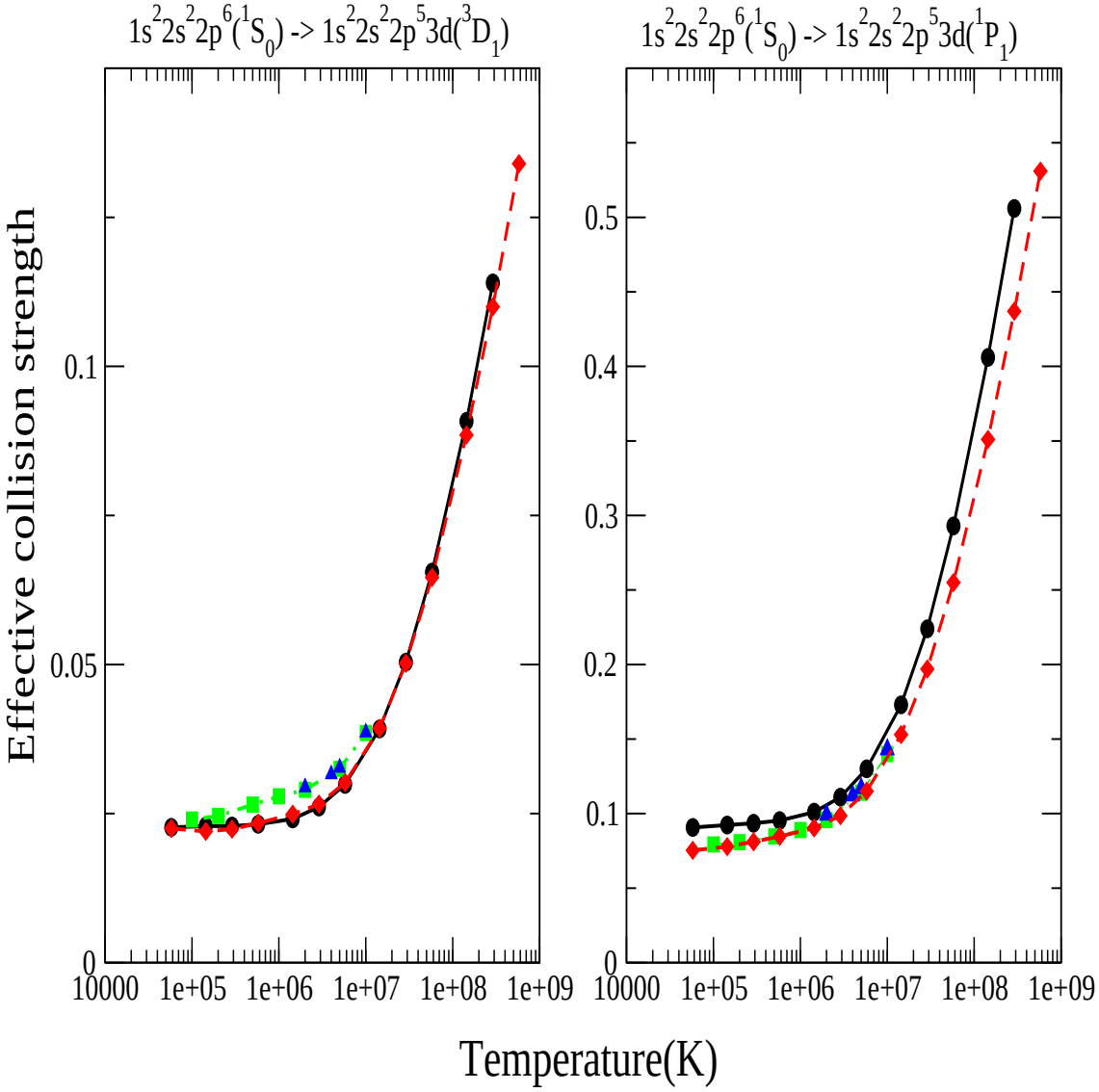

Figure 5.3: Effective collision strength for Ne-like Fe transitions $1s^2 2s^2 2p^6 (^1S_0) \rightarrow 1s^2 2s^2 2p^5 3d(^3D_1)$ and $1s^2 2s^2 2p^6 (^1S_0) \rightarrow 1s^2 2s^2 2p^5 3d(^1P_1)$. Circle(black) shows the results from the current work (without radiation damping), squares(green) show the results from [13], diamonds (red) show the results of [14], and the up-triangles (blue) show the results of [15].

one might expect the effective collision strengths decrease with increasing ion charge. For the dipole transitions the behavior is smooth and could be used to extrapolate to other ion stages, however the results for the low temperature non-dipole rates do not show a simple z-scaling, due to the effect of the resonance contribution.

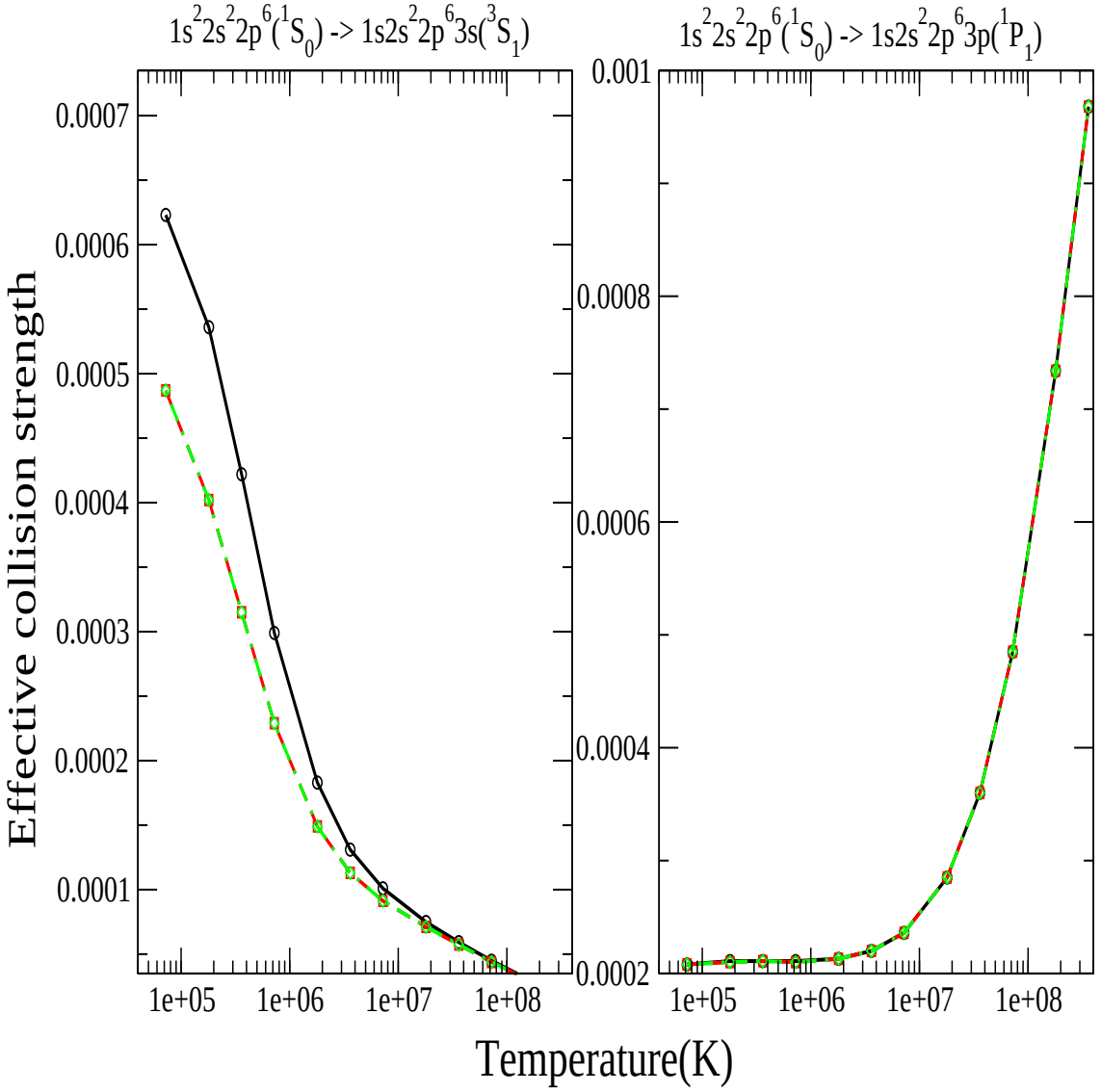

Figure 5.4: Effective collision strengths for Ne-like Fe, K-shell transitions. Circles(solid black line), squares(dashed red line) and diamonds(dot-dashed green line)show the results for no-damping, radiation damping, and Auger+radiation damping, respectively.

5.4 Spectral modeling results

As an illustration of the use of the new K-shell data, we analyze the Cr, Mn, Fe, and Ni $K\alpha$ fluxes for Tycho's SNR reported in Tamagawa [1]. Two important issues to investigate are the confirmation of the line identifications of Tamagawa [1] and checks on possible line blending in the line intensities of these lines. We used our collision datasets to generate photon emissivity coefficient data for a range of plasma electron temperatures and densities. To compare with the observations of [1] we generated a spectrum from our photon emissivity data for Ne=1cm^{-3} and Te=4 keV, using only our Ne-like data. The results are shown in Figure 5.6. Figure 5.6 also shows the measured Tycho spectrum from Tamagawa [1]. In the synthetic spectrum we have assumed relative abundances for Mn, Cr, and Fe that will be determined later in this section.

For the Kα transitions of Cr, Mn, and Fe, we have good agreement between our line positions and those from the observations, confirming the line identifications of Tamagawa [1]. It can also be seen that the Kβ transition features from some of the ions overlap with the Kα transitions of neighboring ions. For example, the Mn Kβ would be blended with the Fe Kα and the Cr Kβ would be blended with the Mn Kα. However, the Kβ intensity is small compared with the strong Kα lines and could be safely ignored when considering the total line flux. The Fe Kβ feature could be blended with the Co Kα transition if the Co abundance were sufficiently high. This should be included in any analysis using the Fe Kβ intensity (e.g. if the ratio of the Fe Kα to the Fe Kβ lines were to be used to determine the electron temperature). One can see that there is clearly observed flux below the energy that one would expect from the Ne-like Fe Kβ line alone, and that this agrees well with the expected position of the Co Kα line. The Suzaku XIS spectrometer cannot resolve these two lines, and without knowledge of the Co abundance in the plasma, it is not possible to extract their relative contributions. We investigate the possible range of Co abundances that would lead to such blending later in this section.

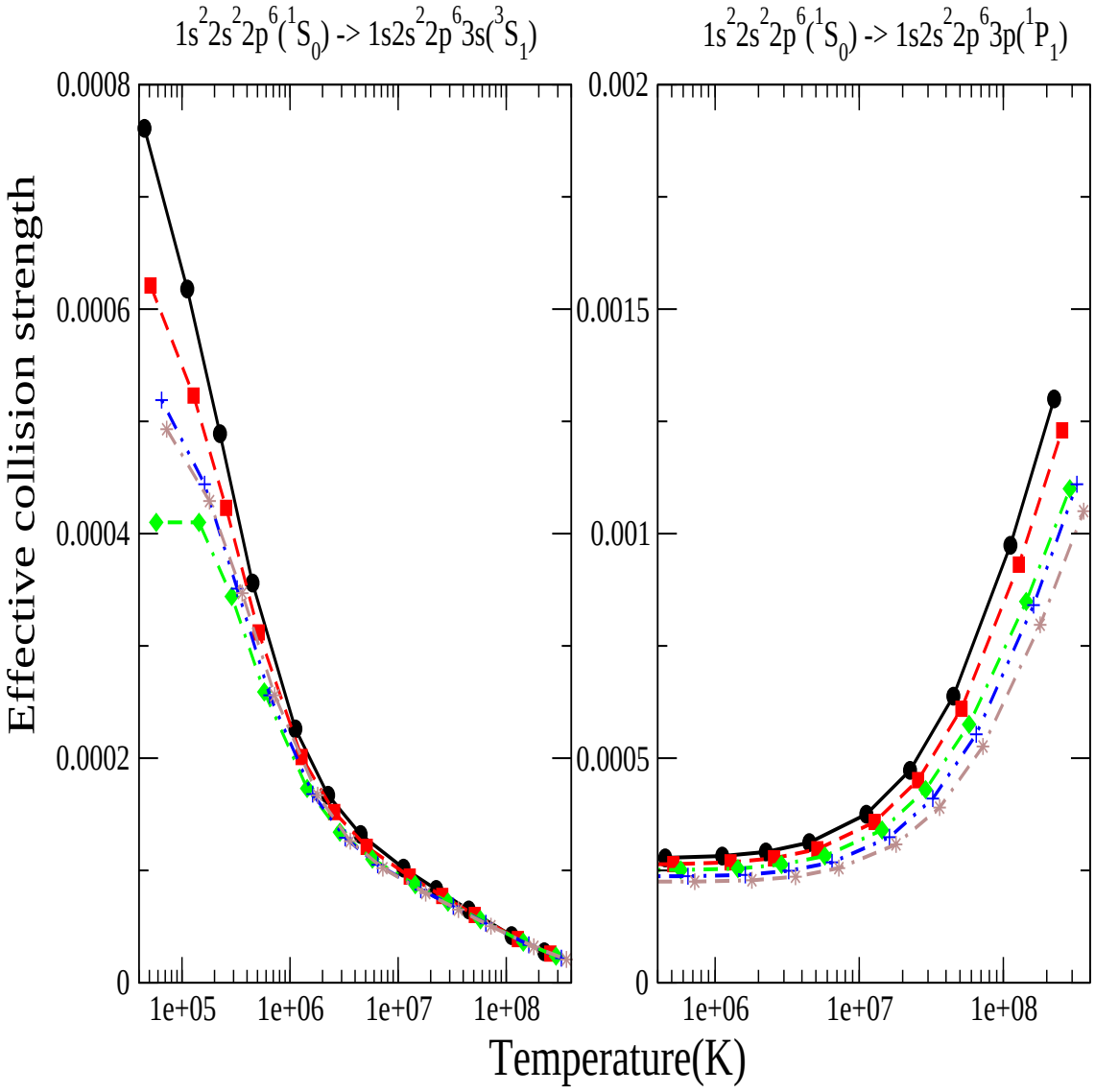

Figure 5.5: Circles(black), squares(red), diamonds (green), plus(blue), and stars(tan) show the effective collision strength for Ne-like Cr, Mn, Fe, Co and Ni K-shell transitions respectively.

Table 5.3: Fe-peak elements abundance ratio

Temp(keV)	1	2	4	Solar abundances
Mn/Fe	0.0191	0.0123	0.0143	0.0052
Cr/Fe	0.0107	0.0190	0.0252	0.01
Ni/Fe	0.0651	0.0359	0.0271	0.038

The reported line fluxes from Tamagawa [1] were used to determine relative abundances of Cr, Mn, and Ni to Fe. The fluxes reported by Tamagawa [1] from their table 1 are 69.1 $\times$ 10^{-5} and 1.13 $\times 10^{-5}$ photons cm^{-2} s^{-1} for Fe and Mn $K\alpha$ lines respectively. Using this ratio and our PEC ratio of Fe and Mn, we can determine the relative abundance from equation 4. In a similar manner we can determine the relative abundances for Cr and Ni. We show the results for four different temperatures in table 5.3. Note that these are the first diagnosed abundances for these elements in Tycho's SNR plasma.

We can also compare our derived relative abundances with abundances from other astrophysical objects. The solar photosphere abundances from Anders [16] give Mn, Cr and Ni to Fe ratios of 0.0052, 0.01 and 0.038 respectively, thus our abundances are about twice the solar photospheric value.

Consider next the spectral feature at 7.1 keV, usually identified as Fe Kβ. As mentioned above, this line is possibly blended with the Co Kα transitions. However, at the lower temperatures in our modelling (1 keV and 2 keV) the predicted Fe Kβ intensity from our photon emissivities is already stronger than that observed in the measurements. At 3.5 keV electron temperature, the predicted Fe Kβ to Fe Kα intensity is 0.05, closer to the ratio of the two features observed from Tycho. Thus, for the feature at 7.1 keV to be a blend of Co Kβ and Fe Kα, the temperature would have to be 3.5 keV or higher in the plasma, and the Co abundance would have to be sufficient for the Co Kβ feature to be strong.

From the spectral measurements it is not possible to extract a Co abundance, however we can determine the minimum abundance that would be required for the Co Kα line to affect the Fe Kβ line intensity, to determine whether this is a likely explanation of the emission

at 7.1keV. The ratio of the Fe Kβ photon emissivity coefficient over the Co Kα photon emissivity coefficient (across a temperature range from 0.2-6 keV) is about 0.07. If the Co Kα line intensity was one third of the Fe Kβ intensity, an abundance of 2% Co compared with Fe would be required. This seems consistent with the abundances for Cr, Mn, and Ni determined above. However, it would be significantly larger than the solar photospheric abundance for Co ($N_{Co}/N_{Fe} = 0.0025$) as reported by Anders [16]. Figure 5.6 shows what the predicted Co Kα intensity would be if solar abundances were assumed, and would clearly not be sufficient to match the observed intensities. Thus, if the feature at 7.1 keV did contain Co contributions, the Co abundance in Tycho's SNR plasma would have to be quite large. Another possibility is that there are other ion stages of iron present, other than the Ne-like ones included in the current modeling. This will be investigated further in the next chapter.

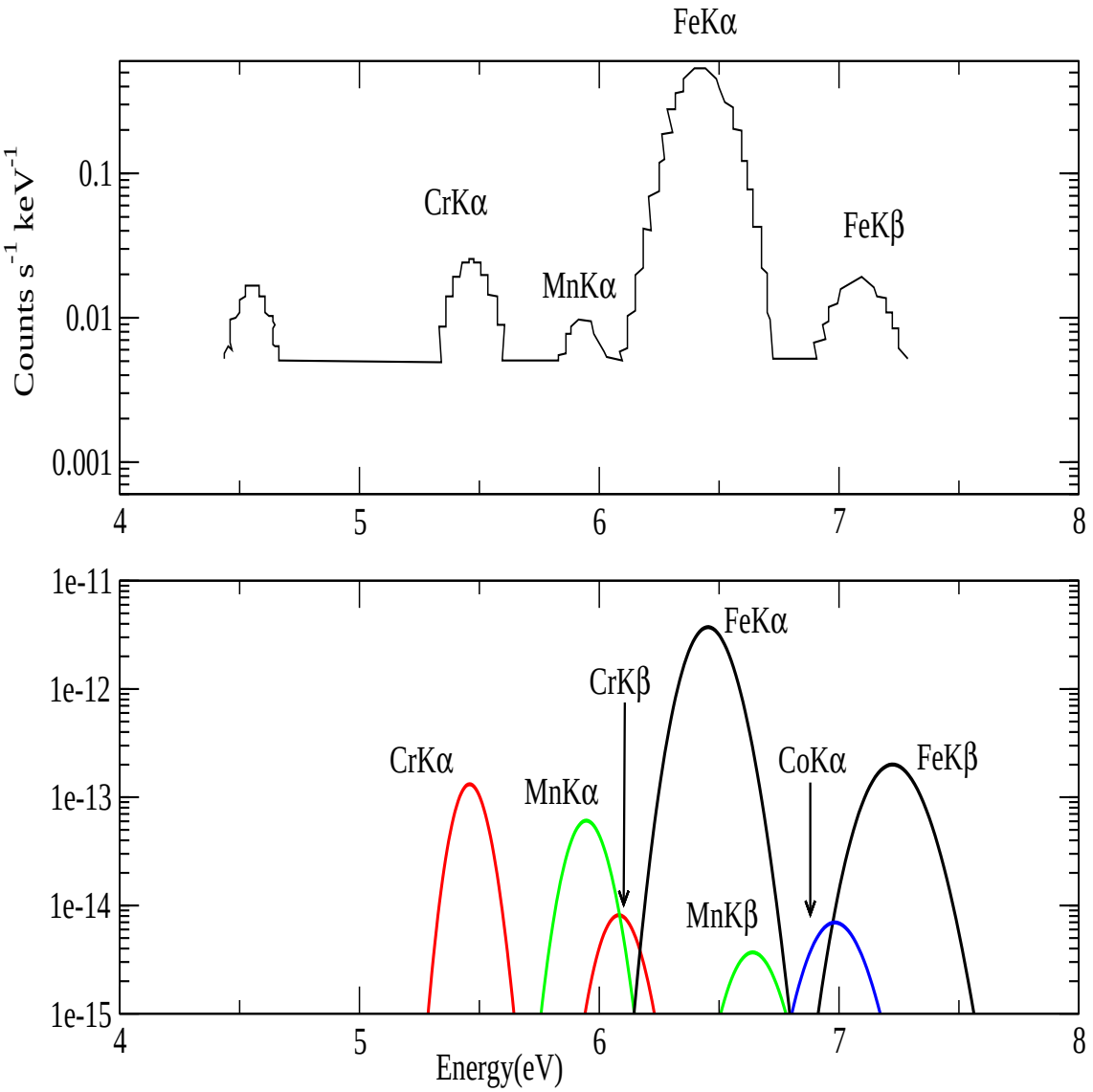

Figure 5.6: Synthetic spectrum for Fe-peak elements, compared with the measured spectrum from [1]. For Co, solar photospheric abundance[16] has been used. For Cr and Ni the abundances derived in this chapter are used.

Chapter 6

F-like iron-peak elements

6.1 Introduction

As part of this project, further Fe-peak element atomic data were generated. This was partly for completion in the database, but was also motivated by the fact that while the observed Fe-peak element spectra have been identified as He-like and Ne-like emission, this is not known for sure. Thus, further sequence work would assist in determining whether the spectrum could contain other ion stages of the Fe-peak elements. One of the issues to explore is whether the K-shell signatures from neighboring ion stages could be distinguished from each other. In this chapter we describe work on the F-like sequence. This was then applied to generate a spectrum. In the previous chapter, see Figure 5.6, the feature previously identified as Ne-like Fe Kβ is likely to be a blend with another line. This can be seen from the line width, or from the poor agreement with the Ne-like Fe Kβ wavelength. In the previous chapter we showed that it could be Co Kα, provided that the Co abundance was higher than normally expected in SNR plasmas. In this chapter, we investigate whether it could be another ion stage of Fe that is causing the blend. That is, perhaps it is not a pure Ne-like spectrum that is being detected, but a blend of neighboring ion stages. We also compare the Kα and Kβ intensities from Ne-like and F-like ions, to explore whether the ion stages could be distinguished spectroscopically. Thus, we performed similar R-matrix calculations as those described in the previous chapter, but for the F-like Fe-peak elements. We calculated electron-impact excitation collision strength for F-like Cr, Mn, Fe, Co and Ni. Due to the small contribution that radiation damping made in the Ne-like calculations for the temperatures of importance for SNR plasmas, we perform undamped calculations for the ions in this chapter.

Table 6.1: scaling parameters for F-like iron-peak elements

orbital	scaling parameter
1s	1.0
2s	1.0
2p	0.92300
3s	0.77410
3p	0.87900
3d	0.85660

6.2 Results

For each stage F-like iron-peak elements, we use the AUTOSTRUCTURE code [55] to generate the radial orbitals that were been subsequently used in the ICFT calculations. In order to match the available NIST K-shell energy value ($1s2s^22p^6$), we chose the orbital scaling parameters shown in Table 6.1. Note that this case is slightly different from the Ne-like Fe calculation in the previous chapter, where no K-shell NIST energies were available. In this case were were able to optimise on one available K-shell energy.

All the 71 LS terms(157 JΠ levels) arising from the following configurations $2p^5$, $1s2s^22p^6$, $1s^22s2p^6$, $2p^4nl$, $2s2p^5nl$ and $1s2s^22p^5nl$ (n=3 and $l = s, p, d$) were used in the close-coupling expansion of the subsequent scattering calculation. The energy range of the incident electron extended from 0 to 2200 Ryds(approximately 4 times the K shell edge) for each of the ion stages. Eighty-four partial waves ranging in angular momentum from L=0-13 were evaluated for the exchange calculation. Another 152 higher partial waves (L=14-48) were calculated without exchange. All results were "topped-up" to include higher L contributions to the cross section using the method described by [72] for dipole transitions and a geometric series for non-dipole transitions.

In Table 6.2, we compare our AUTOSTRUCTURE target energies with the available NIST energies. Unlike in the Ne-like case, NIST has one energy level for the K-shell hole that we can compare with ours. From the table, we can see that the average difference between NIST values and our AUTOSTRUCTURE results is about 1.42%. In the asymptotic region,

we performed several calculations on the ion stage, to verify the energy mesh that was sufficient to converge the effective collision strengths. In the previous chapter, we have shown that for Fe^{16+} 800,000 points energy mesh were required. However, this size of energy mesh is prohibitively large for the F-like calculations. Thus, we investigated the results using 200,000 and 400,000 energy mesh points, using Fe^{17+} as the case study. We found that 90% of the transitions from the ground state had converged to within 5%, see Figure 6.1. For the supernova remnant plasma applications, which are very low density plasmas, the spectrum will be dominated by transitions from the ground and this level of accuracy should be sufficient.

In the previous chapter, we performed calculations with no radiation damping, with radiation damping, and with Auger + radiation damping. We saw no difference between radiation damping and Auger + radiation damping, and very small difference between non-radiation damping and radiation damping. Thus, in this chapter we will focus on non-radiation damping calculations. Figure 6.2 shows the first 2 transitions of our R-matrix calculation and Witthoeft et al. [17] calculations. Since we have used different scaling parameters for the structure, this calculation is about 10% lower than Witthoeft et al.. The K-shell transitions that we calculated were not included in the calculations of Witthoeft. From the Figure 6.2, it can be seen that for the non-dipole transition $1s^22s^22p^5(^2P_{1.5}) \rightarrow 1s^22s^22p^5(^2P_{0.5})$ or the dipole transition $1s^22s^22p^5(^2P_{1.5}) \rightarrow 1s^22s2p^6(^2S_{0.5})$, the shape of our calculation agrees with that of Witthoeft et al. The differences in the calculation are what one might expect given the different target structures. Note that we have chosen to optimize our structure on the K-shell energy levels, and thus our L-shell data are only shown for completion. The final modeling dataset should use the L-shell data of Witthoeft et al., combined with our K-shell data.

Figure 6.3 shows two K-shell transitions for all the Fe-peak elements without any radiation damping. There are no literature values to compare with. For the dipole transition $1s^22s^22p^5(^2P_{1.5}) \rightarrow 1s2s^22p^6(^2S_{0.5})$, all five curves follow the same increasing slope and show

Table 6.2: Level energies from AUTOSTRUCTURE and corresponding NIST energies.

Configuration	Term	J	NIST result (Ry)	AUTOSTRUCTURE value (Ry)	Difference (%)
$1s^2 2s^2 2p^5$	^2P	1.5	0.0000	0.0000	0.00
	^2P	0.5	0.9347	0.9873	5.32
$1s^2 2s 2p^6$	^2S	0.5	9.7023	9.7704	0.70
$1s^2 2s^2 2p^4 3s$	^4P	2.5	56.6990	57.9659	2.18
	^4P	1.5	57.5028	58.6911	2.02
	^4P	0.5	57.5729	58.8253	2.13
$1s^2 2s^2 2p^4 3s$	^2P	1.5	56.9369	58.2002	2.17
	^2P	0.5	57.7980	59.0528	2.12
$1s^2 2s^2 2p^4 3s$	^2D	2.5	58.3000	59.5705	2.13
	^2D	1.5	58.3557	59.6031	2.09
$1s^2 2s^2 2p^4 3s$	^2S	0.5	59.9167	61.1694	2.05
$1s^2 2s^2 2p^4 3d$	^4P	0.5	62.4965	63.5753	1.70
	^4P	1.5	62.6259	63.7237	1.72
	^4P	2.5	62.9111	64.2821	2.13
$1s^2 2s^2 2p^4 3d$	^2F	2.5	62.6988	63.8006	1.73
$1s^2 2s^2 2p^4 3d$	^4D	0.5	62.9066	63.0502	0.23
	^4D	1.5	63.0510	63.1565	0.17
$1s^2 2s^2 2p^4 3d$	^2P	1.5	63.3085	63.5072	0.31
$1s^2 2s^2 2p^4 3d$	^2D	2.5	63.4014	64.4974	1.70
$1s^2 2s^2 2p^4 3d$	^2S	0.5	63.9190	64.9957	1.66
$1s^2 2s^2 2p^4 3d$	^2P	1.5	64.1386	64.4051	0.41
	^2P	0.5	64.4649	63.8113	1.02
$1s^2 2s^2 2p^4 3d$	^2D	2.5	64.1605	64.4973	0.52
$1s^2 2s^2 2p^4 3d$	^2D	2.5	65.3050	65.2919	0.02
	^2D	1.5	65.4682	65.5177	0.07
$1s^2 2s 2p^5 3s$	^4P	2.5	65.4818	66.4001	1.38
	^4P	1.5	65.5912	66.7330	1.71
	^4P	0.5	65.8354	67.1440	1.95
$1s^2 2s 2p^5 3s$	^2P	1.5	66.0751	67.2479	1.74
$1s^2 2s 2p^5 3p$	^4D	1.5	68.0206	68.7885	1.11
$1s^2 2s 2p^5 3p$	^2D	2.5	68.1373	68.9119	1.12
	^2D	1.5	68.9569	69.7835	1.18
$1s^2 2s 2p^5 3p$	^2P	1.5	68.2339	69.1544	1.33
	^2P	0.5	68.4188	69.3607	1.36
$1s^2 2s 2p^5 3p$	^4P	2.5	68.4118	69.3371	1.33
	^4P	1.5	68.6175	69.3760	1.09
$1s^2 2s 2p^5 3p$	^2S	0.5	69.2508	70.1537	1.29
$1s^2 2s 2p^5 3p$	^2D	1.5	70.7453	71.7512	1.40
	^2D	2.5	70.9362	71.9640	1.43
$1s^2 2s 2p^5 3p$	^2P	0.5	70.9510	72.0050	1.46
	^2P	1.5	71.0278	72.0980	1.48
$1s 2s^2 2p^6$	^2S	0.5	474.2140	475.2814	0.22

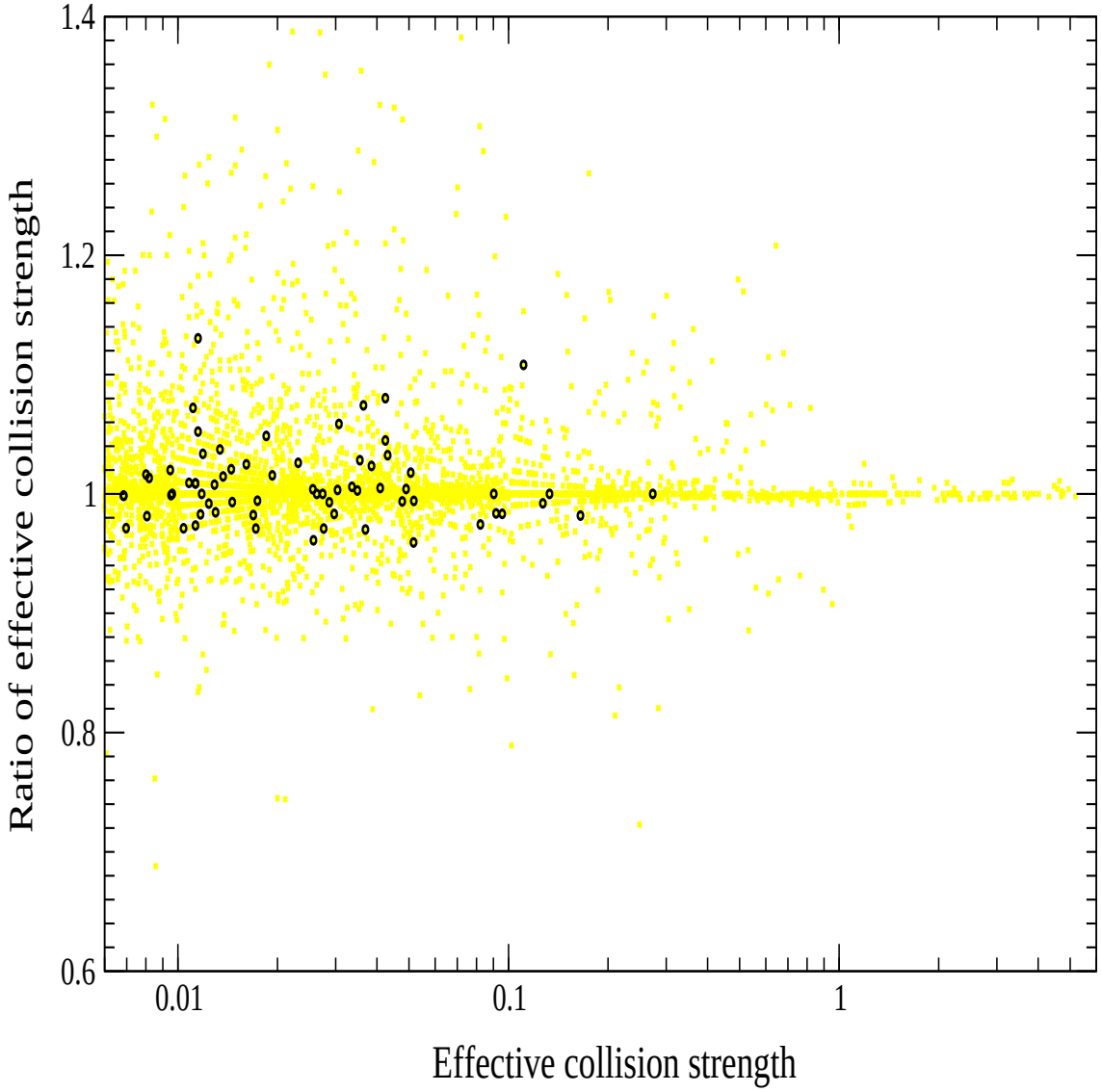

Figure 6.1: Ratio of effective collision strength of (200k/400k) energy mesh vs effective collision strength for F-like Fe. The yellow circles show the results for all of the transitions and the hollow black circles show the results for the ground level only.

a predictable order. For the non-dipole transition $1s^2 2s^2 2p^5(^2P_{1.5}) \rightarrow 1s2s^2 2p^5 3p(^4D_{2.5})$, all five elements show similar trends, but with some changes in the order for individual ions, in a similar manner to the non-dipole Ne-like transitions shown in the previous chapter.

The new excitation data was used to generate a spectrum. For the purpose of the spectral comparison, we assume that each of the ion stages have equal abundances, that is we are comparing their photon emissivities directly. The purpose here is to investigate differences in central wavelength and intensity for each of the spectral features. Considering first the intensities of the lines, one can see from Figure 6.4 that for the F-like ion the Kα feature is much stronger than the Kα feature for the Ne-like ion. This is to be expected, given the strong 1s-2p excitation that can populate the Kα feature in the F-like case, while this transition is not possible in the Ne-like case due to the 2p shell being full. A plot of the Kα to Kβ line ratio for each of these ions (Figure 6.5) shows that this difference persists at all temperatures.

Considering next the wavelength positions, the Kβ feature for the F-like ion is shifted to higher energy, compared with the Kβ feature for th Ne-like ion. This shift is stronger than the one seen for the Kα line. It is not surprising that the Kα feature is not strongly shifted in wavelength, due to the small perturbation that the n=3 electrons will make on the n=2 to 1 transition energy. With the larger splitting of the terms of the $1s2s^2 2p^5 3l$ configurations, one would expect a larger shift in the Kβ wavelengths. Note that this is in the wrong direction to explain the feature in the Tycho spectrum, thus to further investigate the 7.1 keV feature in Tycho's spectrum, the focus should be on ions of lower charge states of Fe (e.g. Na-like, Mg-like etc). The new F-like data will be archived online, and used by the modeling community.

Thus, it appears that one could potentially resolve emission from F-like and Ne-like Fe using the central wavelength of the Kβ feature, and self-consistently checking the line ratio of the Kα to Kβ features. It may be that the next generation of X-ray telescopes would be able to spectroscopically resolve the Kβ features from the neighboring Fe ions.

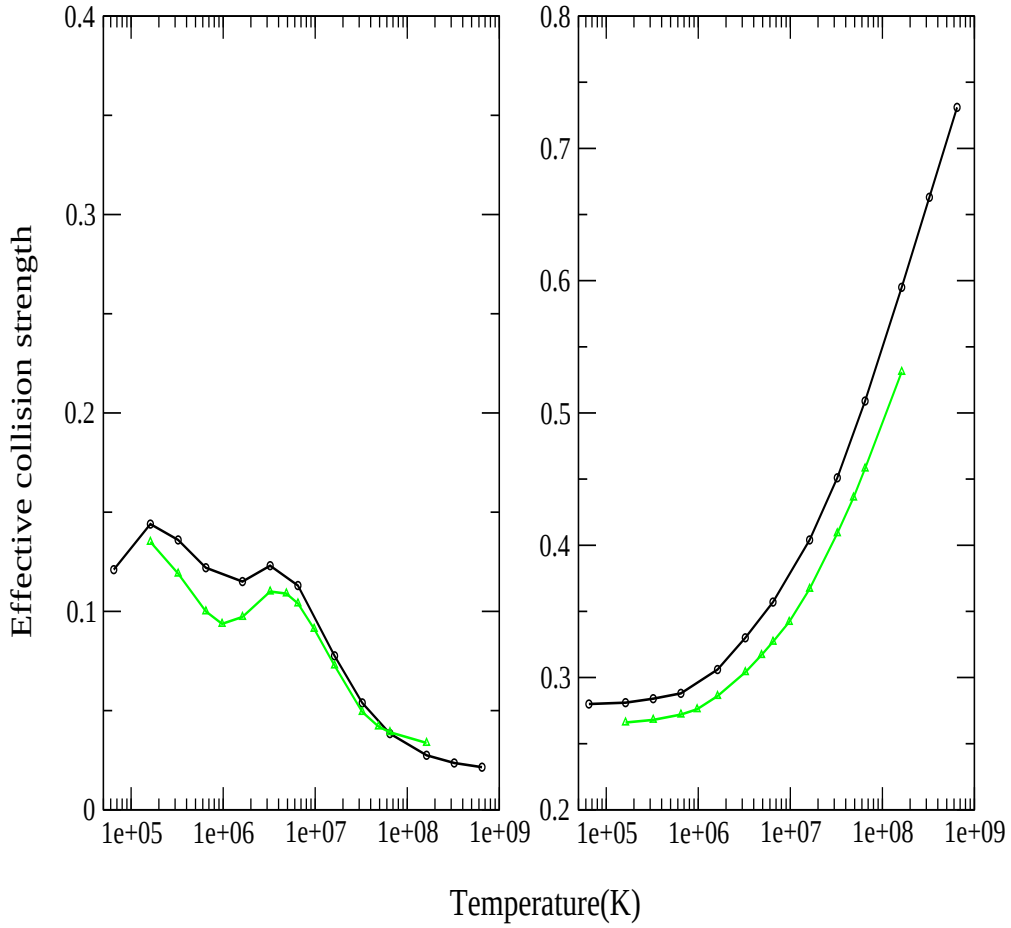

Figure 6.2: Effective collision strength of this work and Witthoeft et al. [17]. Circles(black) shows the R-matrix calculation of F-like Fe without radiation damping. Triangle up(green) shows Witthoeft et al. data. Non-dipole transition $1s^2 2s^2 2p^5(^2P_{1.5}) \rightarrow 1s^2 2s^2 2p^5(^2P_{0.5})$ is the left part and dipole transition $1s^2 2s^2 2p^5(^2P_{1.5}) \rightarrow 1s^2 2s 2p^6(^2S_{0.5})$ is on the right.

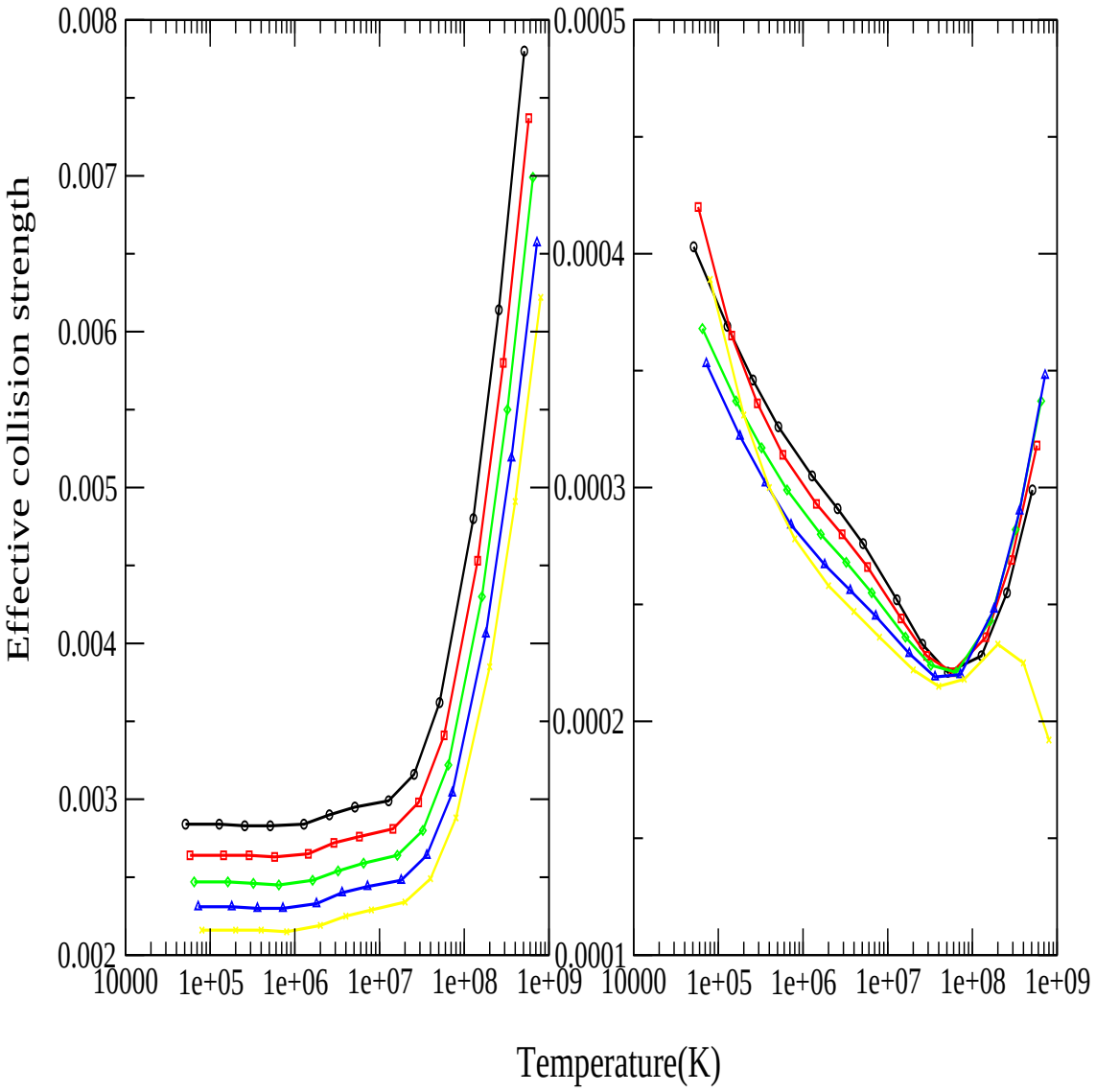

Figure 6.3: Effective collision strength of Fe-peak elements. Circles(black), squares(red), diamonds(green), triangle-up(blue) and X(yellow) stand for Cr, Mn, Fe, Co and Ni respectively. Dipole transition $1s^2 2s^2 2p^5 (^2P_{1.5}) \rightarrow 1s 2s^2 2p^6 (^2S_{0.5})$ is on left and non-dipole transition $1s^2 2s^2 2p^5 (^2P_{1.5}) \rightarrow 1s 2s^2 2p^5 3p (^4D_{2.5})$ is on the right.

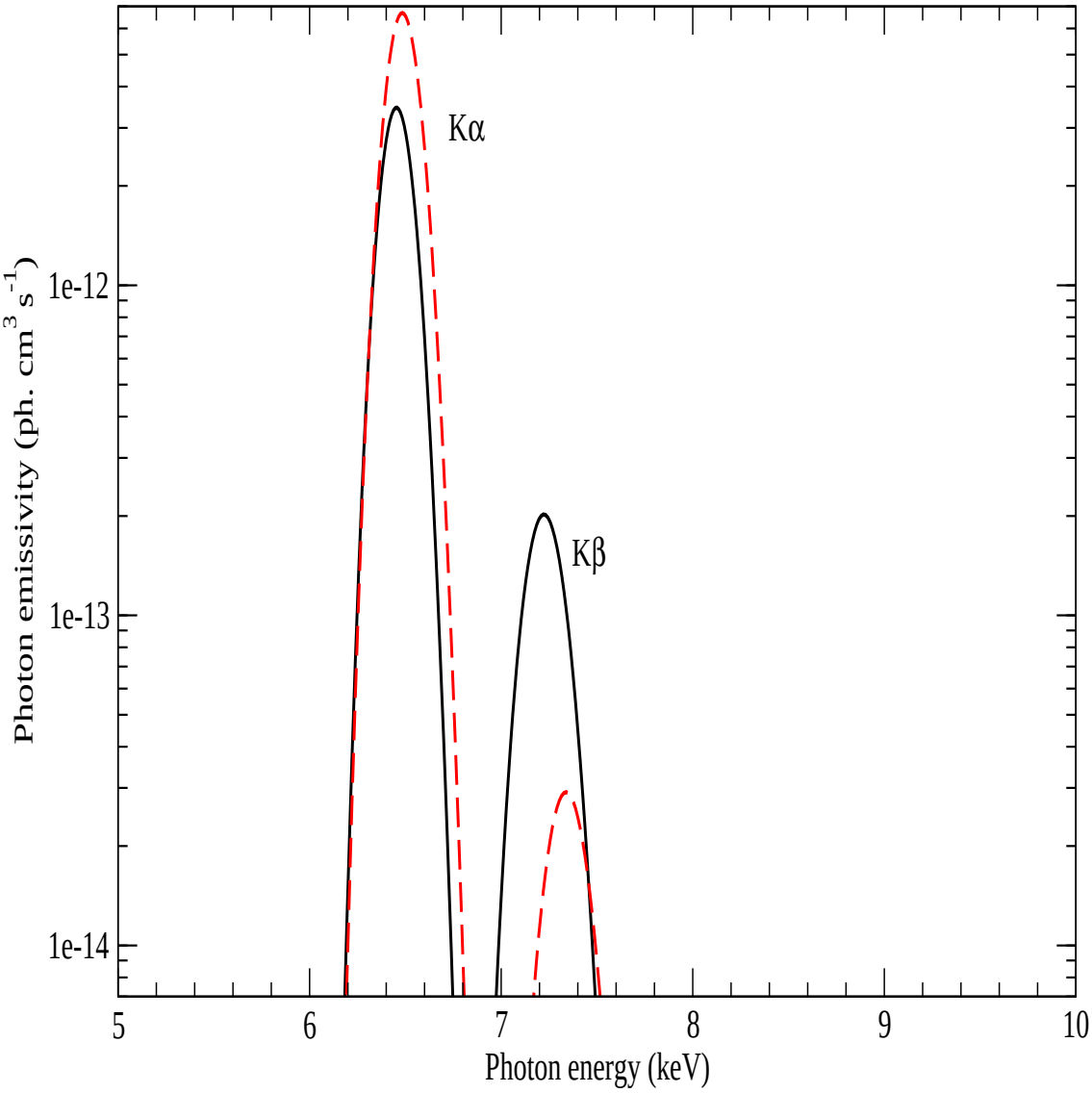

Figure 6.4: Theoretical spectrum of Ne-like and F-like Fe. The spectrum is generated at Te=4 keV and Ne=1 cm^{-3}. Solid line (black) shows Ne-like Fe and dashed line(red) shows F-like Fe.

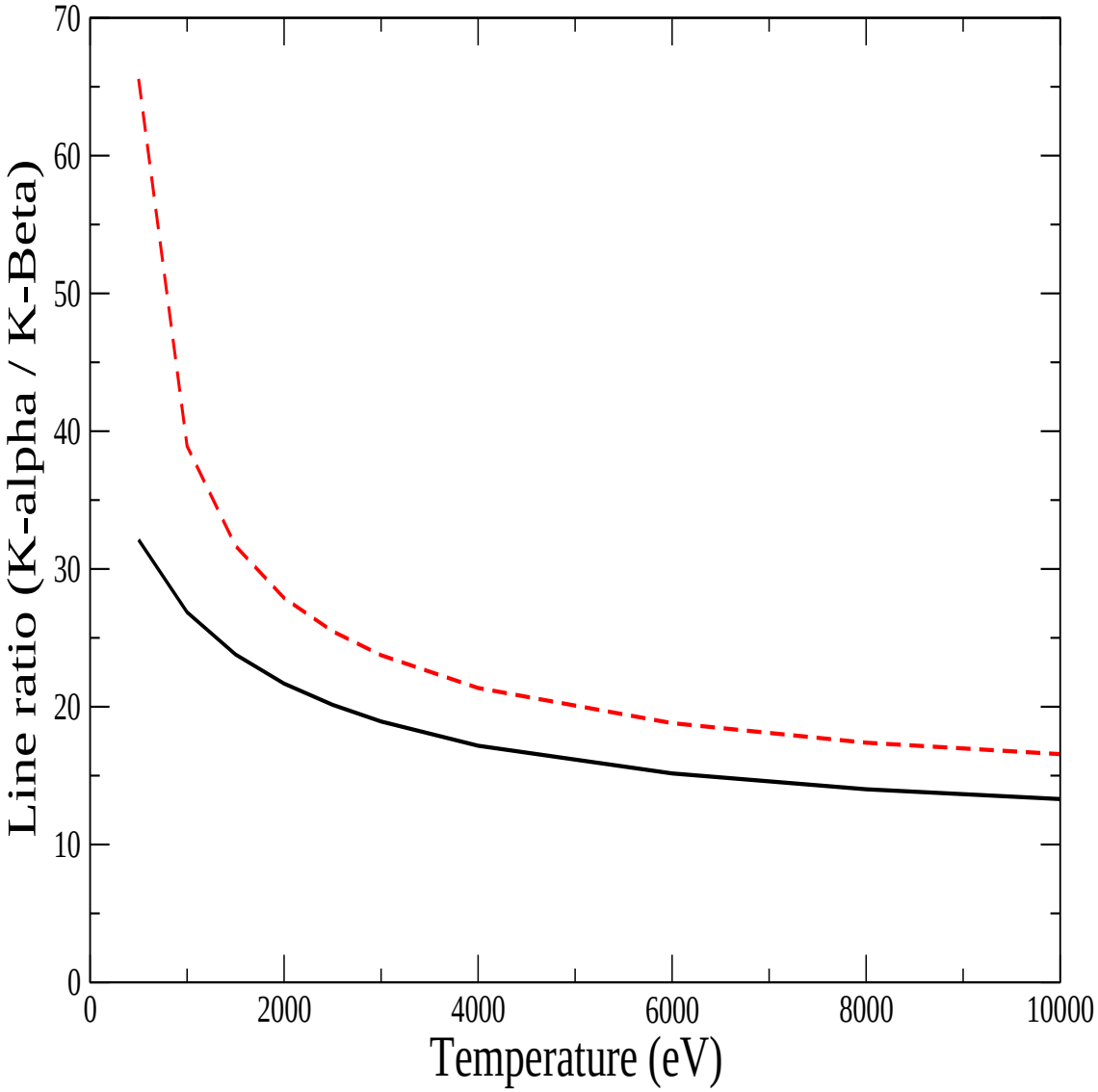

Figure 6.5: Theoretical spectrum of the Kα to Kβ line ratio for Ne-like and F-like Fe. The spectrum is generated at Ne=1 cm^{-3}. Solid line (black) shows Ne-like Fe and dashed line(red) shows F-like Fe.

Chapter 7

Conclusions

In this dissertation, we have applied non-perturbative quantal methods to calculate new atomic data for use in laboratory and astrophysical plasmas. The work was motivated by two areas of application, namely the impurity transport modeling of Al in fusion plasmas and spectral modeling of Fe-peak elements from supernova remnant plasmas. For each of these areas new electron-impact data was required, namely ionization data for Al and excitation data for the Fe-peak elements.

Considering the ionization of Al, the low charge states are particularly important when modeling the erosion from the wall, and the existing ADAS semi-empirical data for these ion stages was likely to be poor. There already existed non-perturbative atomic data for Al^+. Thus, we focused on the electron-impact ionization of neutral Al and Al^{2+} (chapters 2 and 3). In each of these cases the non-perturbative calculations (RMPS and TDCC) produced cross sections that were below the perturbative DW calculation, due to correlation in both the direct and indirect ionization processes. For neutral Al, the factor of two decrease in the direct ionization is one of the largest seen in all of the atoms studied to date. For Al^+, the non-perturbative calculations were below the experimental cross sections, with the weight of evidence pointing to the non-perturbative data being more accurate.

These non-perturbative data were combined with CADW calculations for the remaining ion stages. The results were compared with the measurements of with Aichele [10]. The ion stages where the discrepancies exist are those with expected metastable pressure in the beam. Thus, we have a final recommended ionization dataset consisting of non-perturbative data for the first three ion stages, and DW data for the remaining charge states. We generated Maxwellian rate coefficients, and will archive the data in online databases. In chapter 4 we

gave a brief overview of the rates, comparing them to literature values. We also showed an equilibrium ionization balance calculation, indicating that the new data will predict that the lower charge states exist up to higher temperatures than previously thought, due to the reduction in their ionization cross sections. The new Al data is being sent to researchers at the MST fusion plasma experiment and will be used there for impurity transport modeling.

In the second part of this dissertation, the focus was on generating atomic data for supernova remnant plasma spectroscopy. Recent observations of K-shell emission from Ne-like Fe-peak elements for SNR plasmas have potentially very useful diagnostics applications. However, such studies are hampered by a lack of K-shell atomic data for these ions. Thus, in chapter 5 we reported on calculations for K-shell electron-impact excitation of Ne-like Cr, Mn, Fe, Co and Ni. We compare our calculations with available L-shell data from the literature. We also investigate the effects of radiation and Auger damping. While radiation damping has an effect at the lowest temperatures, Auger damping does not significantly change the effective collision strengths. We generated photon emissivity coefficients from our collision data using a collisional-radiative model. These coefficients are used to determine abundances for Mn, Cr and Ni from the observations of [1]. These are the first such abundances determined for Tycho's SNR plasma. Critically, we find that the Fe Kβ line is possibly blended with a Co Kα line. This must be accounted for when using the Fe Kβ line for any spectral diagnostics, so as not to overestimate the Fe Kβ line intensity. In chapter 6 we then presented similar calculations for F-like Fe-peak elements, and have archived these files for use by the modeling community. To make the data more accessible to the community it will be put into the ATOMDB and the XSPEC model, as well as in the OPEN-ADAS and CFADC web pages.

The future work in this area will involve calculating some of the other iso-electronic sequences for Fe-peak elements. There are numerous reasons for this, including to determine whether the blend at 7.1 keV could be due to other ion stages of Fe, rather than from Co. It is possible that multiple ion stages are present in the plasma, so the spectra from each

of the component ion stages should be considered in the total emission. Once the data is archived online it is hoped that it finds wide use in the astrophysics modeling community. Also of interest for future work would be to update the ionization and recombination data for the Fe-peak elements, and to investigate non-equilibrium ionization balance models for SNR emissions.

Bibliography

[1] T. Tamagawa et al. Suzaku observations of Tycho's supernova remnant. *Publications of the Astronomical Society of Japan*, 61:S167–S174, 2009.

[2] R. S. Freund, R. C. Wetzel, R. J. Shul, and T. R. Hayes. Cross-section measurements for electron-impact ionization of atoms. *Phys. Rev. A*, 41:3575–3595, Apr 1990.

[3] M. R. BELIC. Exact solution to the degenerate four-wave mixing in reflection geometry in photorefractive media. *Phys. Rev. A*, 31(3169), 1987.

[4] R. G. Montague and M. F. A. Harrison. A measurement of the cross section for electron impact ionisation of Al^+. *J. Phys. B: At. Mol. Opt. Phys.*, 16(16), 1983.

[5] S. J. T. Hayton and B. Peart. Measurements of cross sections for the ionization of Al^+ and Cd^+ by energy-resolved electrons. *J. Phys. B: At. Mol. Opt. Phys.*, 27(5331), 1994.

[6] D. H. Crandall, R. A. Phaneuf, R. A. Falk, D. S. Belic, and G. H. Dunn. Absolute cross-section measurements for electron-impact ionization of Na-like ions Mg^+, Al^{2+}, and Si^{3+}. *Phys. Rev. A*, 25:143–153, Jan 1982.

[7] J. W. G. Thomason and B. Peart. The electron-impact ionization of Al^+ ions. *J. Phys. B: At. Mol. Opt. Phys.*, 31:L201, 1998.

[8] N. R. Badnell, M. S. Pindzola, I. Bray, and D. C. Griffin. Time-independent and time-dependent close-coupling methods for the electron-impact ionization of Mg^+, Al^{2+}, and Si^{3+}. *J. Phys. B: At. Mol. Opt. Phys.*, 31:911, Feb 1998.

[9] Huaguo Teng. Electron-impact ionization of Al^{2+} ions: a unified R-matrix calculation. *J. Phys. B: At. Mol. Opt. Phys.*, 33(15):L553, 2000.

[10] K. Aichele, M. Steidl, U. Hartenfeller, D. Hathiramani, F. Scheuermann, M. Westermann, E. Salzborn, and M. S. Pindzola. Electron-impact single ionization of multiply charged aluminium ions. *J. Phys. B: At. Mol. Opt. Phys.*, 34:4113, 2001.

[11] E. J. McGuire. Born-approximation electron ionization cross sections for Al^{n+} and some ions of the Na isoelectronic sequence. *Phys. Rev. A*, 26:125–131, Jul 1982.

[12] K. P. Dere. Ionization rate coefficients for the elements hydrogen through zinc. *Astron. Astrophys.*, 466(2):771, 2007.

[13] S. D. Loch, M. S. Pindzola, C. P. Ballance, and D. C. Griffin. The effects of radiative cascades on the X-ray diagnostic lines of Fe^{16+}. *J. Phys. B: At. Mol. Opt. Phys.*, 39:85, 2006.

[14] G. Y. Liang and N. R. Badnell. R-matrix electron-impact excitation data for the Ne-like iso-electronic sequence. *Astronomy and Astrophysics*, 518(A64), 2010.

[15] Guo-Xin Chen. Converged dirac R-matrix calculation of electron impact excitation of Fe XVII. *Phys. Review A*, 76(062708), 2007.

[16] E. Anders and N. Grevesse. Abundances of the elements: Meteoritic and solar. *Geochimica et Cosmochimica Acta*, 53:197–214, 1989.

[17] M. C. Witthoeft, A. D. Whiteford, and N. R. Badnell. R-matrix electron-impact excitation calculations along the F-like iso-electronoic sequence. *J. Phys. B: At. Mol. Opt. Phys.*, 40:2969–2993, 2007.

[18] L. Lauro-Taroni et al. *Proceedings of the 21st EPS Conference on Controlled Fusion and Plasma Physics*, 1:102, 1994.

[19] http://www.ipp.mpg.de/∼dcp/solps.html.

[20] http://w3.pppl.gov/transp.

[21] C. S. Chang, Seunghoe Ku, and H. Weitzner. Numerical study of neoclassical plasma pedestal in a tokamak geometry. *Physics of Plasmas*, 11:2649, 2004.

[22] T. Putterich, R. Neu, R. Dux, A.D. Whiteford, M.G. O'Mullane, and the ASDEX Upgrade team. Modelling of measured tungsten spectra from asdex upgrade and predictions for iter. *Plasma Physics and Controlled Fusion*, 50:085016, 2008.

[23] T. Putterich, R. Neu, A. D. Whiteford R. Dux, M. G. O'Mullane, and the ASDEX Upgrade team. Calculation and experimental test of the cooling factor of tungsten. *Nuclear Fusion*, 50:025012, 2010.

[24] N. R. Badnell, M. G. O'Mullane, H. P. Summers, Z. Altun, M. A. Bautista, J. Colgan, T. W. Gorczyca, D. M. Mitnik, M. S. Pindzola, and O. Zatsarinny. Dielectronic recombination data for dynamic finite-density plasmas. *Astronomy and Astrophysics*, 406:1151–1165, 2003.

[25] N. R. Badnell. Dielectronic recombination of fe $3p^q$ ions: A key ingredient for describing x-ray absorption in active galactic nuclei. *The Astrophysical Journal*, 651:L73–L76, 2006.

[26] M. F. Gu. Radiative recombination rate coefficients for bare through F-like isosequences of Mg, Si, Ar, Ca, Fe, and Ni. *The Astrophysical Journal*, 589(2):1085, 2003.

[27] H. P. Summers, W. J. Dickson, M. G. O'Mullane, N. R. Badnell, A. D. Whiteford, D. H. Brooks, J. Lang, S. D. Loch, and D. C. Griffin. Ionization state, excited populations and emission of impurities in dynamic finite density plasmas: I. the generalized collisional

Dradiative model for light elements. *Plasma Physics and Controlled Fusion*, 48:263, 2006.

[28] M. Mattioli, G. Mazzitelli, M. Finkenthal, P. Mazzotta, K. B. Fournier, J. Kaastra, and M. E. Puiatti. Updating of ionization data for ionization balance evaluations of atoms and ions for the elements hydrogen to germanium. *J. Phys. B: At. Mol. Opt. Phys.*, 40(18):3569, 2007.

[29] S. D. Loch, C. P. Ballance, D. Wu, Sh A Abdel-Naby, and M. S. Pindzola. Electron-impact ionization of Al. *J. Phys. B: At. Mol. Opt. Phys.*, 45:065201, 2012.

[30] Di Wu, S. D. Loch, M. S. Pindzola, and C. P. Ballance. Electron-impact ionization of Al^{2+}. *Phys. Rev. A*, 85:012711, 2012.

[31] S. E. Woosley and Thomas A. Weaver. The physics of supernova explosions. *Annual Review of Astronomy and Astrophysics*, 24:205–253, 1986.

[32] E. Cappellaro R. Barbon, V. Buondi and M. Turatto. http://adsabs.harvard.edu/abs/2008ycat.2283....0b.

[33] M. Fink, W. Hillebrandt, and F. K. R/"opke. Double-detonation supernovae of sub-Chandrasekhar mass white dwarfs. *Astronomy and Astrophysics*, 476:1133–1143, 2007.

[34] S. Immler, P. J. Brown, P. Milne, L.-S. The, R. Petre, N. Gehrels, D. N. Burrows, J. A. Nousek, C. L. Williams, E. Pian, P. A. Mazzali, K. Nomoto, R. A. Chevalier, V. Mangano, S. T. Holland, P. W. A. Roming, J. Greiner, and D. Pooley. X-ray observations of Type Ia supernovae with swift: Evidence of circumstellar interaction for SN 2005ke. *The Astrophysical Journal Letters*, 648:L119, 2006.

[35] S. A. Colgate. Supernovae as a standard candle for cosmology. *Astrophysical Journal*, 232:404–408, 1979.

[36] A. Saha, Allan Sandage, G. A. Tammann, Lukas Labhardt, F. D. Macchetto, and N. Panagia. Cepheid calibration of the peak brightness of Type Ia Supernovae. IX. SN 1989b in NGC 3627. *Astrophysical Journal*, 522:802, 1999.

[37] Wendy L. Freedman, Barry F. Madore, Brad K. Gibson, Laura Ferrarese, Daniel D. Kelson, Shoko Sakai, Jeremy R. Mould, Robert C. Kennicutt Jr., Holland C. Ford, John A. Graham, John P. Huchra, Shaun M. G. Hughes, Garth D. Illingworth, Lucas M. Macri, and Peter B. Stetson. Final results from the Hubble space telescope key project to measure the hubble constant. *The Astrophysical Journal*, 553:47, 2001.

[38] Adam G. Riess, Alexei V. Filippenko, Peter Challis, Alejandro Clocchiatti, Alan Diercks, Peter M. Garnavich, Ron L. Gilliland, Craig J. Hogan, Saurabh Jha, Robert P. Kirshner, B. Leibundgut, M. M. Phillips, David Reiss, Brian P. Schmidt, Robert A. Schommer, R. Chris Smith, J. Spyromilio, Christopher Stubbs, Nicholas B. Suntzeff, and John Tonry. Observational evidence from supernovae for an accelerating universe and a cosmological constant. *The Astrophysical Journal*, 116:1009, 1998.

[39] L. Ciotti, S. Pellegrini, A. Renziji, and A. D'ercole. Winds, outflows, and inflows in X-ray elliptical galaxies. *The Astrophysical Journal*, 376:380–403, 1991.

[40] Andrea Ferrara and Eline Tolstoy. The role of stellar feedback and dark matter in the evolution of dwarf galaxies. *Monthly Notices of the Royal Astronomical Society*, 313:291–309, 2000.

[41] Carles Badenes, Eduardo Bravo, and John P. Hughes. The end of amnesia: A new method for measuring the metallicity of Type Ia supernova progenitors using manganese lines in supernova remnants. *The Astrophysical Journal Letters*, 680:L33, 2008.

[42] X. J. Yang, H. Tsunemi, F. J. Lu, and L. Chen. A Cr-K emission line survey in young supernova remnants with chandra. *The Astrophysical Journal*, 692:894, 2009.

[43] J. Oelgoetz, C. J. Fontes, H. L. Zhang, M. Montenegro, S. N. Nahar, and A. K. Pradhan. High-temperature behaviour of the helium-like KαG ratio: the effect of improved recombination rate coefficients for calcium, iron and nickel. *Monthly Notices of the Royal Astronomical Society*, 382:761–769, 2007.

[44] Una Hwang, Robert Petre, and John P. Hughes. The X-ray line emission from the supernova remnant W49B. *The Astrophysical Journal*, 532:970, 2000.

[45] M. Miceli, A. Decourchelle, J. Ballet, F. Bocchino, J. P. Hughes, U. Hwang, and R. Petre. The X-ray emission of the supernova remnant W49B observed with XMM-Newton. *Astronomy and Astrophysics*, 453:567–578, 2006.

[46] David N. Burrows, Eli Michael, Una Hwang, Richard McCray, Roger A. Chevalier, Robert Petre, Gordon P. Garmire, Stephen S. Holt, and John A. Nousek. The X-ray remnant of SN 1987A. *The Astrophysical Journal Letters*, 543:L149, 2000.

[47] Carles Badenes, Kazimierz J. Borkowski, John P. Hughes, Una Hwang, and Eduardo Bravo. Constraints on the physics of Type Ia supernovae from the X-ray spectrum of the Tycho supernova remnant. *The Astrophysical Journal*, 645:1373, 2006.

[48] M. S. Pindzola, D. C. Griffin, and C. Bottcher. Atomic processes in electron-ion and ion-ion collisions. *NATO ASI Ser.*, 145:75, 1986.

[49] H. Anderson, M. G. von Hellermann, R. Hoekstra, L. D. Horton, A. C. Howman, R. W. T. Konig, R. Martin, R. E. Olson, and H. P. Summers. Neutral beam stopping and emission in fusion plasmas i: deuterium beams. *Plasma Physics and Controlled Fusion*, 42:781–806, 2000.

[50] S. Otranto, R. E. Olson, and P. Beiersdorfer. Conetary x-rays: line emission cross sections for multiply charged solar wind ion charge exchange. *J. Phys. B: At. Mol. Opt. Phys.*, 40:1755, 2007.

[51] D. R. Bates, A. E. Kingston, and R. W. P. McWhirter. Recombination between electrons and atomic ions. I. optically thin plasmas. *Proceedings of the Royal Society A.*, 267(1330):297–312, 1962.

[52] Eugene P. Wigner. Resonance reactions. *Physics Review*, 70:606–618, 1946.

[53] E. P. Wigner and L. Eisenbud. Higher angular momenta and long range interaction in resonance reactions. *Physics Review*, 72:29–41, 1947.

[54] P. G. Burke and W. D. Robb. The R-matrix theory of atomic processes. *Advances in Atomic and Molecular Physics*, 11:143–214, 1976.

[55] N. R. Badnell. A BreitPauli distorted wave implementation for autostructure. *Computer Physics Communications*, 182(7):1528 – 1535, 2011.

[56] L. S. Blackford et al. *ScaLAPACK Users' Guide*. SIAM, Philadelphia, PA, 1997.

[57] P. G. Burke, D. F. Gallaher, and S. Geltman. Electron scattering by atomic hydrogen using a pseudo-state expansion I. elastic scattering. *J. Phys. B: At. Mol. Opt. Phys.*, 2:1142, 1969.

[58] K. Bartschat, E. T. Hudson, M. P. Scott, P. G. Burke, and V. M. Burke. Electron - atom scattering at low and intermediate energies using a pseudo-state/ R-matrix basis. *J. Phys. B: At. Mol. Opt. Phys.*, 29(1):115, 1996.

[59] T. W. Gorczyca and N. R. Badnell. Radiation damping in highly charged ions: an R-matrix approach. *J. Phys. B: At. Mol. Opt. Phys.*, 29(L283), 1996.

[60] C. P. Ballance and D. C. Griffin. Electron-impact excitation of neon: a pseudo-state convergence study. *J. Phys. B: At. Mol. Opt. Phys.*, 37(14):2943, 2004.

[61] D. M. Mitnik, D. C. Griffin, C. P. Ballance, and N. R. Badnell. An R-matrix with pseudo-states calculation of electron-impact excitation in C^{2+}. *J. Phys. B: At. Mol. Opt. Phys.*, 36(4):717, 2003.

[62] Keith A. Berrington, Werner B. Eissner, and Patrick H. Norrington. Rmatrx1: Belfast atomic R-matrix codes. *Computer Physics Communications*, 92:290 – 420, 1995.

[63] M. S. Pindzola, F. Robicheaux, S. D. Loch, J. C. Berengut, T. Topcu, J. Colgan, M. Foster, D. C. Griffin, C. P. Ballance, D. R. Schultz, T. Minami, N. R. Badnell, M. C. Witthoeft, D. R. Plante, D. M. Mitnik, J. A. Ludlow, and U. Kleiman. The time-dependent close-coupling method for atomic and molecular collision processes. *J. Phys. B: At. Mol. Opt. Phys.*, 40(7):R39, 2007.

[64] M. S. Pindzola and F. Robicheaux. Total ionization cross section for electron-hydrogen scattering using a time-dependent close-coupling method. *Phys. Rev. A*, 54(3):2142, 1996.

[65] Klaus Bartschat. The R-matrix with pseudo-states method: Theory and applications to electron scattering and photoionization. *Comput. Phys. Commun.*, 114(1-3):168, 1998.

[66] C. P. Ballance, D. C. Griffin, M. S. Pindzola, and S. D. Loch. Electron-impact ionization of argon using the r-matrix with a pseudo-states method. *J. Phys. B: At. Mol. Opt. Phys.*, 40(3):F27, 2007.

[67] C. P. Ballance, J. A. Ludlow, M. S. Pindzola, and S. D. Loch. Electron-impact ionization of ground and metastable neon. *J. Phys. B: At. Mol. Opt. Phys.*, 42(17), 2009.

[68] S. T. A. Kumar, D. J. Den Hartog, R. M. Magee, G. Fiksel, and D. Craig. Behaviour of carbon and boron impurities in the madison symmetric torus. *Plasma Phys. Control. Fusion*, 53(3), 2011.

[69] R. D. Cowan. *The Theory of Atomic Structure and Spectra*. University of California Press, Berkeley,California, 1981.

[70] J. Botero and J. H. Macek. Coulomb born approximation for electron scattering from neutral atoms: application to electron impact ionization of helium in coplanar symmetric geometry. *J. Phys. B: At. Mol. Opt. Phys.*, 24(16):L405, 1991.

[71] http://physics.nist.gov/physrefdata/asd/levels_form.html.

[72] A. Burgess. Coulomb integrals: tables and sum rules. *J. Phys. B: At. Mol. Phys.*, 7:L364, 1970.

[73] Charlotte Froese Fischer. General Hartree-Fock program. *Computer Physics Communications*, 43(3):355 – 365, 1987.

[74] S. S. Tayal and J. W. Henry. Contributions of excitation autoionization to electron-impact ionization of Mg-like Al^{+}, S^{4+}, Cl^{5+}, and Ar^{6+} ions. *Phys. Rev. A*, 33:3825–3831, 1986.

[75] J. A. Ludlow, C. P. Ballance, S. D. Loch, M. S. Pindzola, and D. C. Griffin. Electron-impact single ionization of Mg and Al^{+}. *Phys. Rev. A*, 79(032715), 2009.

[76] S. D. Loch, M. S. Pindzola, C. P. Ballance, D. C. Griffin, D. M. Mitnik, N. R. Badnell, M. G. ÓMullane, H. P. Summers, and A. D. Whiteford. Electron-impact ionization of all ionization stages of krypton. *Phys. Rev. A*, 66(052708), 2002.

[77] S. D. Loch, J. A. Ludlow, M. S. Pindzola, A. D. Whiteford, and D. C. Griffin. Electron-impact ionization of atomic ions in the W isonuclear sequence. *Phys. Rev. A*, 72(052716), 2005.

[78] S. M. Younger. Cross sections and rates for direct electron-impact ionization of sodiumlike ions. *Phys. Rev. A*, 24:1272–1277, Sep 1981.

[79] D. C. Griffin, C. Bottcher, and M. S. Pindzola. Contributions of excitation autoionization to the electron-impact ionization of Mg^{+}, Al^{2+}, and Si^{3+} in the distorted-wave approximation with exchange. *Phys. Rev. A*, 25:154–160, Jan 1982.

[80] R. J. W. Henry and A. Z. Msezane. Cross sections for inner-shell excitation of Na-like ions. *Phys. Rev. A*, 26:2545–2550, Nov 1982.

[81] K. L. Bell, H. B. Gilbody, J. G. Hughes, A. E. Kingston, and F. J. Smith. Recommended data on the electron impact ionization of light atoms and ions. *Journal of Physical and Chemical Reference Data*, 12(891), 1983.

[82] Wolfgang Lotz. Electron-impact ionization cross-sections and ionization rate coefficients for atoms and ions from hydrogen to calcium. *ZEITSCHRIFT FÜR PHYSIK A HADRONS AND NUCLEI*, 216(3):241–247, 1968.

[83] Jan M. Rost and Thomas Pattard. Analytical parametrization for the shape of atomic ionization cross sections. *Phys. Rev. A*, 55:R5–R7, 1997.

[84] H. Yamaguchi and K. Koyama. Suzaku view of supernova remnants. *Memorie della Societ Astronomica Italiana*, 81(1):382, 2010.

[85] M. Nobukawa, K. Koyama, T. G. Tsuru, S. G. Ryu, and V. Tatischeff. Discovery of K-shell emission lines of neutral atoms in the galactic center region. *Publ. Astron. Soc. Japan*, 62:423–429, 2010.

[86] T. Tamura, Y. Maeda, K. Mitsuda, A. C. Fabian, J. S. Sanders, A. Furuzawa, J. P. Hughes, R. Iizuka, K. Matsushita, and T. Tamagawa. X-ray spectroscopy of the core of the perseus cluster with Suzaku: Elemental abundances in the intracluster medium. *The Astrophysical Journal Letters*, 705(L62), 2009.

[87] Guo Xin Chen and Anil K. Pradhan. Influence of resonances on spectral formation of X-ray lines in Fe XVII. *Physical Review Letters*, 89(013202), 2002.

[88] G. V. Brown, P. Beiersdorfer, D. A. Liedahl, K. Widmann, and S. M. Kahn. Laboratory measurements and modeling of the Fe XVII X-ray spectrum. *The Astrophysical Journal*, 502:1015, 1998.

[89] J. D. Gillaspy, T. Lin, L. Tedesco, J. N. Tan, J. M. Pomeroy, J. M. Laming, N. Brickhouse, G.-X. Chen, and E. Silver. Fe XVII X-ray line ratios for accurate astrophysical plasma diagnostics. *The Astrophysical Journal*, 728:132, 2011.

[90] K. M. Aggarwal and F. P. Keenan. Electron impact excitation of Ne-like Ni XIX. *Journal of Physics: Conference Series*, 58:169–172, 2007.

[91] G. X. Chen, K. Kirby, E. Silver, N. S. Brickhouse, J. D. Gillaspy, J. N. Tan, J. M. Pomeroy, and J. M. Laming. The 3C/3D line ratio in Ni XIX: New Ab Initio theory and experimental results. *Physical Review Letters*, 97(143201), 2006.

[92] D. C. Griffin, C. P. Ballance, D. M. Mitnik, and J. C. Berengut. Dirac R-matrix calculations of electron-impact excitation of neon-like krypton. *J. Phys. B: At. Mol. Opt. Phys.*, 41(215201), 2008.

[93] N. R. Badnell. Dielectronic recombination of Fe^{22+} and Fe^{21+}. *J. Phys. B: At. Mol. Opt. Phys.*, 19:3827, 1986.

[94] F. Robicheaux, T. W. Gorczyca, and M. S. Pindzola. Inclusion of radiation damping in the close-coupling equations for electron-atom scattering. *Phys. Rev. A*, 52:1319–1333, 1995.

Appendix A : Configuration-average ionization potentials for Al

Ion Stage	Transition	CA IP (eV)	Double IP (eV)
Al	$1s^22s^22p^63s^23p \rightarrow 1s^22s^22p^63s^2$	6.15	24.45
	$1s^22s^22p^63s^23p \rightarrow 1s^22s^22p^53s3p$	10.85	
	$1s^22s^22p^63s^23p \rightarrow 1s^22s^22p^53s^23p$	81.55	
	$1s^22s^22p^63s^23p \rightarrow 1s^22s^12p^63s^23p$	128.836	
	$1s^22s^22p^63s^23p \rightarrow 1s^12s^22p^63s^23p$	1569.86	
Al^+	$1s^22s^22p^63s^2 \rightarrow 1s^22s^22p^63s$	18.30	46.93
	$1s^22s^22p^63s^2 \rightarrow 1s^22s^22p^53s^2$	91.54	
	$1s^22s^22p^63s^2 \rightarrow 1s^22s^12p^63s^2$	138.90	
	$1s^22s^22p^63s^2 \rightarrow 1s^12s^22p^63s^2$	1594.65	
Al^{2+}	$1s^22s^22p^63s \rightarrow 1s^22s^22p^6$	28.63	147.20
	$1s^22s^22p^63s \rightarrow 1s^22s^22p^53s$	104.73	
	$1s^22s^22p^63s \rightarrow 1s^22s2p^63s$	151.86	
	$1s^22s^22p^63s \rightarrow 1s2s^22p^63s$	1593.98	
Al^{3+}	$1s^22s^22p^6 \rightarrow 1s^22s^22p^5$	119.57	275.46
	$1s^22s^22p^6 \rightarrow 1s^22s2p^6$	166.39	
	$1s^22s^22p^6 \rightarrow 1s2s^22p^6$	1609.87	
Al^{4+}	$1s^22s^22p^5 \rightarrow 1s^22s^22p^4$	155.89	351.15
	$1s^22s^22p^5 \rightarrow 1s^22s2p^5$	198.84	
	$1s^22s^22p^5 \rightarrow 1s2s^22p^5$	1656.72	
Al^{5+}	$1s^22s^22p^4 \rightarrow 1s^22s^22p^3$	195.26	432.89
	$1s^22s^22p^4 \rightarrow 1s^22s2p^4$	233.65	
	$1s^22s^22p^4 \rightarrow 1s2s^22p^4$	1991.84	
Al^{6+}	$1s^22s^22p^3 \rightarrow 1s^22s^22p^2$	237.63	520.58
	$1s^22s^22p^3 \rightarrow 1s^22s2p^3$	270.75	
	$1s^22s^22p^3 \rightarrow 1s2s^22p^3$	1764.18	
Al^{7+}	$1s^22s^22p^2 \rightarrow 1s^22s^22p$	282.95	614.16
	$1s^22s^22p^2 \rightarrow 1s^22s2p^2$	310.10	
	$1s^22s^22p^2 \rightarrow 1s2s^22p^2$	1824.62	
Al^{8+}	$1s^22s^22p \rightarrow 1s^22s^2$	331.21	614.16
	$1s^22s^22p \rightarrow 1s^22s2p$	351.67	
	$1s^22s^22p \rightarrow 1s2s^22p$	1889.44	
Al^{9+}	$1s^22s^2 \rightarrow 1s^22s$	395.42	838.12
	$1s^22s^2 \rightarrow 1s2s^2$	1958.58	
Al^{10+}	$1s^22s \rightarrow 1s^2$	442.70	2529.60
	$1s^22s \rightarrow 1s2s$	2021.43	
Al^{11+}	$1s^2 \rightarrow 1s$	2086.90	

Table 1: Configuration-Average Ionization Potential(IP) and Double Ionization Potential for Al ion stage from Al to Al^{11+}